MASTER THESIS, 2021, CONDENSED MATTER PHYSICS

High Polarization Purity and Short-wavelength Integrated Optics for Trapped-ion Quantum Systems

Leonardo Massai

Zürich, Trapped Ion Quantum Information Group, ETHZ

University of Pisa Supervisor:
Prof. Dr. Oliver Morsch

ETHZ Supervisor:
Prof. Dr. Jonathan Home
Dr. Karan K Mehta

Abstract

One of the most ambitious goals of modern Physics and Computer Science is the realization of a universal quantum computer. Among all the implementations of quantum systems as quantum bits (qubits) that are tested and pursued, ion trapping represents one of the most promising options. This is due in part to the long coherence times and lifetime of the electronic states used to encode the qubit and the reproducibility, since every ion is the same. However, scalability is possibly the most challenging to fulfil among all DiVincenzo's criteria for ions as well as many other qubit modalities. For this reason, a development in designing ion traps and in-chip photonics is lately strongly pursued. In fact, integrated photonics have shown early promise, but the requirements of trapped-ion systems raise numerous challenges for integrated photonics. In particular, generating pure circularly polarized fields for state preparation and readout in ion-based qubits (and to some extent for laser cooling, i.e. EIT [1]), and developing materials capable of guiding the blue and UV wavelengths of interest are two of major challenges in this direction.

The present thesis aims at studying a micro-metric ring resonator, that in its structural simplicity and without active tuning, is able to emit pure ($P \sim 99.9\%$) circularly-polarized beams (so with one polarization component being a P fraction of the total intensity), that can be integrated into next-generation ion trap designs and used for high fidelity quantum state control. Furthermore, a study on Hafnium Dioxide (HfO_2), used to realize multi-layer composite together with Alumina (Al_2O_3), as a potential low-loss high refractive index material for blue-UV waveguides is presented. The resulting material gets as low as ~ 2.2 dB/cm for slab mode loss and ~ 4.2 dB/cm for material loss keeping an effective refractive index of $n \sim 1.96$ ($\lambda = 406$ nm) and there is the possibility for further optimization. This multi-layer *nano-laminate* can be suitable for high-index contrast diffraction gratings and highly confining waveguides in the blue-UV.

Acknowledgement

First of all, I would like to thank Dr. Karan K Mehta for supervising me all along my thesis work in TIQI Group. Thanks to his care, high expertise and great passion for the topics, I learnt a lot and I further understood the importance of always having a critical view and an organized method. I also wanted to thank him for the time dedicated to familiarize me with the hands on work in laboratory and cleanroom.

Equally I want to thank Prof. Dr. Jonathan Home and all members of TIQI group for the constant help, and for the opportunity to research on these topics, that largely enriched my education and increased even further my interest for Quantum Information.

Many thanks to Prof. Dr. Oliver Morsch from University of Pisa, for giving me the possibility to pursue my thesis project at ETHZ and for his constant availability.

Last but not least, I wanted to thank my family and my friends, always present during my whole education path and very supporting in each one of my choices.

Contents

Chapter 1

Introduction

1.1 Challenges in integrated photonics

In this thesis work we will tackle two major challenges concerning integrated photonics for single and multiple trapped ions addressing in quantum processors, that can however have useful impact in many other engineering and physics related fields.

Trapped-ion quantum processors make use of ions to encode the physical qubits. The ions are usually first ionized atoms such as Alkaline earth metals - Beryllium ($^{9}Be^{+}$), Magnesium ($^{25}Mg^{+}$), Calcium ($^{40}Ca^{+}$) - in order to have just a single valence electron and a Hydrogen-like electronic structure, where the $|0\rangle$ and $|1\rangle$ states can be encoded. Once the most suitable ion is chosen, it can be trapped in an electrodynamics potential well. Indeed, as a simple consequence of Earnshaw's theorem, it's not possible to confine a charge in 3 dimensions with a superposition of static electric fields. The two main techniques are Penning trapping and Paul trapping [2]. Penning traps exploit a strong magnetic field for radial confinement, while Paul traps use a mix of static (DC) and radio-frequency (RF) electric fields, supplied by electrodes arranged in either 3D or 2D.

However, in order to build a quantum charge-coupled device (QCCD) [3], where every step, from trapping to readout is realized, many further improvements to chip designs and material choices have to be made. One of the most challenging obstacles to overcome (yet a very fascinating topic) is the integration of many wavelengths for optical control of the ion electronic state. So far, state of the art quantum processors, such as the ones developed by companies IonQ [4] and Honeywell [5], or by academic groups as Innsbruck's Quantum Optics and Spectroscopy Group [6] and UMD's Trapped Ion Quantum Information Group [7], employ free-space lasers with the appropriate wavelength to address the single ions inside the ion crystal. This technique can be limiting for scalability due multiple aspects: the number of ions has to be increased and therefore the number of separate free-space beams that have to be accurately aligned to the micron scale, with limited access to the ion string in case of a 3D trap (also due to the vacuum chamber/cryostat where the trap is usually located). Addressing the ions with free-space beams also comports vibrations and polarization impurities given by the chamber windows materials (often slightly birefringent). One promising alternative is designing chips that aside of the electrodes also include waveguides to transport many wavelengths and outcouplers able to radiate focused and polarized beams onto the suspended ions [8]. This approach could give the possibility to supply many beams in parallel using multiple outcouplers simultaneously, along with more vibration stability and less frequency drifts in the employed beams, since all the optics used to emit the light are inside the vacuum system in a much confined zone, protected from the exterior environment. Furthermore, these kind of integrated optical components are planar-fabricated, layer by layer, with well established CMOS techniques.

As stated before, the $|0\rangle$ and $|1\rangle$ states of the logical qubit are chosen to be two out of the many electronic energy states in the selected ion: depending on which couple of these are taken, the qubit is called *Zeeman*, *Hyperfine* or *Optical*. To state prepare, cool down, coherently control and readout the state of the atom, many different wavelengths and, in some species, light polarizations (to exploit selection rules) must be employed. For instance, a commonly used ion in the TIQI Group is Calcium ($^{40}Ca^+$). The needed wavelengths space in a range from 389 nm to 855 nm and to achieve scalability thanks to integrated optics, both waveguides able to transport light in the requested frequency range and outcouplers that can emit light correctly polarized and shaped have to be developed and implemented. Thanks to previous works [9], tapered gratings acting as linearly-polarized light emitters have already been implemented in 2D traps in the 729-855 nm range, tested for even wider ranges of frequencies (405-1092 nm) [10] and their suitability for high-fidelity quantum operation has been shown [11]. However very few researches have been conducted in search of low-loss high refractive index materials for waveguides able to confine modes in the blue-UV frequency range. For instance, Aluminum Oxide (Al_2O_3) is one of the few examples of promising material in this regard. It has already been tested as core material, given the sub dB/cm optical losses in the range of interest, despite its quite low refractive index ~ 1.7 [12]. The same lack of studies regards emitters for circularly-polarized light beams: having the possibility to emit highly-pure circularly-polarized light from micro-metric devices that can be embedded in chips, it's crucial for a fully integrated optics control system. This could permit to perform many more operations on the qubit, such as cooling, state preparation, readout procedures, that are more or less fundamental depending on the used ion species. For instance, in trapped-ion quantum processor based on Beryllium ($^9Be^+$), highly pure circularly-polarized light is really essential to control the *Hyperfine* qubit. However, very few devices have been designed and studied for this purpose so far and, most of the time, without any particular regard or interest to the polarization purity of the emitted light [13]. High purity is required for high-fidelity state preparation via optical pumping, as required for low-error quantum computation [14].

In Chapter 2 and 3 we will present a ring resonator working near 729 nm and able to emit a focused beam perpendicular to the waveguide plane with highly pure circular polarization.

Then, in Chapter 4 we will study Hafnium Dioxide (HfO_2) and how, engineered together with Aluminum Oxide, it can provide a promising waveguide core material in a very wide frequency range, basically covering all the visible spectrum, maintaining losses < 3 dB/cm and refractive index > 1.9 (as unpatterned slab). Having a high contrast in refractive index at the core-cladding interfaces implies various advantages, such as stronger coupling to radiated field if the waveguide is endowed of a diffraction grating, as treated in Section 2.1.4.

1.2 Waveguides and optical fibers

In this Section we present a general dissertation about propagating electromagnetic fields in heterogeneous media. It will give the reader a simple yet enough complete theory to face the waveguides topic recurring in Chapter 2 and 3. Moreover, we present an introduction over waveguides loss mechanisms to better understand Chapter 4.

Dielectric waveguides are multi material composed structures that exploit total internal reflection to guide optical waves with low loss and high confinement. We will treat the waveguide as a dielectric material (core) confined in 2 dimensions by another dielectric material (cladding) with different refractive index. We will see that the confinement of the guided modes is dependent on geometrical aspects of the structure, such as the width and height of the core, here considered to have a rectangular section, and the refractive index difference between the two dielectrics.

1.2.1 Vector potential wave equation

Let's introduce firstly the wave equation for the vector potential $\boldsymbol{A}$ in a non uniform medium without sources[15]:

$$\nabla^2 \boldsymbol{A} + \omega^2 \mu_0 \varepsilon \boldsymbol{A} = -j\omega\mu_0 \nabla\varepsilon\Phi \tag{1.1}$$

where we have chosen the Lorenz gauge

$$\nabla \cdot \boldsymbol{A} + j\omega\mu_0\varepsilon\Phi = 0 \tag{1.2}$$

and assumed a time dependency $\exp(j\omega t)$ with ω the angular frequency. Φ is the scalar potential, ε is the dielectric constant and μ_0 the magnetic permeability of free space. The electric and magnetic fields are given by

$$\begin{aligned} \boldsymbol{E} &= -j\omega\boldsymbol{A} - \nabla\Phi \\ \mu_0\boldsymbol{H} &= \nabla \times \boldsymbol{A} \end{aligned} \tag{1.3}$$

The nonuniform dielectric couples the vector potential to the scalar potential, and vice versa. However, in the studied problem the variation of ε is null due to a homogeneous medium. The coupling term is hence not present and we arrive at the wave equation for $\boldsymbol{A}$:

$$\nabla^2 \boldsymbol{A} + \omega^2 \mu_0 \varepsilon \boldsymbol{A} = 0 \tag{1.4}$$

We assume a uniform medium in the z direction with step variation in the transverse directions (x, y) and a particular polarization for $\boldsymbol{A}$, say parallel to y. We write

$$\boldsymbol{A} = \hat{\boldsymbol{y}} u(x, y) e^{-j\beta z} \tag{1.5}$$

where β is the, still undetermined, propagation constant. The exponential factor $\exp(-j\beta z)$ contains the entire z dependence, so that the remaining factor $u(x, y)$ can be assumed z independent. Considering the medium dielectric constant varying only in the transverse directions x and y, we obtain from Eq. 1.4 the differential equation

$$\nabla_T^2 u + \left[\omega^2\mu_0\varepsilon(x, y) - \beta^2\right] u = 0 \tag{1.6}$$

where ∇_T is the vector differential operator in the two transverse coordinates (x, y). To start, let's consider a simpler structure: a slab material with thickness $2d$ and index ε_i confined in the x dimension.

1.2.2 Transverse electric (TE)

We start with the analysis of a transverse electric (TE) wave with the vector potential and the electric field polarized along $\hat{y}$, transverse to the direction of propagation, the z direction.
Because the structure is symmetric, one picks the origin of the Cartesian coordinates at its center, and one looks for solutions for the electric field that are either symmetric, or antisymmetric with respect to the symmetry plane of the waveguide, the $y - z$ plane.

A schematic of the waveguide is shown in Fig. 1.1

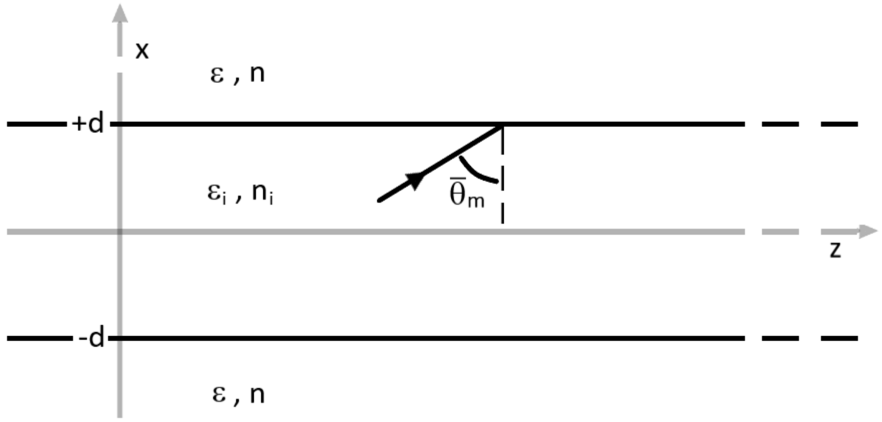

Figure 1.1: slab waveguide scheme.

We can choose a set of symmetric solutions for the different defined zones and then match the boundaries conditions.

$$\begin{aligned} E_y &= A\cos k_x x e^{-j\beta z}, \quad |x| < d \\ E_y &= B e^{-j\beta z} e^{-\alpha_x x}, \quad x > d \\ &= B e^{-j\beta z} e^{\alpha_x x}, \quad x < -d \end{aligned} \tag{1.7}$$

The equations for $\boldsymbol{H}$ follow from Faraday's law.

Taking advantage of symmetry, we need to match the boundary conditions only at $x = d$. Evaluating E_y and H_z at $x = d$ and dividing the two equations gives

$$\begin{cases} A\cos k_x d = B e^{-\alpha_x d} & E_y(x=d) \\ -k_x A \sin k_x d = -\alpha_x B e^{-\alpha_x d} & H_z(x=d) \end{cases} \quad \text{and dividing} \quad \rightarrow \quad \tan k_x d = \frac{\alpha_x}{k_x} \tag{1.8}$$

We further have from the wave equation

$$\begin{aligned} \beta^2 - \alpha_x^2 &= \omega^2 \mu_0 \varepsilon \\ \beta^2 + k_x^2 &= \omega^2 \mu_0 \varepsilon_i \end{aligned} \tag{1.9}$$

Combining these two equations, we find a condition for the parameters

$$\frac{\alpha_x}{k_x} = \sqrt{\frac{\omega^2 \mu_0 (\varepsilon_i - \varepsilon)}{k_x^2} - 1} \tag{1.10}$$

The dispersion diagram, the dependence of the propagation constant β on frequency, is found by constructing an intersection in Fig. 1.2 of the functions $\tan k_x d$ and α_x / k_x for each frequency and mode and then evaluating β from Eq. 1.9. For decreasing ω, α_x/k_x moves toward the origin and intersections are lost, except for the intersection with the first branch of the tangent function. This corresponds to the dominant mode, $m = 0$, with no cutoff. All higher order modes ($m > 0$) have a "cutoff"; they are not guided below a certain critical frequency, the cutoff-frequency.

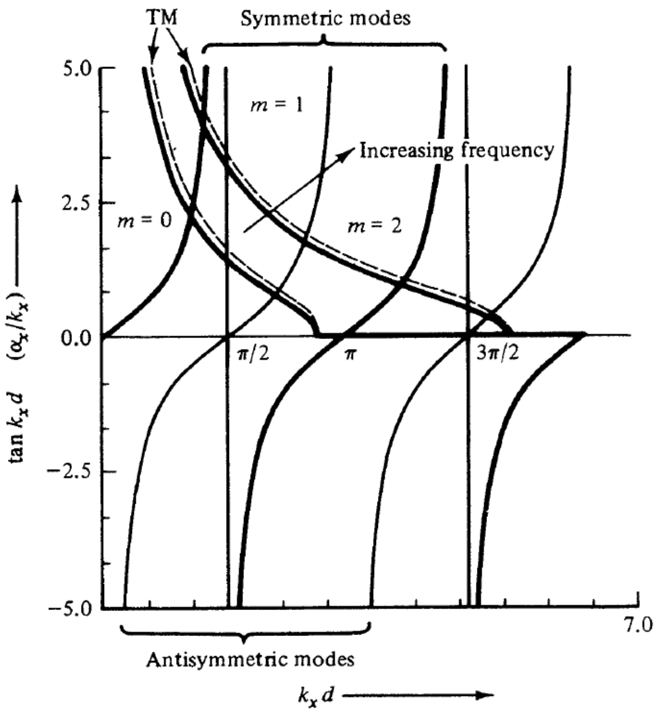

Figure 1.2: Graphical solution of Eq. 1.10 and Eq. 1.8. In dashed lines the TM modes. $\varepsilon_i/\varepsilon = 1$. Fig. duplicated from [15].

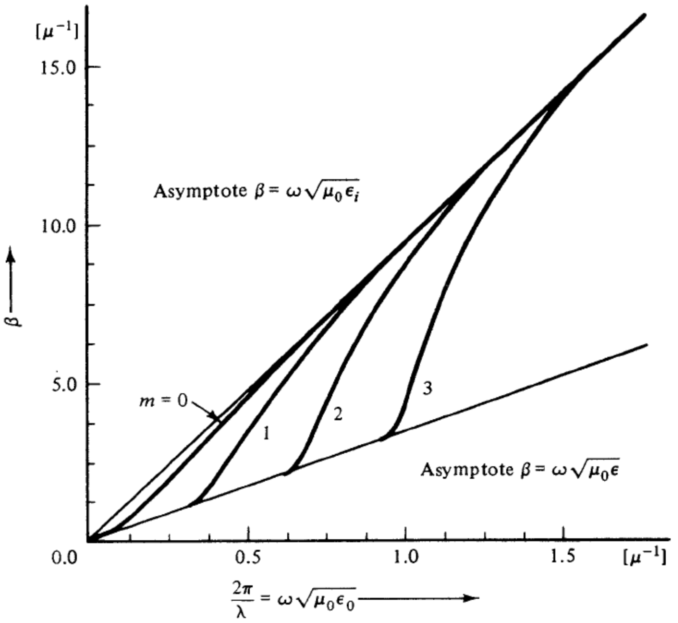

Figure 1.3: Dispersion diagram for TE waves in dielectric slab guide. $n_i = 9$, $n = 3.5$, $d = 0.6$ µm. The interior index is picked exaggeratedly large in order to separate the dispersion curves. Fig. duplicated from [15].

The dispersion curves of Fig. 1.3 are obtained by the use of Eq. 1.9, with the value of k_x for every frequency evaluated from Fig. 1.2.

Studying the dispersion curve for low-high frequency limits:

- For $\omega \to 0$, the fundamental mode acquires a small k_x. Hence $\tan k_x d \simeq k_x d$, and 1.10 and 1.8 yield

$$\omega^2 \mu_0 (\varepsilon_i - \varepsilon) d^2 - k_x^2 d^2 \simeq k_x^4 d^4 \tag{1.11}$$

  Neglecting $k_x^4 d^4$ compared with $k_x^2 d^2$, we have $k_x^2 = \omega^2 \mu_0 (\varepsilon_i - \varepsilon)$ and from 1.9, $\beta \simeq \omega\sqrt{\mu_0 \varepsilon}$. The wave propagates at the speed characteristic of the external region. This may be explained by the fact that most of the field is outside the slab at low frequencies.

- On the other hand, when $\omega \to \infty, k_x d$ approaches $\pi/2$ and we find from 1.9 that $\beta \simeq \omega\sqrt{\mu_0 \varepsilon_i}$. Now the propagation is at the speed characteristic of the interior of the slab.

The field is confined to the interior, as shown in Fig. 1.4. The pictured field is the simplest possible mode where the confinement just in the x dimension, so its a slab mode. With a further patterning also in the y dimension (following the same procedure for the x confinement) we can achieve a fully confined mode propagating in the z direction, such as the ones in proper waveguides.

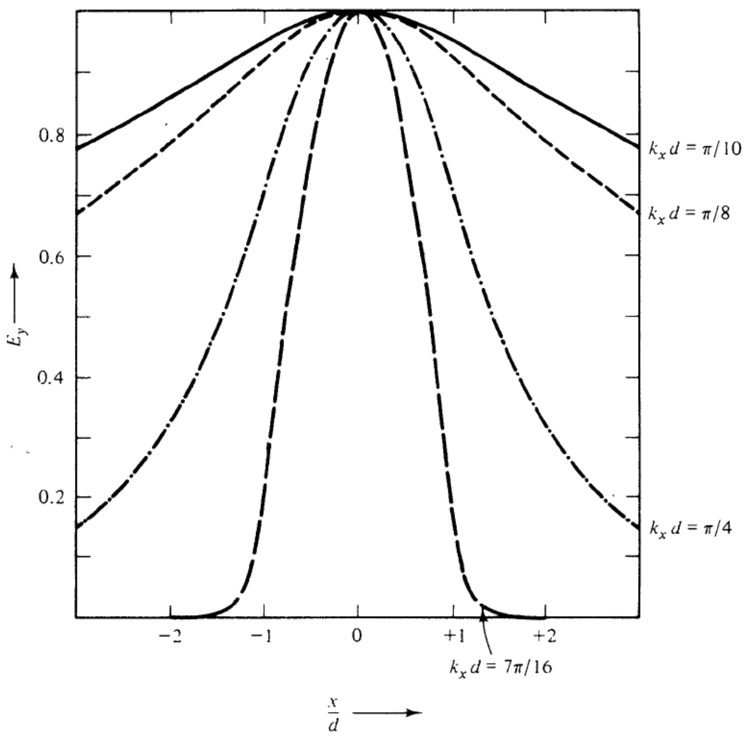

Figure 1.4: Profile of the electric field for three different frequencies. Fig. duplicated from [15].

1.2.3 Waveguide losses

Light transport through optical fibers and waveguides implies losses due to different factors. The main sources of power loss while propagation are:

- Scattering loss, due to surface roughness and impurities inside the core material,

- Absorption loss, due to photons annihilated inside the material,
- Radiation loss, due to curves, macro- and micro-bending of the waveguide.

To quantitatively describe the optical loss, the exponential attenuation coefficient α is generally used. In this case, the intensity (power per unit length) decays along the waveguide in the z direction

$$I(z) = I_0 \exp(-\alpha z) \quad I_0 \text{ is the initial intensity at z} = 0 \tag{1.12}$$

The attenuation coefficient α can be seen as a sum of different terms,

Scattering loss This kind of loss is given by two contributes, volume scattering and surface scattering. Volume scattering is caused by impurities in the composition and homogeneity of the material such as contaminations or crystalline defects if the used material is meant to be crystalline, or crystallization if it's meant to be amorphous. Surface scattering instead, is caused by the roughness of the waveguide walls, often given by deposition processes or lithography used for the structure realization.

A complete model for radiation loss arising from scattering by surface roughness of the waveguide walls is derived in [16]. We will call the portion of the exponential attenuation coefficient α relative to the surface scattering loss as α_s.

$$\alpha_s = \varphi^2(d)\left(n_i^2 - n^2\right)^2 \frac{k_0^3}{4\pi n_i} \int_0^{\pi} \tilde{R}\left(\beta - n k_0 \cos\theta\right) d\theta \tag{1.13}$$

where n_i and n are respectively the refractive indices of core and cladding materials, $\varphi(d)$ is the modal field evaluated at the interface, β the modal propagation constant and k_0 the e free-space wavenumber. The surface roughness of the waveguide walls is described by the spectral density function $\tilde{R}(\Omega)$, which is related to the autocorrelation function (ACF) $R(u)$ of the surface roughness through the Fourier transform

$$\tilde{R}(\Omega) = \int_{-\infty}^{\infty} R(u) \exp(\mathrm{i}\Omega u) \mathrm{d}u \tag{1.14}$$

The surface roughness is characterized by a correlation length L_c, and mean square deviation σ^2 from a flat surface. The parameter σ^2 is related to the autocorrelation function $R(u)$ by

$$\sigma^2 = R(0) \tag{1.15}$$

The modal field $\varphi(y)$ used in Eq 1.13 1 is normalized so that

$$\int_{-\infty}^{\infty} \varphi^2(y) \mathrm{d}y = 1 \tag{1.16}$$

In Fig. 1.5 the waveguide with surface roughness is schematized.

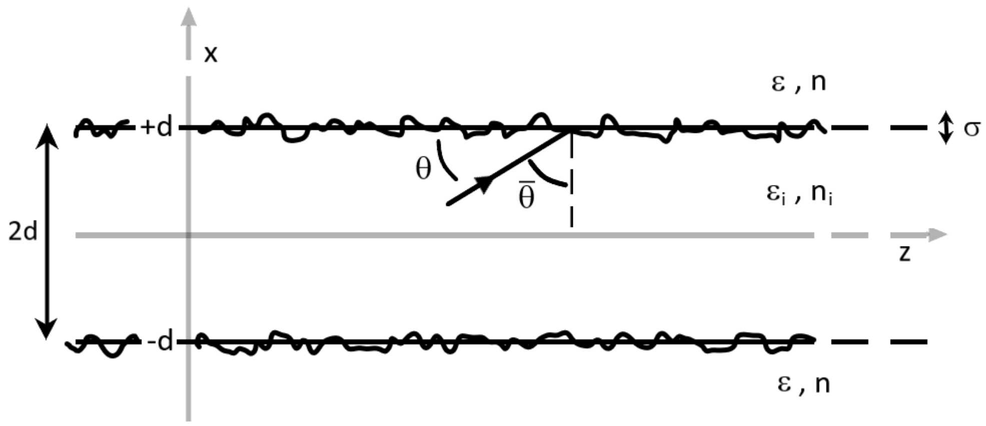

Figure 1.5: Geometry of the planar waveguide used for the derivation of Equation 1. The surface roughness is described by the r.m.s, deviation σ from flatness of an unperturbed waveguide of width 2d. The incident TE mode has a propagation constant β.

The result is then analytical calculated for specific ACFs in [17], highlighting some insight over the waveguide structural parameters. Another crucial aspect regarding surface scattering loss is the dependency on the mode. Higher order modes are more affected by this kind of loss process. This can quite easily understood considering that higher modes have a smaller $\bar{\theta}_m$ and therefore are reflected more times than lower order modes in the same Δz.

Absorption loss Absorption is the source of attenuation that convert optical power into another energy form such as heat. The causes for this kind of loss are two: *intrinsic*, due to band structure of the fiber material or *extrinsic*, due to impurities that modify the very same band structure. *Intraband* and *free carrier absorption* are two among the intrinsic sources of absorption attenuation.

To give an example, using the Drude's model, it's straightforward to link the complex refractive index of the core material to the *free carrier absorption* attenuation coefficient α_{fca}. The motion of an electron in an oscillating electric field $E_0 \exp(i\omega t)$ can be written as

$$x = \frac{eE_0/m^*}{\omega^2 - i\omega g} \exp(j\omega t) \tag{1.17}$$

where m^* is the effective mass of the electron in a specific band and g is the motion damping coefficient due to scattering and is linked to the mobility $\mu = e/m^* g$. Then, considering the polarization $p = -Nex$, (N density of free carriers) is possible to arrive to the complex electric susceptibility:

$$\begin{aligned} \chi &= n_0^2 - \frac{\left(Ne^2\right)/\left(m^*\varepsilon_0\right)}{\omega^2 - i\omega g} = \chi' + i\chi'' \\ \chi' &= n_0^2 - \frac{\left(Ne^2\right)/\left(m^*\varepsilon_0\right)}{\omega^2 + g^2} = n'^2 \\ \chi'' &= -\frac{\left(Ne^2 g\right)/\left(m^*\omega\varepsilon_0\right)}{\omega^2 + g^2} \end{aligned} \tag{1.18}$$

Where n_0 is the refractive index of the medium not considering the free carriers. From here is possible to write α_{fca} as:

$$\alpha_{fca} = -2k_0 n'' \approx -k_0 \frac{\chi''}{n} = \frac{Ne^3}{m^{*2} n \varepsilon_0 \omega^2 \mu c} \quad (\omega \gg g) \tag{1.19}$$

The free carrier absorption is proportional to the carrier density and the refractive index is also affected by the free carriers. This kind of absorption is therefore present in certain materials, where free carriers can be excited, such as metals or semiconductors.

For our particular interest, the band-to-band transitions give an important contribute to absorption losses, especially at short wavelengths. Most materials used in integrated photonics have absorption edges above the UV - e.g. Si, GaAs, Ge, InP, etc, and that is part of our challenge. HfO_2 is an interesting candidate (along Al_2O_3) due to a much lower edge, with a photon energy $E_\gamma = 5 - 6$ eV (250-200 nm).

Confinement factor We can define the *confinement factor* Γ of a guided mode in a waveguide as the ratio between the time-averaged z-component module of the Poynting vector integrated over the core and integrated over its total support (here we assume the propagation direction parallel to $\hat{\boldsymbol{z}}$, as in figure 1.5):

$$\Gamma = \frac{\int_{core} |\langle S_z(x,y)\rangle| \, dxdy}{\int_{-\infty}^{+\infty} |\langle S_z(x,y)\rangle| \, dxdy} \tag{1.20}$$

Through the calculation of the confinement factor in a given waveguide geometry and a measurement of the guided mode optical loss (assuming that the total loss is dominated by material loss) we can back out the material loss by simply:

$$L_{\text{material}} = \frac{L_{\text{guided mode}}}{\Gamma} \tag{1.21}$$

This will be useful in Chapter 4 to compare the studied material in terms of losses and refractive index with another established waveguide material, alumina.

1.3 Deposition and characterization tools for thin films

In Chapter 4 we will present a study over an array of different films. Here we present the tools that have been protagonists both of the fabrication process, through deposition, and the optical characterization:

- the PEALD (*Plasma Enhanced Atomic Layer Deposition*) for the realization of the thin slabs
- a *Spectroscopic Ellipsometer*, for refractive index and thickness measurements
- a *Prism Coupler*, used to measure tha slab mode optical loss of the films

1.3.1 Plasma Enhanced Atomic Layer Deposition

Atomic layer deposition (ALD) is a material growth process that was introduced by Dr. Suntola in 1974. It is based on a pair of sequential, self-limiting, surface-mediated reactions that lead to a nominal layer-by-layer growth process for a wide range of oxides, nitrides, and metals and has become a key enabling technology in semiconductor manufacturing and a rapidly expanding number of other applications where ultrathin, conformal coatings can bring performance advantages.
The process generally involves four steps:

1. pulse of the precursor
2. purge of excess precursors and reaction by-products from the gas phase
3. pulse of the reactant
4. purge of the reaction products and excess reactants

The reaction between the precursor and reactant forms the nominal monolayer of choice and constitutes one ALD cycle, which can be repeated to build thickness of the desired material in a linear fashion [18].

In particular, Plasma-Enhanced ALD (PEALD) is used to expand the properties and application of thermal ALD materials and the number and types of materials beyond the material set available to thermal ALD. PEALD generally uses a plasma to create the reactant "pulse" in the ALD sequence. In Figure 1.6 is shown a scheme of the four steps in PEALD process.

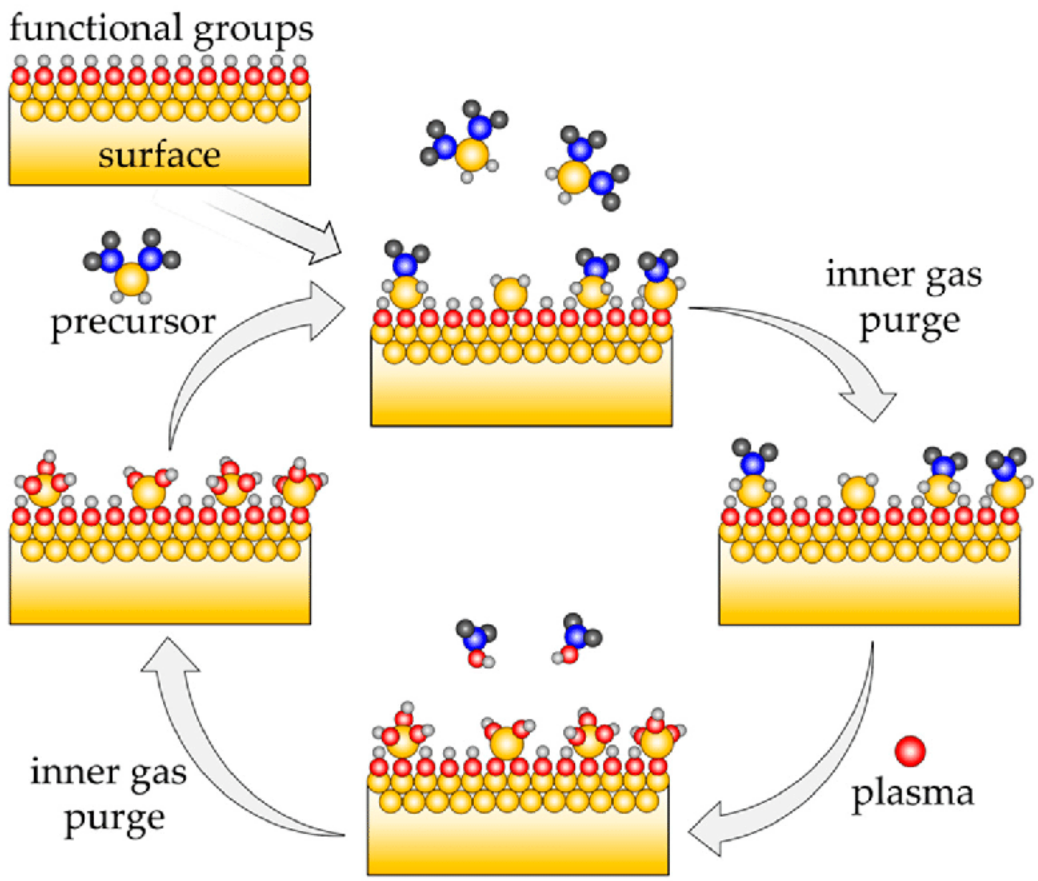

Figure 1.6: Scheme of the four steps of PEALD process. Fig. duplicated from [19].

In respect of the thermal ALD, PEALD allows for a wider choice of precursor chemistry with enhanced film quality:

- Plasma enables low-temperature ALD processes and the remote source maintains low plasma damage
- Eliminates the need for water as a precursor, reducing purge times between ALD cycles - especially for low temperatures

- Higher quality films through improved removal of impurities, leading to lower resistivity, higher density, etc
- Ability to control stoichiometry/phase

However some of the disadvantages of PEALD over ALD are [20]:

- More complicated reaction chemistry and reactor designs
- Potentially poor conformality and presence of plasma-induced damage

1.3.2 Spectroscopic ellipsometer

In this Section we are going to explain the basic working principle of the Spectroscopic ellipsometer used for refractive index and thickness characterization of thin films. The specific tool that was used is a SENTECH SE850 Ellipsometer.

An unpolarized light beam is emitted by a source at different wavelengths: after being linearly polarized and phase compensated it is reflected by the sample and collected by a detector. A scheme is shown in Fig. 1.7.

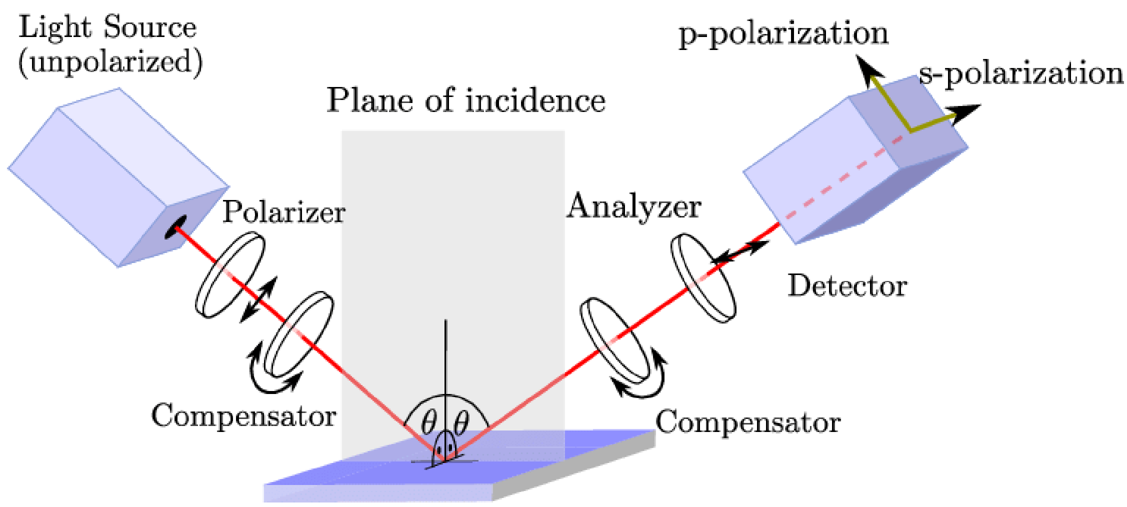

Figure 1.7: Scheme of the spectroscopic ellipsometer tool and working principle.

The detector measures the complex reflectance ratio $\rho = \frac{r_p}{r_s} = \tan\Psi e^{i\Delta}$, where r_p and r_s are the normalized amplitude components after reflection, $\tan\Psi$ is the real amplitude ratio and Δ is the phase shift. In order to maximize $\tan\Psi$, the incidence angle θ is set to $\theta \sim \theta_{\text{Brewster}} = \arctan\frac{n_2}{n_1}$ ($\theta_B \sim 70^o$ for most of the studied materials).

The light collected by the detector is the sum of many contributions in the two S and P polarizations: portion of the light is directly reflected at the air-material interface, another portion will be the result of as first refraction and a consecutive reflection on the second (from top) interface and so on [21]. Knowing approximately the layer structure of the sample, Ψ and Δ can be reconstructed thanks to Fresnel equations and then fitted on the data. From the fits is possible to get d, $n_{0,1,2}$ and $k_{0,1,2}$ in a range of $\lambda[360, 800]$ nm. These are parameters for the Cauchy's transmission equation:

$$
\begin{aligned}
n(\lambda) &= n_0 + \frac{n_1}{\lambda^2} + \frac{n_2}{\lambda^4} && \text{refractive index} \\
\mathrm{k}(\lambda) &= k_0 + \frac{k_1}{\lambda^2} + \frac{k_2}{\lambda^4} && \text{absorption coefficient}
\end{aligned}
\tag{1.22}
$$

1.3.3 Prism coupler

In this section we are going to explain the basic working principle of the Prism coupler instrument used for refractive index and slab mode optical loss measurements of thin films. The specific tool that was used is a Metricon Model 2010/M.

As shown in Fig. 1.8, a polarized light beam enters in the prism by one side, totally reflects on the lower face and is refracted again out of the prism where a detector measures its intensity. For certain incidence angles $\theta_{1,m}$, the evanescent wave's wavevector along the horizontal - generated by the total reflection at the lower prism-air interface - matches to the wavevector of the guided mode in the film. This is called *phase-matching condition*. When satisfied, a dip in the detected intensity is observed and a slab mode is excited. Then, knowing the refractive index of the prism and the angle $\theta_{1,m}$ is possible to obtain for each mode m $\beta_m = nk_0 \cos\theta_m$ that is the propagation constant and $n_{eff} = n\cos\theta_m$ called effective refractive index of the mode. The coupling condition is $n_{\text{prism}} \cos\theta_p = n_{\text{eff}}$. With multiple modes, both d (thickness of the film) and n can be estimated [22]. The process can be iterated with different wavelengths to potentially obtain $n(\lambda)$ by a Cauchy's transmission equation fit, in Eq, 1.22.

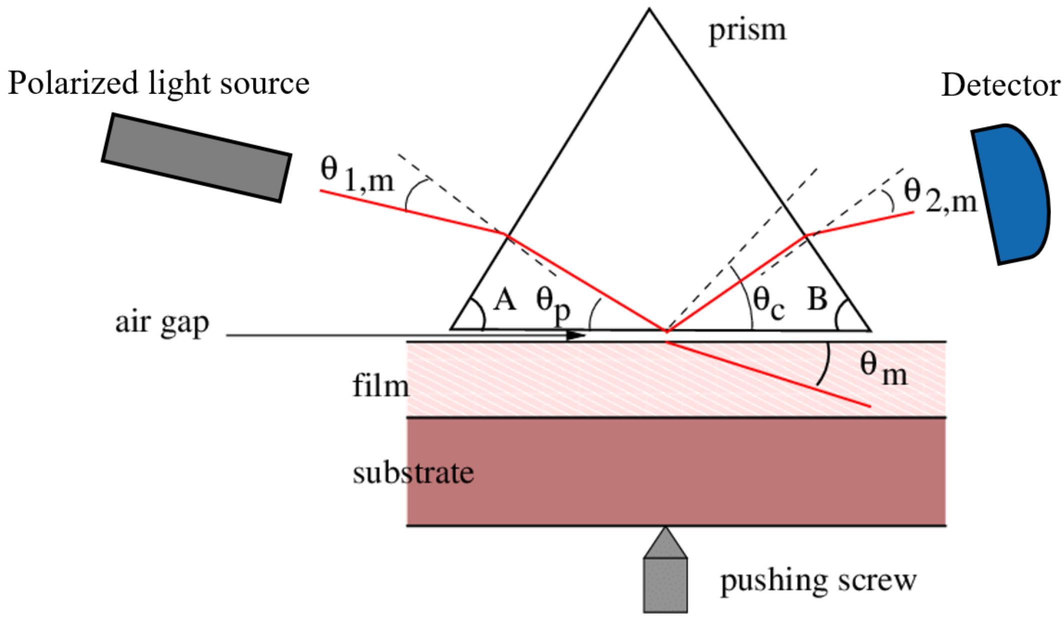

Figure 1.8: Scheme of the prism coupler tool and working principle for slab mode coupling in thin films.

Once the $\theta_{1,m}$ is fixed in order to observe a slab mode m and opportunely blocking the outcoupled light with a shield, the waveguide optical loss can be obtained by scanning a fiber optic probe down the length of a propagating streak to measure the light intensity scattered from the surface of the guide. The assumption is that at every point on the propagating streak the light scattered from the surface and picked up by the fiber is proportional to the light which remains within the guide. The best exponential fit to the resulting intensity vs distance (x) curve yields the loss in dB/cm. A scheme of the loss measurement module is presented in Fig. 1.9.

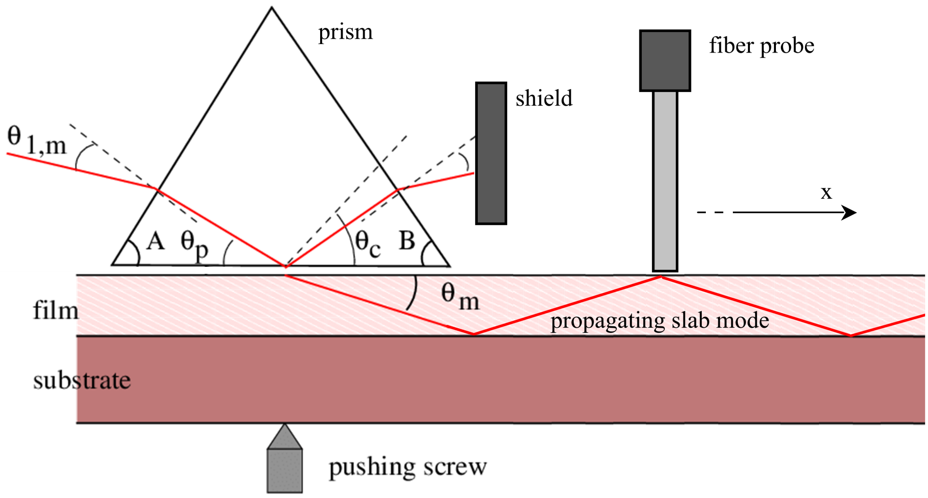

Figure 1.9: Scheme of the Metricon tool and working principle for slab mode loss measurements.

Chapter 2

Ring resonator circular polarization emitter - Theory

In Chapter 1, we introduced the importance of developing micro-metric devices able to outcouple focused beam in the preferred polarization state and wavelength. These then can be embedded underneath the electrodes layer that will be opportunely engineered with some conducting but optically transparent windows to let the emitted beams pass through. While structures that can radiate linearly-polarized light have already been designed and successfully implemented in such way [8], there is still lack of designs that can be suitable candidates to replace the free-space delivery method for circularly-polarized light currently used. Highly pure right and left-circular polarized light is indeed strictly necessary for multiple reasons. Depending on the ion chosen for the quantum system (some times even multiple species are required [23]), $\hat{\boldsymbol{\sigma}}_{\pm}$ polarized light at specific wavelengths is employed for many operations such as cooling, pumping for state preparation and read-out measurements. So far, the most successful attempts consist in circular resonators [24, 13], like the one we are going to present in the following Chapters, or micro-disks [25]. However, despite the remarkable results, all the previous works did not have the final purpose of having high polarization purity for high fidelity operations, crucial aspect in the trapped-ion quantum computation research. This feature was either not measured or not not very high. The highest reported value that we're aware of comes from more complex photonics circuits [26], that however need an active tuning. The maximum achieved polarization purity in these is 99%.

In this Chapter we will present a schematics of the studied device (the actual physical device is shown and described in Chapter 3) and we will discuss its working principle and how the radiated light can be modeled in an analytical way thanks to a classical diffraction theory. We will see that having an simple model that can describe the emission and fit the data is extremely useful in designing next generation high purity circular polarization emitters in order to improve performances. This process would be way more time demanding using just a fully numerical approach. Part of this Chapter, especially Section 2.1, is based on the content of a semester project by Tom Schatteburg, a previous student in TIQI Group [27].

2.1 Working principle

2.1.1 Device design

A ring resonator with an angular grating as shown in Fig. 2.1 theoretically allows the emission of almost purely circularly polarized light. In the following sections we will discuss about the general concept of an optical resonator, the optimal working conditions and then how the modes confined into the studied circular structure can be coupled into a radiated beam thanks to the diffraction grating.

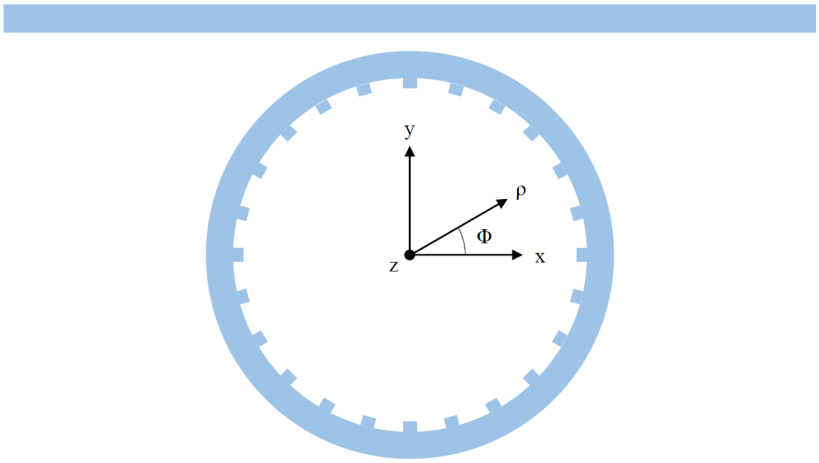

Figure 2.1: Scheme of the ring resonator with a feeding waveguide. On the inner boundary of the ring, grating elements are added to couple radiation out of the ring. z forms a optical axis due to the circular symmetry of the emission grating.

2.1.2 Optical Resonators

An optical resonator is a system in which light circulates and is fed back to its original state. Let's call the optical path length L which light rays travel until they reach their initial position again, and an attenuation factor which accounts for losses during one round-trip. The losses in a resonator can have many sources, from the partially reflecting mirrors in a Fabry-Perot etalon to impurities in the guiding material (as explained in Section 1.2.3) closed in a loop. Although this occurs only at specific positions in the resonator, we can usually 'distribute' the losses mathematically so that they are averaged over one round-trip.

Optical resonators have resonant modes at particular frequencies. The resonance condition is satisfied when the interference of the fed light from the exterior and the one fed back by the structure itself (due to its geometry, usually a closed path) is constructive. This means that additionally to spatial feedback, light also has to have its original phase when it reaches its initial position again. Otherwise, the light wave interferes destructively with itself so that these components are cancelled out. This means that only electric fields with wavelengths submultiples of the total optical path are self-consistent and can exist in the resonator. In the resonator of our interest, described in Section 2.1.1, the resonance condition is simply expressed by:

$$2\pi R = m\lambda_0/n_{eff} \tag{2.1}$$

where R is the circumference effective radius (where the propagation wavevector of the mode can be considered to lay), λ_0 is the wavelength in vacuum of the light inside the ring and n_{eff} is the effective refractive index of the guided mode with index m. In a circular resonator as the one we are presenting, such guided electric fields are called whispering gallery modes (WGMs).

2.1.3 Coupling Mechanism

Figure 2.2 shows a scheme of the coupling region at the gap between the feeding waveguide and the ring resonator, the following coupling model is based on [28]. The electric field guided inside the dielectric core is not totally confined, and it extends to the cladding, with intensity that decays exponentially with distance from the core, as evanescent wave. However in a coupling region, another structure is flanked to the bus waveguide, in this case the ring resonator. If the coupling gap is small enough, such as the evanescent tail of one of the bus waveguide modes overlaps with one mode of the gallery, a portion of the electric field propagating inside of the feeding waveguide can be coupled into the ring. There, it is guided again and does not lose amplitude by propagation.

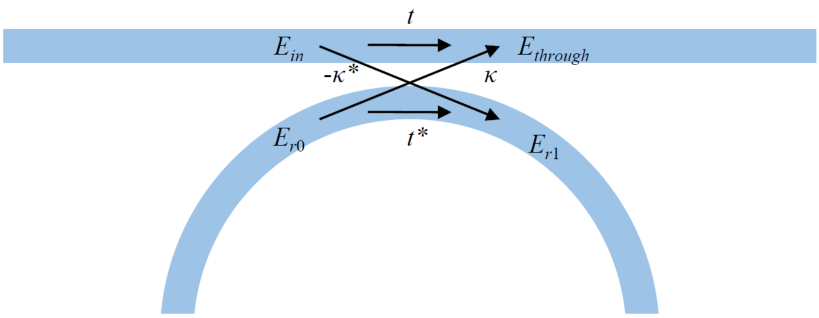

Figure 2.2: Scheme of the feeding region, from the bus waveguide to the ring resonator.

The different electric fields - now considered single complex quantities describing the amplitude of the mode - at the coupling region are related by Eq. 2.2.

$$\begin{pmatrix} E_{\text{through}} \\ E_{r1} \end{pmatrix} = \begin{bmatrix} t & \kappa \\ -\kappa^* & t^* \end{bmatrix} \begin{pmatrix} E_{\text{in}} \\ E_{r0} \end{pmatrix} \tag{2.2}$$

where E_{in} and E_{through} are the mode amplitudes in the feeding waveguide before and after the coupling, E_{r0} and E_{r1} are the electric fields in the ring before and after the coupling, t is the transmission coefficient and κ is the coupling coefficient. Energy conservation requires that the transmission matrix is unitary, so that $|t|^2+|\kappa|^2 = 1$. E_{r0} follows only from E_{r1} due to propagation of the electric field in the ring,

$$E_{r0} = E_{r1} e^{-\frac{\alpha}{2} 2\pi R} e^{i\phi} \tag{2.3}$$

where α is the intensity decay rate due to loss in the resonator, R is the radius in the ring and ϕ is the phase shift introduced in one round-trip. The transmitted field E_{through} can thus be expressed in terms of the input field E_{in}:

$$E_{\text{through}} = E_{\text{in}} \frac{te^{-i\phi} - e^{-\alpha\pi R}}{e^{-i\phi} - t^* e^{-\alpha\pi R}} \tag{2.4}$$

At resonance, there must be constructive interference between the field $t^* E_{r0}$ which propagates in the ring and the field E_{r1} added by the feeding waveguide. This means $\arg\{t^* E_{r0}\} = \arg\{E_{r1}\}$ and thus $\phi = \varphi_t$ up to a shift of a multiple of 2π, where φ_t is the phase of t. Then, Eq: 2.4 reduces to

$$E_{\text{through}} = E_{\text{in}}\, e^{i\varphi_t} \frac{|t| - e^{-\alpha\pi R}}{1 - |t|e^{-\alpha\pi R}} \tag{2.5}$$

Looking at the numerator, it follows that the transmitted field becomes zero for

$$|t| = e^{-\alpha\pi R} \tag{2.6}$$

which is the *critical coupling condition.* For these pairs of parameters $|t|$ and α, the field in the feeding waveguide interferes destructively with the field coupled back from the ring. This means all the input power is transferred into the ring, where it is lost through whatever mechanism causes the intensity decay rate α. In our structure, the values of $|t|$ and α are linked to the choice of two geometrical parameters, respectively the coupling gap width d and the grating amplitude g. It goes without saying that $|t|$ and α are also dependent on the material choice, the fabrication processes (especially α) and other factors. However it's easier to control the first two parameter in respect to the others. The major loss mechanism in the studied ring resonator, and hence the major contribution to α, is predominantly given by the grating situated in the inner side of the circumference, explicitly used to radiate the light into a perpendicular beam as we will discuss in Section 2.2.

We will see in the Chapter 3 that the *critical coupling condition* is indeed observed, choosing $|t|$ and α to satisfy Eq. 2.6. However we are interested in maximising both the radiated power in respect of the injected one, but more importantly the circular polarization purity of the radiated beam, that is also dependent on $|t|$ and α.

2.1.4 Coupling WGMs into radiated field

This Section is devoted to explaining how portion of the electric field of the propagating whispering gallery modes (WGMs) inside the waveguide can be radiated outside of the structure plane. We will explain why this can be achieved by matching the azimuthal mode index m to the number of grating elements q by a difference of 1.

As already introduced, circular resonators support whispering gallery modes (WGMs). Let's use angular propagation constant $\nu_{WGM} = \beta_m R$, which give the phase shift per unit azimuthal angle. R is the effective radius of the WGM and β_m is the propagation constant of the guided mode m. On resonance, the phase shift for one round trip has to be a multiple of 2π, so that $\nu_{WGM} = \beta_m R = m$. m is an integer which is called the azimuthal mode number and denotes the number of cycles that the light goes through when propagating one round-trip through the resonator. The electric field in the ring waveguide then takes the form

$$\boldsymbol{E}_{WGM} \propto \left(E_\rho \hat{\boldsymbol{\rho}} + E_\phi \hat{\boldsymbol{\phi}}\right) e^{i\phi m} \tag{2.7}$$

We can neglect the $\hat{\boldsymbol{z}}$ component (the one perpendicular to the circumference in Fig. 2.1) because, in our devices, we only couple into quasi-TE modes. E_ρ and E_ϕ are respectively the radial and azimuthal components of the electric field confined and propagating in the core. Due to circular symmetry, they are independent of angle ϕ, but in principle they do depend on position. A visualization is present in Fig. 2.4. At the grating elements, a part of the light is reflected and removed from the guided mode. According to Huygen's principle, each point where this occurs is the source of a new spherical wave. Each grating element can be regarded as quasi-point source for such a spherical wave. There are different phase shifts between these waves from neighboring grating elements due to different path lengths up to a given point in space. If the phase shift is an integer multiple of 2π, constructive interference occurs and light is radiated into this spatial direction. Oppositely, for uneven integer multiples of π, destructive interference is observed. Due to the circular symmetry of the problem, in case of constructive interference the wavefronts are circular as well and do not present any discontinuity. The radiated field will be described in detail in Section 2.2.1, but we can already introduce the general shape of this kind of outcoupled emission modes as:

$$\boldsymbol{E}_{rad} \propto \left(E_\rho \hat{\boldsymbol{\rho}} + E_\phi \hat{\boldsymbol{\phi}}\right) e^{i\phi l} \tag{2.8}$$

in a similar fashion as Eq. 2.7, where l is an integer. Similar to the Laguerre-Gaussian modes, they carry a total angular momentum of $l\hbar$ per photon. The azimuthal dependence manifests itself in helical wavefront, where l can be see in a geometrical representation as the number of helices in a *l-helix*.

To understand which radiation modes are excited by a waveguide mode we can calculate their coupling coefficient κ (different from the one mentioned in Eq. 2.2). It is given by

$$\kappa \propto \int_V \boldsymbol{E}^*_{rad} \Delta\epsilon \boldsymbol{E}_{WGM} dV \tag{2.9}$$

which is an overlap volume integral of the unperturbed field in the waveguide $\boldsymbol{E}_{WGM}$ with the radiated field $\boldsymbol{E}_{rad}$, mediated by the $\Delta\epsilon$. $\Delta\epsilon$ is the dielectric perturbation given by the grating; in our design the grating can be described as a square wave in the azimuthal direction with a contrast of $\Delta\epsilon = \epsilon_{core} - \epsilon_{cladding}$. The angular dependent parts are evaluated separately and $\Delta\epsilon$ is expanded in a Fourier series. Considering only the first term, it is given by $\Delta\epsilon \propto \sin(q\phi)$, where q is the number of grating elements. Then, each of the electric field vector components contributes to the coupling coefficient like the following:

$$\kappa \propto \int_0^{2\pi} e^{i(m+q-l)\phi} + e^{i(m-q-l)\phi} d\phi \tag{2.10}$$

For this integral to be non-zero, one of the exponents has to become zero. This gives the condition $l = m \pm q$. Since the radius of the radiation modes increases with l, a small structure like the azimuthal grating only overlaps with modes with small values of l. m and q are both numbers in the order of 10 to 100, so only the difference condition produces significant overlap. Thus, the azimuthal mode index l of the radiation is given by the difference between the azimuthal mode index m of the WGM and the number of grating elements q :

$$l = m - q \tag{2.11}$$

Then, the propagation constant of the radiation in z direction $\beta_{rad,z}$ is given by

$$\begin{aligned} \beta_{\text{rad, } z} &= \sqrt{(\beta_{rad})^2 - (\beta_{rad,\phi})^2} \\ &= \sqrt{\left(\frac{2\pi n_{surr}}{\lambda}\right)^2 - (\nu_{rad} R)^2} \end{aligned}$$

where n_{surr} is the refractive index of the cladding medium and λ is the free-space wavelength. Because of the circular symmetry, the general propagation is along the z direction.

2.1.5 Mode l dependency of the field polarization components

Before heading into a more accurate descriptive model of the radiated field in Section 2.2.1, we can briefly give an idea on how the polarization components of the emission are dependent on the azimuthal mode l. There are different conventions about the terminology of circular polarization. Here we use the unit vectors $\hat{\boldsymbol{\sigma}}_+ = \hat{\boldsymbol{R}} = \frac{1}{\sqrt{2}}(\hat{\boldsymbol{x}} - i\hat{\boldsymbol{y}})$ for right-handed circular polarization (RHCP) and $\hat{\boldsymbol{\sigma}}_- = \hat{\boldsymbol{L}} = \frac{1}{\sqrt{2}}(\hat{\boldsymbol{x}} + i\hat{\boldsymbol{y}})$ for left-handed circular polarization (LHCP), assuming the quantization axis to be parallel to $\hat{\boldsymbol{z}}$ for notation simplicity. In order to show the mentioned dependency on l, we can start from Eq. 2.8 (we can neglect the $\hat{\boldsymbol{z}}$ component, as it will be shown in Section 2.2.1), where $\hat{\boldsymbol{\rho}} = \cos\phi\hat{\boldsymbol{x}} + \sin\phi\hat{\boldsymbol{y}}$ and $\hat{\boldsymbol{\phi}} = -\sin\phi\hat{\boldsymbol{x}} + \cos\phi\hat{\boldsymbol{y}}$ are the unit vectors in radial and azimuthal direction, respectively. The transverse components of the radiated field $\boldsymbol{E}_{rad}$ can also be expressed in the basis of circular polarization:

$$\boldsymbol{E}_{rad} = E_+\hat{\boldsymbol{\sigma}}_+ + E_-\hat{\boldsymbol{\sigma}}_- \tag{2.12}$$

Then, by projection onto the basis vectors of circular polarization, E_+ and E_- are given by

$$\begin{aligned}
E_+ &= e^{il\phi}\left(E_\rho\hat{\boldsymbol{\rho}}\cdot\hat{\boldsymbol{\sigma}}_+ + E_\phi\hat{\boldsymbol{\phi}}\cdot\hat{\boldsymbol{\sigma}}_+\right)\\
&= e^{il\phi}\left(\frac{E_\rho}{\sqrt{2}}e^{-i\phi} - \frac{E_\phi}{\sqrt{2}}ie^{-i\phi}\right)\\
&= E_+(\rho,z)e^{i(l-1)\phi}\\
E_- &= e^{il\phi}\left(E_\rho\hat{\boldsymbol{\rho}}\cdot\hat{\boldsymbol{\sigma}}_- + E_\phi\hat{\boldsymbol{\phi}}\cdot\hat{\boldsymbol{\sigma}}_-\right)\\
&= e^{il\phi}\left(\frac{E_\rho}{\sqrt{2}}e^{i\phi} + \frac{E_\phi}{\sqrt{2}}ie^{i\phi}\right)\\
&= E_-(\rho,z)e^{i(l+1)\phi}\\
\text{with}\quad E_\pm(r,z) &= \mp i\frac{E_\phi \pm iE_\rho}{\sqrt{2}}
\end{aligned} \tag{2.13}$$

written in this form to be in the same one used in Eq. 2.27, Section 2.2.1. Although $E_\pm(r,z)$ is complex, it does not vary with angle ϕ or with time, so its phase stays constant. It is important to note that the amplitudes of right- and left-handed circularly polarized light do not have to be the same, but are determined by the relative amplitudes and phases of the radial and azimuthal components in the waveguide.

We now consider the case where $l = 1$. E_+ becomes independent of angle ϕ. For E_-, the angular dependence is given by $e^{i2\phi}$. With non-zero intensity, there would be a discontinuity at $\rho = 0$. Because this is nonphysical, the intensity on axis $\rho = 0$ must vanish. This applies more generally, so that all Laguerre-Gaussian modes with $l \neq 0$ have zero intensity on axis. In this case, this means that the $\hat{\boldsymbol{\sigma}}_-$ component vanishes at this point. The analogous argument leads to the conclusion that for $l = -1$, the transverse components of the light must be purely left-handedly ($\hat{\boldsymbol{\sigma}}_-$) polarized at the center of the $\rho - \phi$ plane.

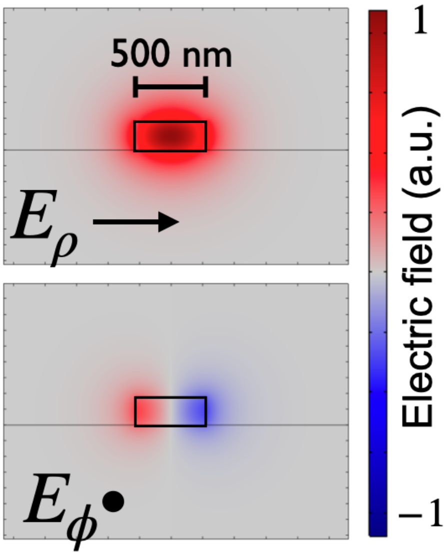

Figure 2.3: COMSOL Multiphysics simulation of the electric field components of a quasi-TE mode in a rectangular waveguide with the same characteristics of the studied resonator. Fig. duplicated from [27].

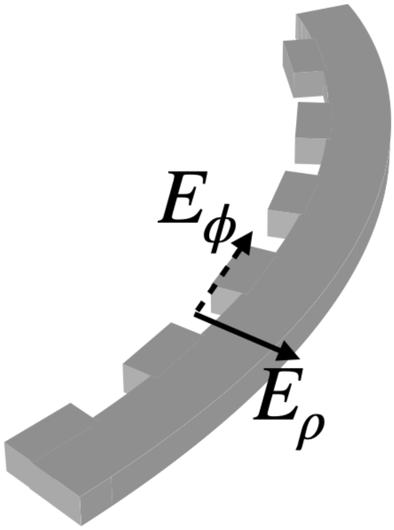

Figure 2.4: Graphical representation of the field components, parallel ($\boldsymbol{E}_\phi$) and perpendicular ($\boldsymbol{E}_\rho$) to the propagation direction ($\hat{\phi}$).

2.1.6 Simulations

Now we consider the state of polarization of light inside the waveguide. The geometry of the waveguides in this study is close to the one of a planar dielectric waveguide. The modes in this waveguide are quasi-TE modes, so that the electric field vector lies within the waveguide plane. From a previous work on this kind of circular resonator that simulated the emission and the WGMs [27] we know that, in the center of the waveguide where the intensity of the guided mode is highest, the electric field vector is transverse, which corresponds to radial polarization for a ring waveguide. In contrast, at the inner sidewall of the waveguide, which is where the grating is placed, the electric field vector has both transverse and longitudinal components (Fig. 2.3). In fact, due to strong confinement, the longitudinal components at the waveguide boundary can be of comparable strength as the transverse components [29]. From the perspective of a ring, this means a mixture of radial and azimuthal polarization with a $\pi/2$ phase shift between them [27]. As will be shown in the following section, the exact emitter state of polarization is not important for the reasoning to obtain purely circularly polarized light at one point. However, it does determine the overall ratio of the amplitudes of left-handed and right-handed circular polarization.

2.2 Radiated emission description

As expressed previously, it's useful to obtain a fairly detailed analytical model of the emission depending on the geometrical properties of the resonator in order to further optimize the device to achieve even better results.

2.2.1 Diffraction theory model

In this Section the main purpose is to model analytically the radiated electric field $\boldsymbol{E}(\rho, \phi, z)$ in any arbitrary spatial point $Q(\rho, \phi, z)$ (in cylindrical coordinates) thanks to a diffraction theory model. All coordinates and the parameters nouns used are represented in Figure 2.5.

The model is based on a more simple one, used in [13]. The field is emitted by the grating in the inner side wall of the circular waveguide composing the ring resonator. Each one of the q grating teeth is spaced equally in the ring circumference. Let's call $G_s(1, \phi_s, 0)$ the spatial points where the grating teeth are situated, each at an angle $\phi_s = 2\pi s/q$ with $s = 1, 2, ..., q$.

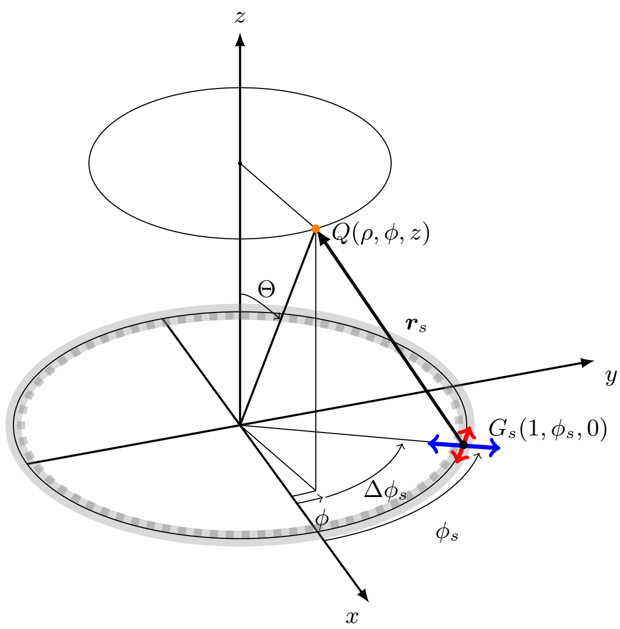

Figure 2.5: The ring has a nominal radius R normalized at 1. Every other spatial dimension is divided by R to get rid of the metric unit.

Inside of the circular waveguide a whispering gallery mode (WGM) is confined with dimensionless wavelength $\lambda \to \lambda/R$ and dimensionless wavenumber $\nu = \frac{2\pi}{\lambda}R$. The emitted electric field is produced by the diffraction of the propagating WGM partially scattered by each one of the grating tooth and it can be described as a superposition of dipole electric fields with $\boldsymbol{P}_s = (P_\phi \hat{\boldsymbol{\phi}}_s + P_\rho \hat{\boldsymbol{\rho}}_s)e^{i\phi l}$, situated at $G_s(1, \phi_s, 0)$ with $s = 1, 2, ..., q$. Each dipole $\boldsymbol{P}_s$ can be decomposed into two orthogonal components P_ϕ and P_ρ respectively along $\hat{\boldsymbol{\phi}}_s$ and $\hat{\boldsymbol{\rho}}_s$. These two components are dependent on the amplitude and the phase that the two components E_ϕ and E_ρ of WGM field have in each point G_s.

The field can be written as:

$$\begin{aligned}\boldsymbol{E}_l =&\boldsymbol{E}_l^\phi + \boldsymbol{E}_l^\rho \\ =&\frac{A}{R^3}\sum_{s=1}^{q}\left\{e^{i\nu r_s}e^{i\phi_s l}\left[\left(\frac{\nu^2}{r_s} - i\frac{\nu}{r_s^2} - \frac{1}{r_s^3}\right)(\hat{\boldsymbol{r}}_s \wedge \hat{\boldsymbol{\phi}}_s)\wedge\hat{\boldsymbol{r}}_s - \left(i\frac{2\nu}{r_s^2} + \frac{2}{r_s^3}\right)(\hat{\boldsymbol{r}}_s\cdot\hat{\boldsymbol{\phi}}_s)\hat{\boldsymbol{r}}_s\right]\right\} \\ +&\frac{B}{R^3}\sum_{s=1}^{q}\left\{e^{i\nu r_s}e^{i\phi_s l}\left[\left(\frac{\nu^2}{r_s} - i\frac{\nu}{r_s^2} - \frac{1}{r_s^3}\right)(\hat{\boldsymbol{r}}_s \wedge \hat{\boldsymbol{\rho}}_s)\wedge\hat{\boldsymbol{r}}_s - \left(i\frac{2\nu}{r_s^2} + \frac{2}{r_s^3}\right)(\hat{\boldsymbol{r}}_s\cdot\hat{\boldsymbol{\rho}}_s)\hat{\boldsymbol{r}}_s\right]\right\}\end{aligned} \tag{2.14}$$

where $A = P_\phi/4\pi\epsilon_0 = \chi E_\phi/4\pi$ and $B = P_\rho/4\pi\epsilon_0 = \chi E_\rho/4\pi$.
In the far field zone $z/\rho \gg 1$ and some approximations can be taken:

- The distance r_s can be expressed in $\mathcal{O}\left((\rho/z)\right)$ and orders > 1 can be neglected.

$$
\begin{aligned}
r_s = \sqrt{z^2 + (1^2 + \rho^2 - 2\rho\cos\Delta\phi_s)} = z\sqrt{1 + \frac{1+\rho^2 - 2\rho\cos\Delta\phi_s}{z^2}} \simeq \\
\simeq z\left(1 + \frac{(1+\rho^2)}{2z^2} - \frac{\tan\Theta\cos\Delta\phi_s}{z}\right) = z + \frac{(1+\rho^2)}{2z} - \tan\Theta\cos\Delta\phi_s
\end{aligned}
$$

given $\rho/z = \tan\Theta$. Then, calling

$$
\Phi(\rho, z) = e^{i\nu\left(z+\frac{(1+\rho^2)}{2z}\right)},
$$

$e^{i\nu r_s}$ can be expressed as

$$
e^{i\nu r_s} = \Phi(\rho, z)e^{-i\nu\tan\Theta\cos\Delta\phi_s}. \tag{2.15}
$$

- The terms in Eq. 2.14 that are proportional to $1/r_s^2$ and $1/r_s^3$ are negligible compared to the terms proportional to $1/r_s$, which can be treated as $1/z$.

Thanks to these two approximation, the explicit leading vectorial terms of the field (calculated in Appendix section 6), we can express the field components in cylindrical coordinates in a simpler way:

$$
\begin{aligned}
E_{\rho,l}(\rho,\phi,z) = E^{\phi}_{\rho,l}(\rho,\phi,z) + E^{\rho}_{\rho,l}(\rho,\phi,z) = &-\frac{A}{R^3}\frac{\nu^2}{z}\Phi(\rho,z)\sum_{s=1}^{q} e^{-i\nu\tan\Theta\cos\Delta\phi_s}e^{il\phi_s}\sin\Delta\phi_s + \\
&+\frac{B}{R^3}\frac{\nu^2}{z}\Phi(\rho,z)\sum_{s=1}^{q} e^{-i\nu\tan\Theta\cos\Delta\phi_s}e^{il\phi_s}\cos\Delta\phi_s \\
E_{\phi,l}(\rho,\phi,z) = E^{\phi}_{\phi,l}(\rho,\phi,z) + E^{\rho}_{\phi,l}(\rho,\phi,z) = &+\frac{A}{R^3}\frac{\nu^2}{z}\Phi(\rho,z)\sum_{s=1}^{q} e^{-i\nu\tan\Theta\cos\Delta\phi_s}e^{il\phi_s}\cos\Delta\phi_s + \\
&+\frac{B}{R^3}\frac{\nu^2}{z}\Phi(\rho,z)\sum_{s=1}^{q} e^{-i\nu\tan\Theta\cos\Delta\phi_s}e^{il\phi_s}\sin\Delta\phi_s \\
E_{z,l}(\rho,\phi,z) = E^{\phi}_{z,l}(\rho,\phi,z) + E^{\rho}_{z,l}(\rho,\phi,z) = &+\frac{A}{R^3}\frac{\nu^2}{z^2}\Phi(\rho,z)\sum_{s=1}^{q} e^{-i\nu\tan\Theta\cos\Delta\phi_s}e^{il\phi_s}\rho\sin\Delta\phi_s + \\
&+\frac{B}{R^3}\frac{\nu^2}{z^2}\Phi(\rho,z)\sum_{s=1}^{q} e^{-i\nu\tan\Theta\cos\Delta\phi_s}e^{il\phi_s}\left(1-\rho\cos\Delta\phi_s\right)
\end{aligned} \tag{2.16}
$$

It can also be interesting to notice that, following these approximations, we arrive at the following relations:

$$
\begin{aligned}
E^{\rho}_{\rho,l}(\rho,\phi,z) = +\frac{B}{A}E^{\phi}_{\phi,l}(\rho,\phi,z) \\
E^{\rho}_{\phi,l}(\rho,\phi,z) = -\frac{B}{A}E^{\phi}_{\rho,l}(\rho,\phi,z)
\end{aligned} \tag{2.17}
$$

From now on we will just consider the transverse field components $E_{\rho,l}(\rho,\phi,z)$ and $E_{\phi,l}(\rho,\phi,z)$, since the vertical component $E_{z,l}(\rho,\phi,z)$ is an $\mathcal{O}\left((\rho/z)^2\right)$ and therefore subdominant in the far field zone. By taking an approximate integral representation of the Bessel function of the first kind ($2\pi/q \ll 1$):

$$\sum_{s=1}^{q} \exp\left(-i\nu \tan\Theta \cos\Delta\phi_s\right) \exp\left(in\Delta\phi_s\right) \approx i^n q J_n(-\nu\tan\Theta) \tag{2.18}$$

And using the two following properties for Bessel function of the first kind

$$\begin{aligned} J_{n-1}(x) + J_{n+1}(x) &= \frac{2n}{x} J_n(x) \\ J_{n-1}(x) - J_{n+1}(x) &= 2\frac{dJ_n(x)}{dx} \end{aligned} \tag{2.19}$$

It's straightforward to arrive at the final and compact form for the two transverse field components:

$$\begin{aligned} E_{\rho,l}(\rho,\phi,z) = E^{\phi}_{\rho,l}(\rho,\phi,z) + E^{\rho}_{\rho,l}(\rho,\phi,z) =& i^l \frac{\nu q}{R^3}\Phi(\rho,z)e^{il\phi}\left\{\frac{Al}{\rho}J_l(-\nu\tan\Theta) - i\frac{B\nu}{z}J_l'(-\nu\tan\Theta)\right\} \\ E_{\phi,l}(\rho,\phi,z) = E^{\phi}_{\phi,l}(\rho,\phi,z) + E^{\rho}_{\phi,l}(\rho,\phi,z) =& i^l \frac{\nu q}{R^3}\Phi(\rho,z)e^{il\phi}\left\{-i\frac{A\nu}{z}J_l'(-\nu\tan\Theta) - \frac{Bl}{\rho}J_l(-\nu\tan\Theta)\right\} \end{aligned} \tag{2.20}$$

Now, with a basis change, we can find the two Right and Left hand circular polarized (R/LHCP) components of the transverse field in the $B'' = \left\{\hat{R} = (\hat{\boldsymbol{x}} - i\hat{\boldsymbol{y}})/\sqrt{2}, \hat{L} = (\hat{\boldsymbol{x}} + i\hat{\boldsymbol{y}})/\sqrt{2}, \hat{z}\right\}$ basis.

$$\begin{pmatrix} E_R \\ E_L \end{pmatrix} = \frac{1}{\sqrt{2}}\begin{bmatrix} e^{-i\phi} & -ie^{-i\phi} \\ e^{i\phi} & ie^{i\phi} \end{bmatrix}\begin{pmatrix} E_\rho \\ E_\phi \end{pmatrix} \tag{2.21}$$

The two final components are:

$$\begin{aligned} E_{R,l}(\rho,\phi,z) &= i^l\frac{\nu q}{\sqrt{2}R^3}\Phi(\rho,z)e^{il\phi}\left\{e^{-i\phi}\left(\frac{Al}{\rho}J_l - i\frac{B\nu}{z}J_l'\right) - e^{-i\phi}\left(\frac{A\nu}{z}J_l' - i\frac{Bl}{\rho}J_l\right)\right\} \\ E_{L,l}(\rho,\phi,z) &= i^l\frac{\nu q}{\sqrt{2}R^3}\Phi(\rho,z)e^{il\phi}\left\{e^{i\phi}\left(\frac{Al}{\rho}J_l - i\frac{B\nu}{z}J_l'\right) + e^{i\phi}\left(\frac{A\nu}{z}J_l' - i\frac{Bl}{\rho}J_l\right)\right\} \end{aligned} \tag{2.22}$$

with $J_l = J_l(-\nu\tan\Theta)$ and $J_l' = J_l'(-\nu\tan\Theta)$.

In order to visualize in the best way how the emission polarization depends on the relation between A and B we can express again the two circular polarized components as

$$\begin{aligned} E_{R,l}(\rho,\phi,z) &= i^l\frac{\nu q}{\sqrt{2}R^3}\Phi(\rho,z)e^{i(l-1)\phi}\left(\frac{l}{\rho}J_l - \frac{\nu}{z}J_l'\right)(A+iB) \\ E_{L,l}(\rho,\phi,z) &= i^l\frac{\nu q}{\sqrt{2}R^3}\Phi(\rho,z)e^{i(l+1)\phi}\left(\frac{l}{\rho}J_l + \frac{\nu}{z}J_l'\right)(A-iB) \end{aligned} \tag{2.23}$$

Then, calling the argument of the Bessel function as $\zeta = -\nu\tan\Theta = -\nu\rho/z$ we can write the term

$$\left(\frac{l}{\rho}J_l \mp \frac{\nu}{z}J_l'\right) = -\frac{\nu}{z}\left(\frac{l}{\zeta}J_l(\zeta) \pm J_l'(\zeta)\right) \tag{2.24}$$

and using the recurrence relations

$$\begin{cases} J_l'(\zeta) = \frac{d}{d\zeta}J_l(\zeta) = \frac{1}{2}\left(J_{l-1}(\zeta) - J_{l+1}(\zeta)\right) \\ J_l(\zeta) = \frac{\zeta}{2l}\left(J_{l-1}(\zeta) + J_{l+1}(\zeta)\right) \end{cases} \tag{2.25}$$

we arrive to

$$\left(\frac{l}{\rho}J_l \mp \frac{\nu}{z}J_l'\right) = -\frac{\nu}{z}J_{l\mp1}(\zeta) \tag{2.26}$$

Substituting once again the dummy parameters A and B in order to highlight the dependency of the radiated field on E_ϕ and E_ρ, we obtain:

$$E_{rad,\sigma_\pm,l}(\rho,\phi,z) = K\Phi(\rho,z)e^{i(l\mp1)\phi}J_{l\mp1}\left(E_\phi \pm iE_\rho\right) \tag{2.27}$$

$$\text{with} \quad \begin{cases} K = -\frac{i^l\nu^2 q\chi}{4\sqrt{2}\pi z R^3} & \text{global factor} \\ \Phi(\rho,z) = e^{iv\left(z+\frac{1+\rho^2}{2z}\right)} & \text{global phase} \\ J_l = J_l(-\nu\tan\Theta) & \text{Bessel function 1}^{\text{st}} \text{ kind order } l \\ E_\phi = |E_\phi| & \text{azimuthal component of the WGM} \\ E_\rho = |E_\rho|\,e^{i\Delta\varphi} & \text{radial component of the WGM} \end{cases} \tag{2.28}$$

where we called the RHCP and LHCP respectively $\hat{\boldsymbol{\sigma}}_+$ and $\hat{\boldsymbol{\sigma}}_-$, assuming the quantization axis to be parallel to $\hat{\boldsymbol{z}}$ for notation simplicity.

2.2.2 Considerations on the model

Now that we have an analytical model, it's possible to understand how to enhance just one of the two components in order to have a micro-metric device, that can be integrated in ion traps and able to address highly pure $\hat{\boldsymbol{\sigma}}_\pm$ light. This radiated field could be used for operations on single ions.

Let's go back to Eq. 2.27: we can notice that, aside of a global factor and a global phase, there are two terms of interest

$$E_{rad,\sigma_\pm,l}(\rho,\phi,z) = K\Phi(\rho,z)e^{i(l\mp1)\phi}\underbrace{J_{l\mp1}}_{①}\underbrace{\left(E_\phi \pm iE_\rho\right)}_{②}$$

The term ① is dependent on the azimuthal mode number l and it also contains the spatial dependency. The term ② instead, highlights the dependency on the WGM components of the field inside the wavewguide. We can exploit both terms in order to maximize one $\hat{\boldsymbol{\sigma}}$ component in respect of the other:

① By selecting the right mode m (so selecting the m-th resonance frequency by tuning the wavelength of the light injected into the bus waveguide), we can choose which mode l is radiated.

Since $J_l(-\nu\tan\Theta = 0) \neq 0$ just for $l = 0$, we have intensity on axis $\rho = 0$ only for the $\hat{\boldsymbol{\sigma}}_\pm$ component when $l = \mp1$ respectively. In particular, choosing $l = 1$ (so $m = q + 1$), on the axis $= 0$, the $\hat{\boldsymbol{\sigma}}_-$ polarization component goes to zero:

$$\begin{aligned} E_{rad,\sigma_-,l=1}(\rho = 0) &= 0 \\ E_{rad,\sigma_+,l=1}(\rho = 0) &\neq 0 \end{aligned} \tag{2.29}$$

This nice feature of the emitted field can be very useful for multiple reasons: firstly, the spatial distribution shows a Gaussian-like beam on axis $\rho = 0$ in $E_{rad,\sigma_+,l=1}$ that can be use to address single ions if these are kept trapped above the ring resonator. For instance, in the studied device in Chapter 4, the HWHM of the central spot at $z \sim 50\mu\text{m}$ is about $\sim 1\mu\text{m}$. This could fit with the usual dimension scales in state of the art surface traps, where ions are usually trapped $\sim 50\mu$m above the gold electrodes and kept at a distance one from the other of $\sim 4\mu$m. Secondly, at the center of the beam, one of the two field components is orders of magnitude higher than the other. This assures that for the mode $l = 1$ we manage to have a highly pure $\hat{\boldsymbol{\sigma}}_+$ polarized beam, a very not trivial property ($\hat{\boldsymbol{\sigma}}_-$ if the light is coupled into the ring in the opposite sense, so with anti-parallel propagation direction).

A visualization of the emission pattern for the two components $E_{\sigma_\pm}$ is presented in Fig. 2.6, a simulation of the field in the $l = 1$ mode.

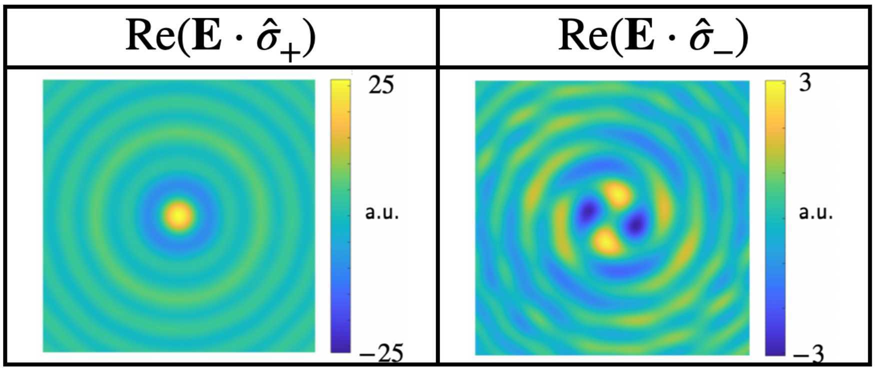

Figure 2.6: Lumerical simulation of the radiated field in mode $l = 1$, using the FDTD method. Fig. duplicated from [27].

② In the second term instead the dependency on the WGM electric field components $E_{\phi,\rho}$ is shown. Writing the two components as in Eq: 2.28, we can arrive to an interesting relation between these two.

$$\begin{cases} E_\phi = |E_\phi| & \text{azimuthal component of the WGM} \\ E_\rho = |E_\rho|\, e^{i\Delta\varphi} & \text{radial component of the WGM} \end{cases}$$

with $\Delta\varphi$ the relative phase between the two E_ρ and E_ϕ.
Now we can write again the second term as:

$$② \propto \left(1 \pm e^{i(\Delta\varphi+\pi/2)} \frac{|E_\rho|}{|E_\phi|}\right) \tag{2.30}$$

where the $+(-)$ is for the $\hat{\boldsymbol{\sigma}}_+(\hat{\boldsymbol{\sigma}}_-)$ component.
If $\Delta\varphi = -\pi/2$ (so there's a $-i$ phase between E_ρ and E_ϕ), then $\exp i(\Delta\varphi + \pi/2) = 1$. From the Helmholtz equation inside the waveguide, in a anticlockwise propagating mode inside the ring the two E_ρ and E_ϕ have indeed this phase relation (while it's opposite for the clockwise propagating direction). So, choosing one propagation direction (anticlockwise in the studied case), Eq. 2.30 becomes

$$② \propto \left(1 \pm \frac{|E_\rho|}{|E_\phi|}\right) \tag{2.31}$$

The $|E_\rho|/|E_\phi|$ ratio depends on the field spatial distribution of the WGM and therefore on the sizes of the rectangular section of the waveguide core.
In the particular limit $|E_\rho|/|E_\phi| \sim 1$

$$\lim_{|E_\rho|/|E_\phi| \to 1} E_{rad,\sigma_-,l}(\rho,\phi,z) = 0 \quad \forall l \tag{2.32}$$

The quite outstanding property is that this limit that brings to zero the $E_{rad,\sigma_-,l}$ component is valid no matter which mode l (m) we are selecting and no matter where in space we are looking (as long as the far field approximation is still valid).

However, term ① condition is more robust, because it just implies to be at resonance. Term ② instead, despite being ideally an even more powerful relation, requires exactly the right effective ratio between field components. For this purpose a simulation on the $|E_\rho|/|E_\phi|$ ratio has been conducted. Maintaining the same sizes of the core rectangular section (let's call the width w and the height h, in a very ingenious way), the ratio has been evaluated for different grating amplitudes in such a way:

$$\frac{|E_\rho|}{|E_\phi|} = \frac{\int_{\rho=R-w/2-g}^{\rho=R-w/2} |E_\rho(\rho, z = h/2)| d\rho}{\int_{\rho=R-w/2-g}^{\rho=R-w/2} |E_\phi(\rho, z = h/2)| d\rho} \tag{2.33}$$

considering no azimuthal dependency for the module of the field components and following the coordinate system in Fig. 2.7.

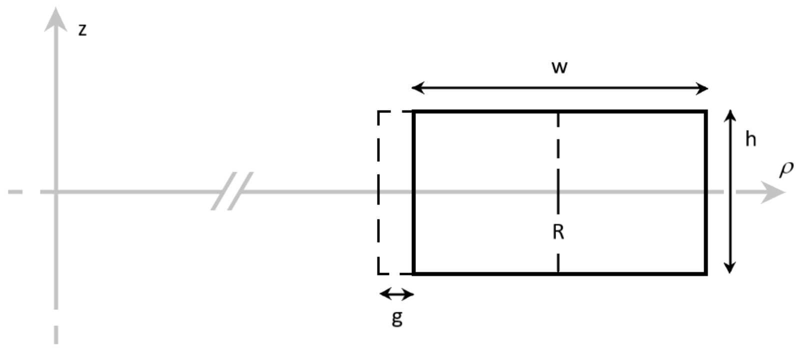

Figure 2.7: Coordinate system referenced with the waveguide core position. The ring is laying on the $z = 0$ plane and its center is congruent with the axes origin.

The field profiles used to evaluate the $|E_\rho|/|E_\phi|$ ratio thanks to Eq. 2.33 are the simulated ones shown in Fig. 2.3. The profiles of the two components are also plotted in Fig. 2.8.

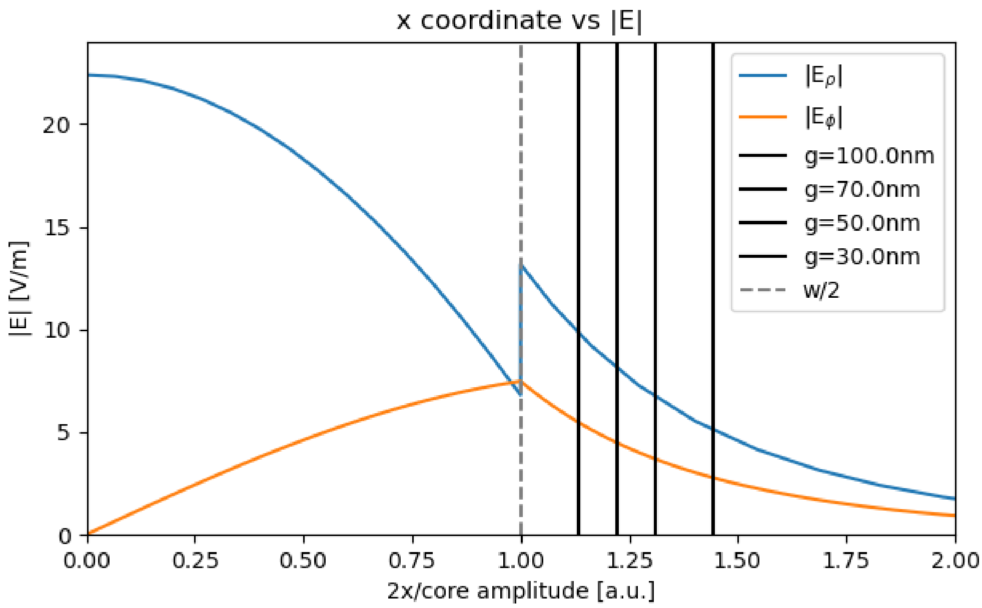

Figure 2.8: WGM component profiles vs normalized distance from the center of the core. In particular the dashed line represents the side wall of the core, while the solid lines represents different grating amplitudes g.

.

The results of the numerical evaluation of Eq. 2.33, considering 4 different grating amplitude values $g = [30, 50, 70, 100]$ nm (indeed the 4 grating amplitudes that we tested during Chapter 3) are plotted in Fig. 2.9.

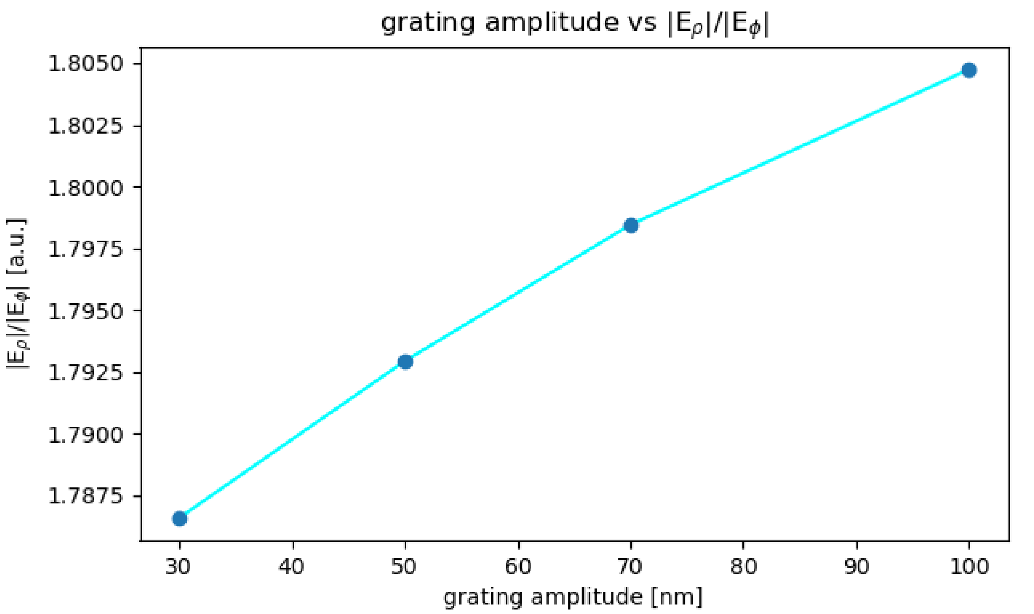

Figure 2.9: $|E_\rho|/|E_\phi|$ ratio as evaluated in Eq. 2.33 vs grating amplitude g.

.

We can observe that the ratio, for all the tested grating amplitudes, is quite off to be ~ 1. The two components, due to the choice of the core dimensions, are visibly quite different (see

Fig, 2.8), and even selecting the smaller available grating is not possible to lower the ratio below ~ 1.787. On the other hand, we are probably overestimating the ratio value. It would make more sense to consider the real value to be an average between the calculated one and the one at the interface inside the core that is closer to 1 in Fig 2.8.

Here again it's possible to highlight how the formulated model can be useful in designing the next generations ring resonator for having even higher polarization purity.

The physical devices that are presented and experimentally tested in Chapter 3, were fabricated before the diffraction model was formulated, so they are not optimized in these terms, especially for the properties coming from ②.

Chapter 3

Ring resonator circular polarization emitter - Experimental results

In this Chapter we will describe the ring resonator waveguide in its geometrical and material specifics. Then, after explaining the setup used to acquire all the measurements, we will undergo all the data acquisition together with the relative analysis and considerations.

3.1 Device

3.1.1 Design

The system is composed by a ring resonator flanked by a linear waveguide travelling from one facet to the other of the chip. The feeding (or bus) waveguide core doesn't maintain the same dimensions for all its length: it is wider and thinner near the input and output regions to facilitate the light in- and out-coupling and to reduce the optical losses, while in the central region, approaching the ring coupling zone, is tapered into a thicker and narrower bi-layer core [30]. The ring cross section is the same as the bus waveguide in the central zone. A schematics of a cross section of the whole chip (not in scale) is presented in Fig. 3.1, where are listed the materials and the thicknesses of the layers. The ring resonator has a nominal radius $R = 10$ µm and it be observed in a SEM image reported in Fig. 3.2. On the inner side of the circumference is also possible to observe the square 50% duty cycle grating with $q = 143$ elements (and hence q periods). In Fig. 3.3 the mode profiles in the two different core sections are shown, together with their widths.

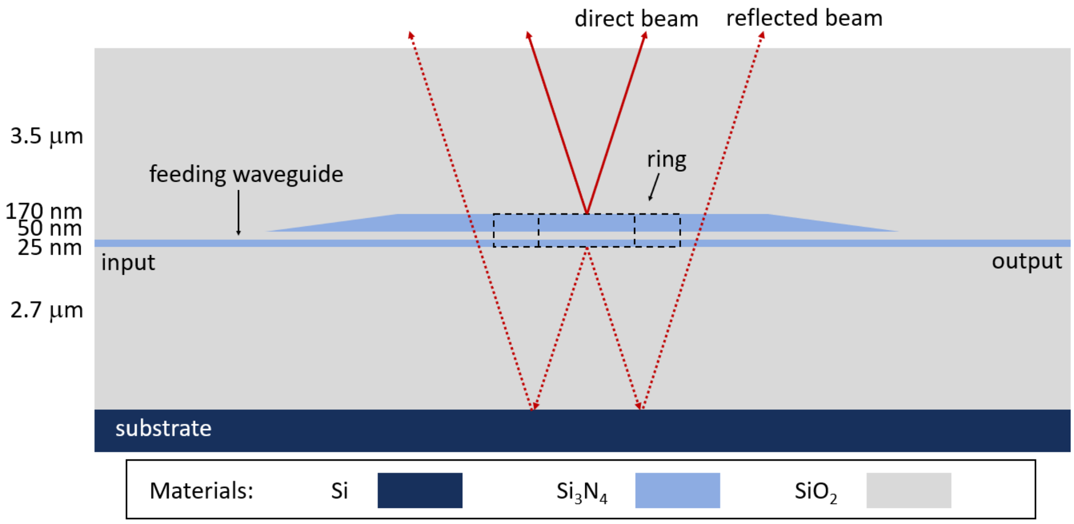

Figure 3.1: Cross section of the multi-layer chip structure (not in scale). The black dashed lines show the position of the ring. Below: legend for the materials.

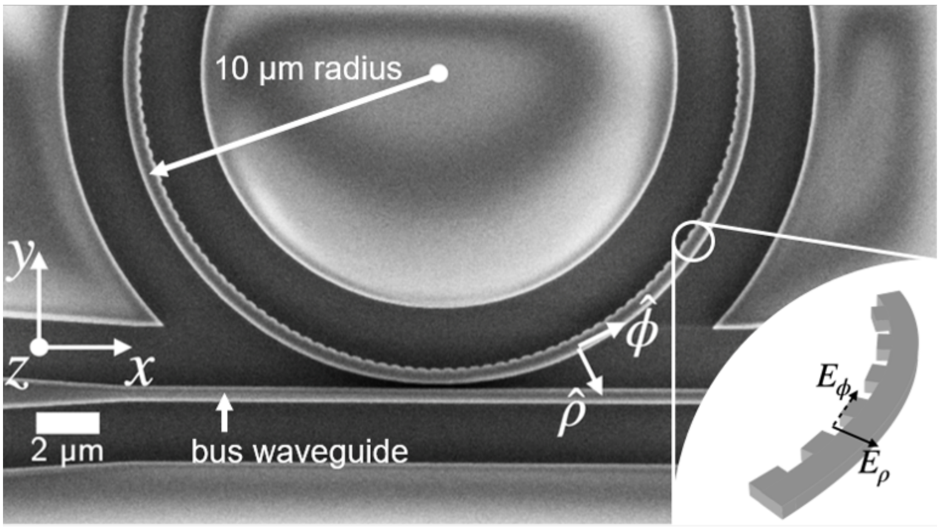

Figure 3.2: SEM image of the ring and the feeding waveguide (top view). The tapering of the bus waveguide can be seen in the bottom left part of the image. Inset: schematics of the square grating.

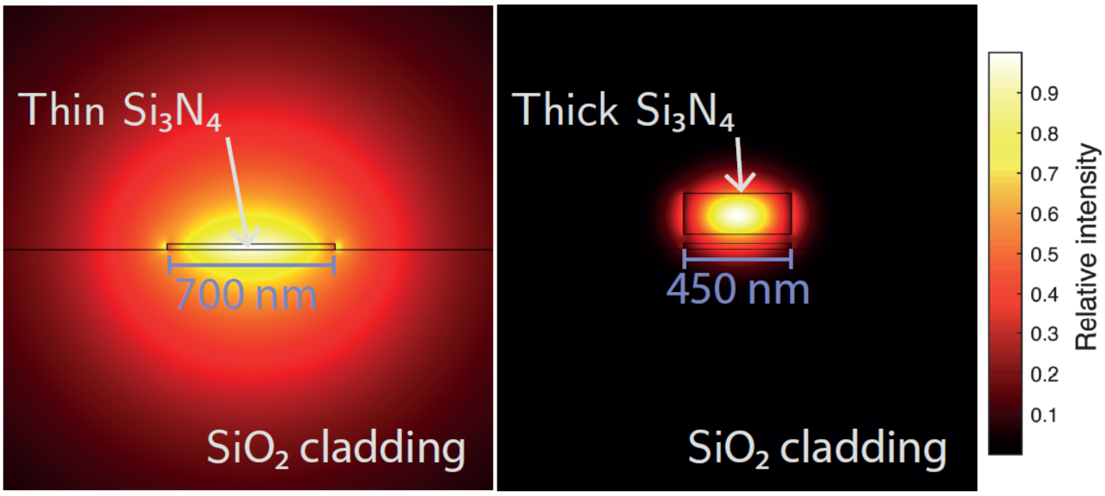

Figure 3.3: COMSOL Multiphysics simulations of the quasi-TE modes in the two different core geometries. Fig. duplicated from [30].

As we already explained, the device has two geometrical parameters called grating amplitude g and coupling gap width d. Indeed we had the possibility to test rings with different g and d.
We had 4 different values for $g = [30, 50, 70, 100]$ nm and at each value of g, 5 different values of $d = [100, 130, 160, 190, 220]$ nm. All these separated devices, together with their own bus waveguide, were fabricated on the same chip, with the parallel feeding waveguides travelling from one facet to the other of the chip; a photo in Fig. 3.4.

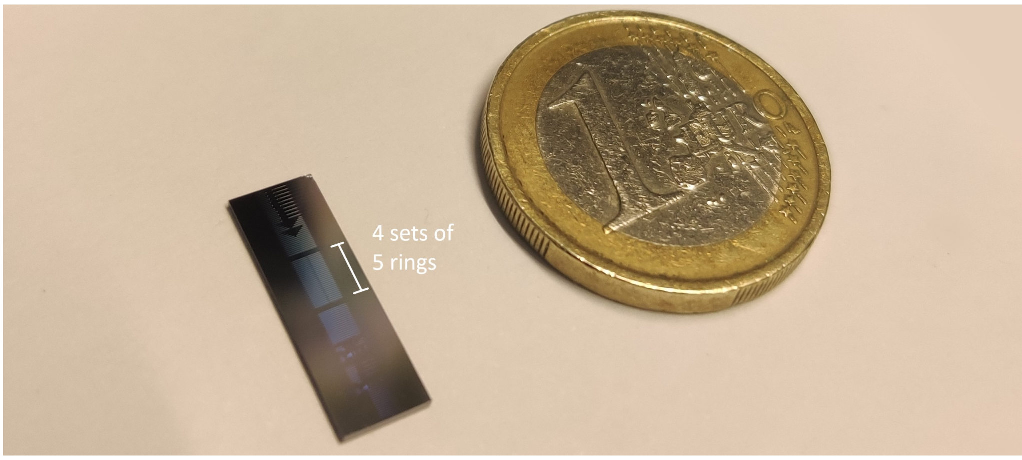

Figure 3.4: Picture of the chip with a 1 euro coin for comparison.

3.1.2 Materials

The device, fabricated by LioniX foundry, has been realized thanks to e-beam lithography with silicon nitride Si_3N_4 (for the waveguides) embedded into silicon dioxide SiO_2 (cladding) on a silicon Si substrate. Silicon nitride is a interesting material for optics, it allows for designs that range from low- to high-contrast waveguides with low propagation losses in the range of 0.3 dB/m to 1.0 dB/cm over the range from ~ 400 to ~ 2350 nm [31]. More on the fabrication process in [30]. The devices were made on the same wafer as the devices in [11], hence with the same layer stack up.

3.2 Experimental Setup

The experimental setup is composed by (in order from light source to emission imaging system):

- Ti:Sapphire laser (M Squared SolsTiS) connected to a wavemeter
- Free space optic system to couple the beam exiting from the Ti:S to a single mode fiber (SMF), attenuating the power - Polarized Beam Splitter (PBS), mirrors for alignment, Neutral Density (ND) filters,
- Fiber squeezer - to adjust polarization in order to optimize the coupling with the quasi-TE mode inside the bus waveguide,
- Fiber attenuator - a simple mechanism used to align and misalign two consecutive SMFs in order to reduce the power coupled into the chip,
- Fiber alignment motion system - used to align the SMF to the waveguide facet to in-couple the light. The chip was mounted on a temperature controlled aluminium chuck at the center of the fiber alignment system,
- out-coupling SMF - to collect from the feeding waveguide facet on the other side of the chip the light that is not coupled into the ring,
- interchangeable imaging systems.

During the data acquisition, in fact two different imaging systems have been employed:

1. a CCD camera sensor (Teledyne Lumenera INFINITY) together with a lens tube (InfiniTube 54-590), a quarter wave plate QWP (Altechna 2-CPW-ZO-L4-0729-S) linear polarizer LP plate (Thorlabs LPVIS100) and a near infra-red NIR 50x lens (Mytutoyo M Apo Plan NIR HR 50x). We will call this imaging system as "camera imaging system". A scheme is pictured in Fig. 3.5.
2. a free space powermeter head (Thorlabs S120VC) connected to a powermeter (Thorlabs PM400), together with a iris and LP plate. We will call this imaging system as "powermeter imaging system". A scheme is pictured in Fig. 3.6.

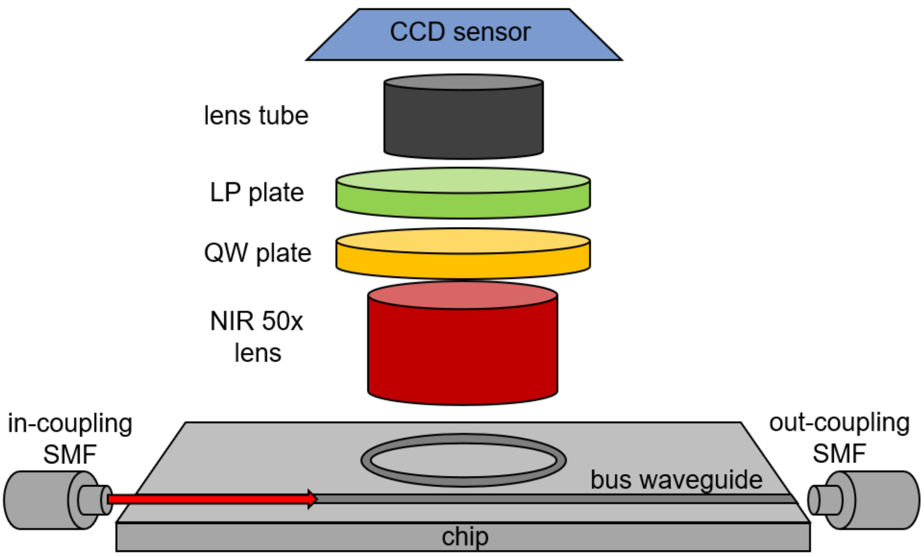

Figure 3.5: "Camera imaging system".

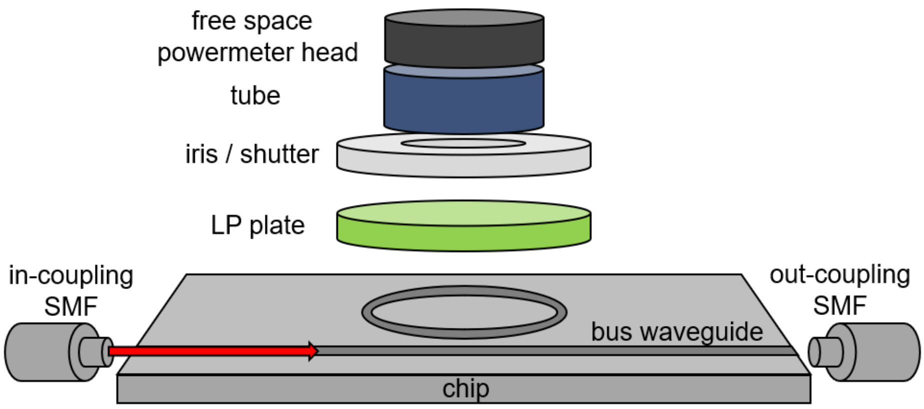

Figure 3.6: "Powermeter imaging system".

After manually aligning the in-coupling and (when needed) the out-coupling fiber and the imaging system, it has been possible to control most of the procedures by Python script, even remotely, in order to minimize all the possible vibrations that could interfere with the setup and disturb the data acquisitions. Indeed the Ti:S laser frequency, the rotation angle of the LP plate (thanks to a motorized rotation mount), the camera and the different powermeters (one for the Powermeter imaging system and a second to read the power of the out-coupled light in the second SMF) have been all interfaced and controlled by script.

Fig. 3.7 shows a photo of the camera imaging system.

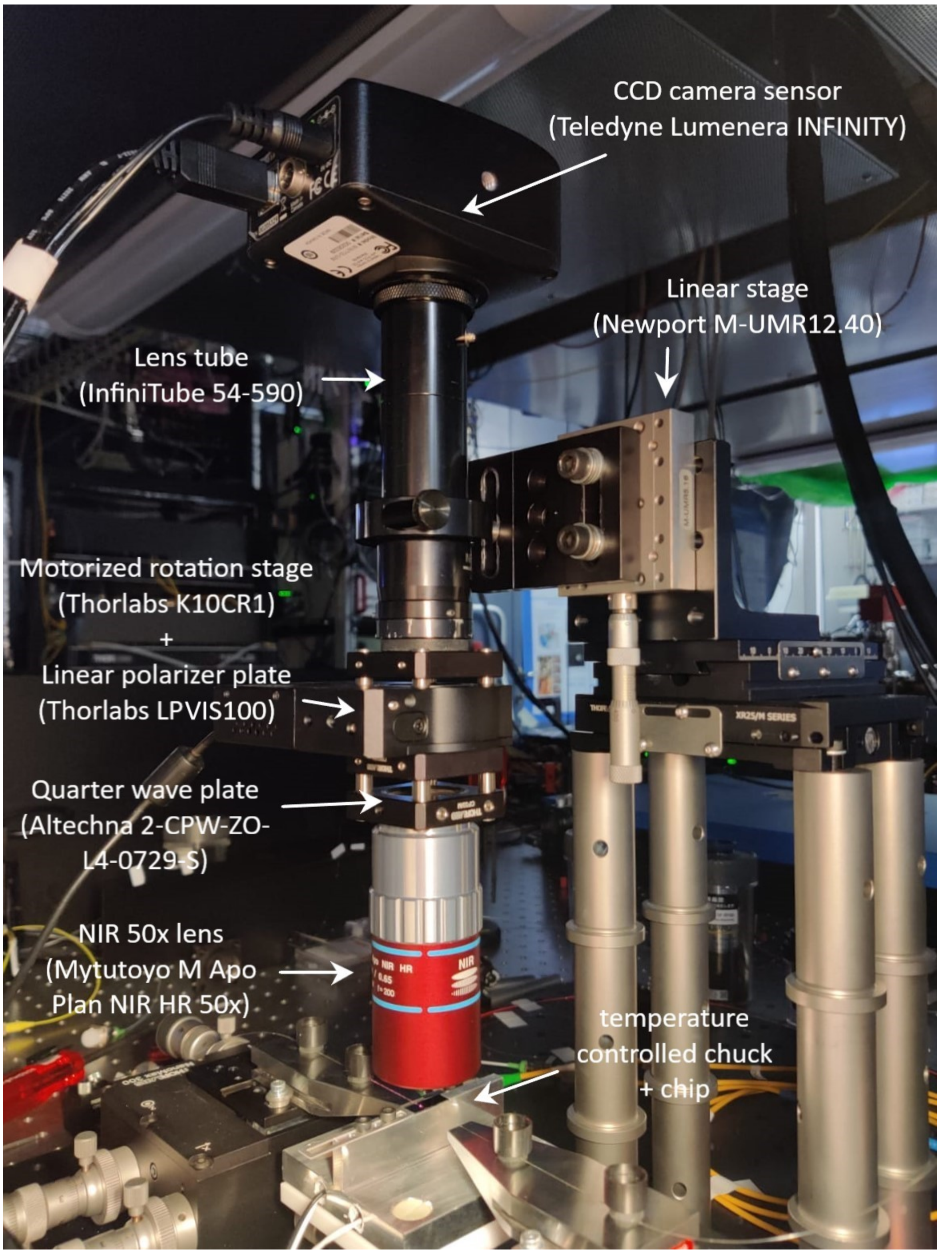

Figure 3.7: Photo of the camera imaging system over the ring resonator emitter (glowing in red).

3.3 Emission characterization

In this section is dedicated to the data acquisition and the following analysis in order to characterize the behaviour of the ring in dependence on the feeding light frequency, the grating amplitude g and the coupling gap width d. Eventually, the final purpose of the Chapter is to get a reliable value for the purity P_{σ_+}, defined as the ratio between the radiated intensity associated to the $\hat{\boldsymbol{\sigma}}_+$ circular polarization I_{rad,σ_+} and the total transverse radiated intensity $I_{rad,T}$. At the same time we aim at understanding what limits the polarization purity and how it's dependent on the structure parameters.

3.3.1 Critical coupling condition

As introduced in Section 2.1.3, there is a relation called *critical coupling condition* between the transmission coefficient t and the loss per round trip α. While t is directly linked with the coupling gap width d, α is the results of many contributions. We have a partial control over α thanks to the grating amplitude g. To test this condition, is possible to select a g and observe the out-coupled power in function of the in-coupled light frequency near a resonance and how this changes varying d.

Experimentally, this has been achieved with the following procedure. Let's choose one set of 5 rings with the same grating amplitude - $g = 30$ nm - and we couple one ring at the time starting from $d = 100$ µm and proceeding with all the following coupling gap widths. Coupling inside the feeding waveguide light at constant power ($\delta P_{in}/\bar{P}_{in} < 2\%$) with tunable wavelength, we can observe the response of the ring in frequency dependency measuring the out-coupled light in the second fiber. For each one of the rings we observe one resonance dip in the transmitted power at $\lambda \sim 722.7$ nm (that is mode $m = 144$, $l = 1$ from Eq. 2.1). The fact that these are not exactly at the same λ_0 might be given by multiple factors: the radius of the ring resonator and its core width can slightly vary due to fabrication processes, and therefore the effective refractive index associated to the mode. The power extinction for each one of the coupling gap widths are plotted in Fig. 3.8.

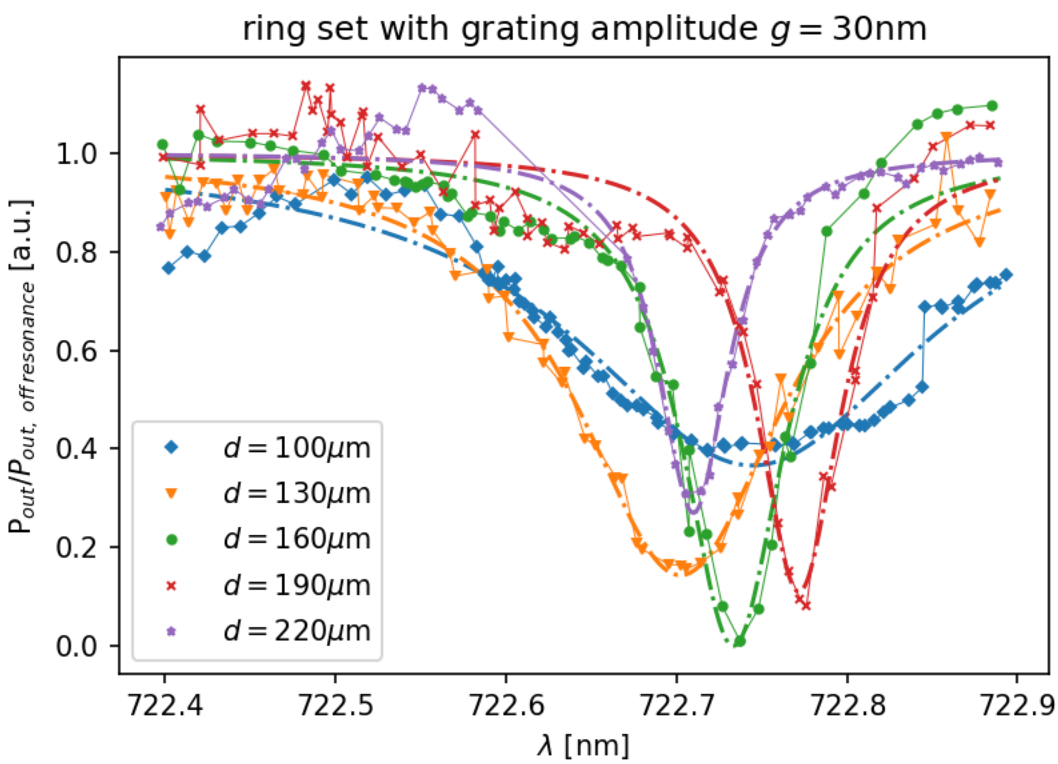

Figure 3.8: Wavelength dependency of the out-coupled power from the feeding waveguide for 5 different d values, keeping constant $g = 30$ nm. The markers represent the actual data, while the dot-dashed lines draw the Lorentzian best fits.

The data for each d have been fitted with a Lorentzian curve, as expected for a resonance in such a ring resonator.

$$\frac{P_{out}(\lambda)}{P_{out,\text{off resonance}}} = 1 - \frac{c}{\pi}\frac{\gamma}{(\lambda-\lambda_0)^2+\gamma^2} \tag{3.1}$$

In Fig. 3.9 are plotted the best fit parameters for all the d values. The extinction represents the contrast between the out-coupled power off resonance with the out-coupled power at resonance, then λ_0 is the resonance wavelength and γ is the HWHM.

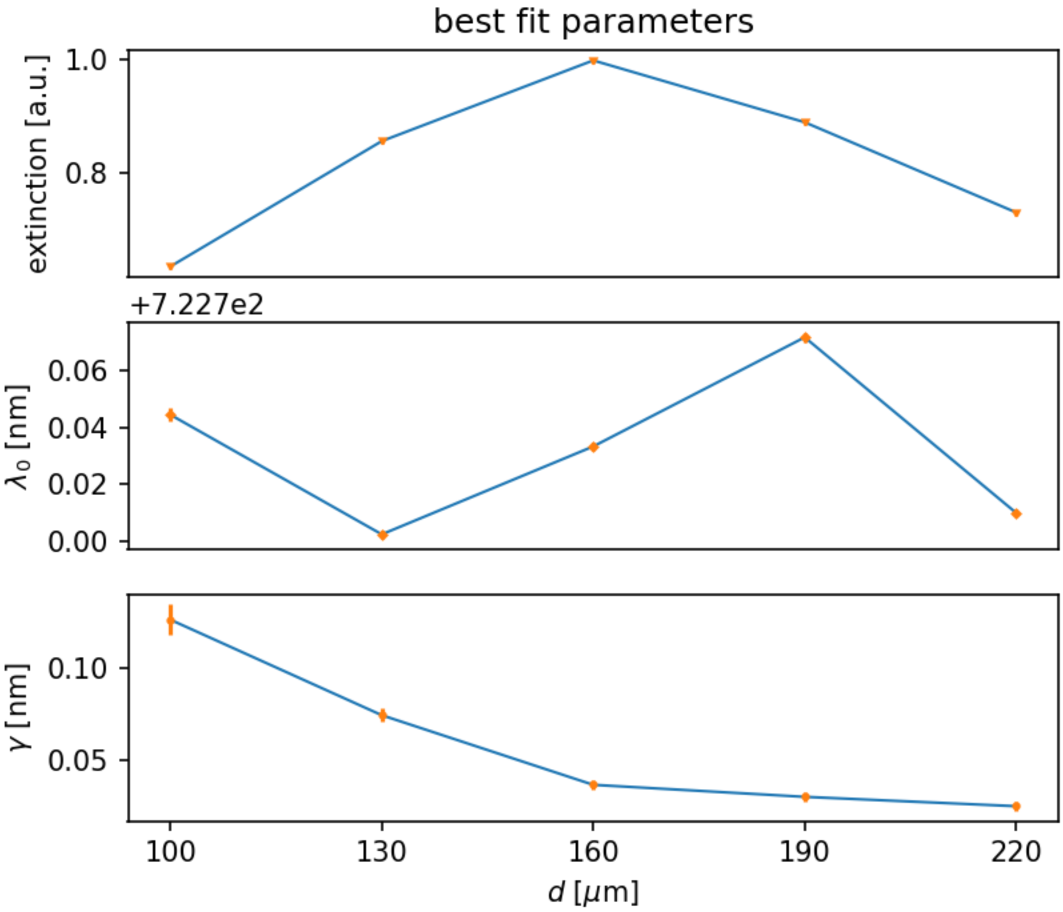

Figure 3.9: Best fit parameters for the different coupling gap widths d. From top to bottom: Extinction - the contrast between the out-coupled power off resonance with the out-coupled power at resonance; λ_0 - the resonance wavelength; γ - the HWHM.

As predicted in Section 2.1.3, for a fixed g value, univocally linked to one intensity decay rate value α, there is an optimal value for d that satisfy the *critical coupling condition* (Eq. 2.6), that maximizes the extinction (Fig. 3.9) and therefore maximizes the radiated power at resonance.

It's also interesting noticing how the coupling gap influences γ. As one can expect, increasing d, the quality factor $Q = \lambda_0/\gamma$ will also increase.

3.3.2 Emission imaging of modes $l = \pm 1, 0$

In this Section we present the procedure and the gathered data regarding the emission imaging of modes $l = \pm 1, 0$. In particular we will observe:

1. the radiated intensity pattern of the two $\hat{\boldsymbol{\sigma}}_{\pm}$ components in the plane $z = 100\mu\text{m}$,

2. the height scan of the beam, so how the total radiated intensity looks like across a section in the $x = 0$ plane ($\rho = 0, \phi = \pi/2$ plane).

In order to separately observe the two polarization components of the radiated light we used a quarter wave plate together with a linear polarizer. It's possible to select which polarization component to look at by adjusting the angle between the LP axis and the QWP fast axis. Fixing the angular position of the QWP, we can indeed rotate the LP using the motorized rotation stage where it's mounted. With a $\theta = +45°$ between the LP axis and the fixed QWP fast axis, it's possible to select just the $\hat{\boldsymbol{\sigma}}_{+}$ polarization component (RHCP); vice versa with a $\theta = -45°$, just the $\hat{\boldsymbol{\sigma}}_{-}$ polarization component (LHCP) can pass through the plates. The scheme is in Fig. 3.10. The composition of a QWP and a LP gives indeed a right/left hand circular polarizer system, depending on the θ angle.

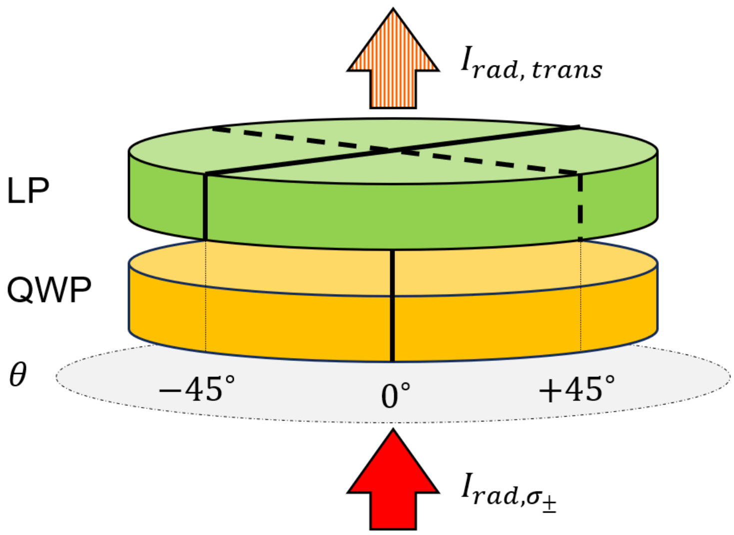

Figure 3.10: Plates system scheme - if $\theta = +45°$ ($\theta = -45°$) the complex is a RHC (LHC) polarizer.

In Fig. 3.11 are presented I_{rad,σ_+} and I_{rad,σ_-} for the modes $l = \pm1, 0$. The images are taken $100\mu\text{m}$ above the ring resonator plane, using the camera imaging system. The ring resonator used for these images has $g = 30$ nm and $d = 100$ nm.

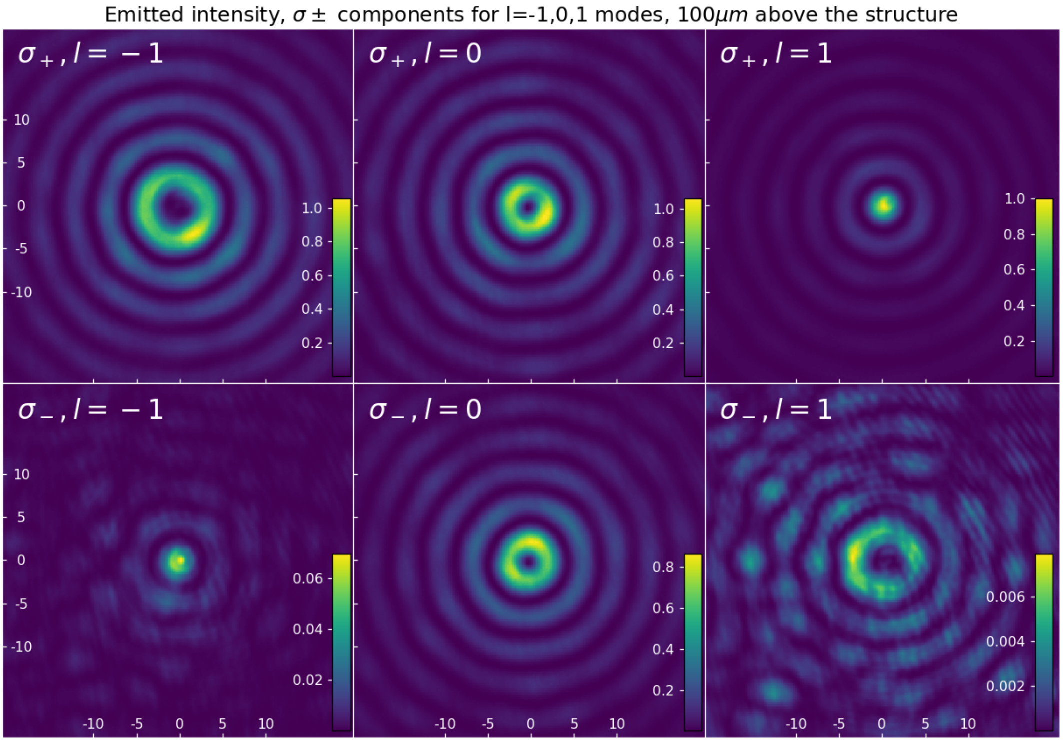

Figure 3.11: $I_{rad,\sigma_\pm}$ for the modes $l = \pm 1, 0$, images taken with the camera imaging system, 100µm above the ring resonator plane. The normalization is common for the polarization components in the same mode, but different for each mode.

For our purpose, the right column in Fig. 3.11, depicting mode $l = 1$, is the most interesting one. We can notice the resemblance to the simulation in Fig. 2.6 (*nb: the simulation shows the radiated electric field, while Fig. 3.11 shows the radiated intensity*). It's also observable a symmetry in the radiated patters patterns for opposite polarizations comparing the two modes $l = \pm 1$. However, even more interestingly, the purity on axis $\rho = 0$ of the two stronger components - $\hat{\boldsymbol{\sigma}}_+$ for $l = 1$ and $\hat{\boldsymbol{\sigma}}_-$ for $l = -1$ (so the ratio of the implied intensity component in respect of the total intensity) - is quite different. This is due to polarization asymmetry given by term ② in Eq. 2.30. Our choice to inject the light exciting a mode with a anticlockwise propagation direction instead of the other breaks the symmetry in the system, given $\Delta\varphi = -\pi/2$. The polarization purity for the most promising mode $l = 1$ will be measured in a more suitable and reliable way than just using these images, in Section 3.3.4.

In Fig. 3.12, 3.13 and 3.14 are pictured the total intensity z scans for the three modes $l = \pm 1, 0$. The image processing to arrive at such visualization goes as following: using the camera imaging system (without the LP and the QWP) we take 51 different images of the total intensity (visually similar to the ones in Fig. 3.11, but not selecting any polarization component) every 2 µm, starting from the focal plane (called z = 0 µm) of the ring and going up to z = 100 µm using a micrometric screw. Then it's possible to extract an angular average over ϕ of each image, obtaining 51 consecutive $I_{rad,tot}(\rho)$. Lastly, we merge together the 51 total intensity profiles in a $I_{rad,tot}(\rho, z)$ plot.

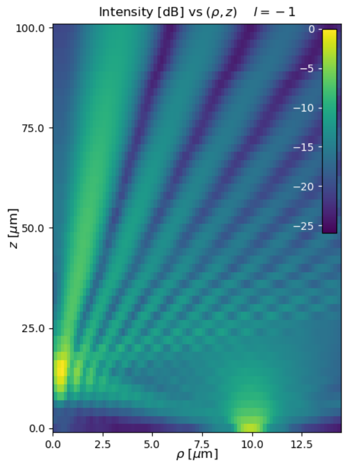

Figure 3.12: Radiated intensity, radial and height spatial distribution, mode $l = -1$.

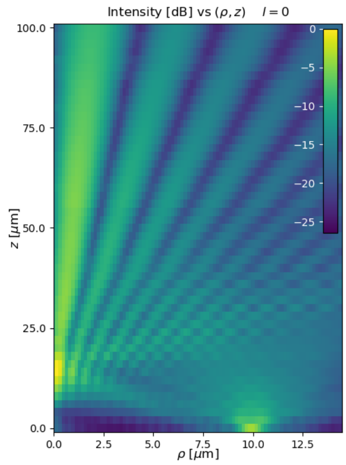

Figure 3.13: Radiated intensity, radial and height spatial distribution, mode $l = 0$.

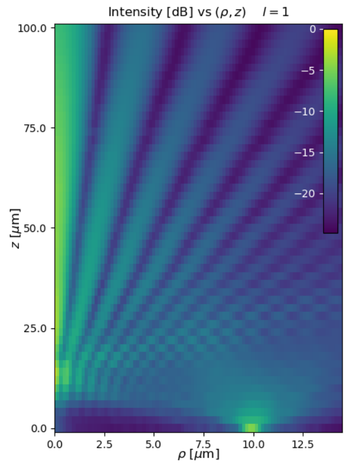

Figure 3.14: Radiated intensity, radial and height spatial distribution, mode $l = 1$.

3.3.3 Data-theory agreement

Now we can compare the data from the two intensity components I_{rad,σ_+} and I_{rad,σ_-} and the diffraction theory model for each one of the modes of interest. The images has been manipulated as in Section 3.3.2: selected a mode $\bar{l}$, it has been performed an angular average over ϕ on the two respective images of $I_{rad,\sigma_+,\bar{l}}$ and $I_{rad,\sigma_-,\bar{l}}$ in Fig. 3.11, obtaining two radiated intensity radial distributions $I_{rad,\sigma_\pm,\bar{l}}(\rho, z = 100\ \mu\text{m})$. To pass from pixel to µm a due calibration has been performed by using an image taken on the focal plane of the ring and knowing its nominal radius $R = 10$ µm. The conversion factor is $C = 0.1609$ µm/pixel for the used imaging system and lenses. Then is possible to normalize the angular average with the number of pixels in the whole circular area.

Simply taking the squared module of Eq. 2.27, we arrive at:

$$I_{rad,\sigma_\pm,l} \propto \left|E_{rad,\sigma_\pm,l}(\rho,\phi,z)\right|^2 = \left|K' J_{l\mp 1}\left(1 \pm \frac{E_\rho}{E_\phi}\right)\right|^2 \tag{3.2}$$

Where we substituted $\Delta\varphi = -\pi/2$ as specified in 2.2.2. For the fit of of both polarization components in the modes $l = \pm 1$ (4 curves) just one fitting parameter has been used (aside a scaling factor for K'): the $|E_\rho|/|E_\phi|$ ratio mentioned in Section 2.2.2. To fit the $l = 0$ mode is needed another fitting parameter, C_R. The fit functions for the two $\hat{\boldsymbol{\sigma}}_\pm$ intensity components in the $l = 0$ mode are given respectively by $\left|E_{rad,\sigma_\pm,l} + C_R E_{rad,\sigma_\mp,l}\right|$. This is given by the matching of the WGM index m and the number of grating elements q. In this condition the back-scattering at the grating elements is enhanced due to Bragg reflection and this produce a counter-propagating mode inside the ring waveguide [32]. The final emitted intensity for each one of the polarizations is the squared sum of the expected field component plus a portion (C_R) of the opposite emission pattern. All the other parameters, such as ν, z, R are fixed to be measured or nominal values. In Fig. 3.15, 3.16 and 3.17 are plotted the data for each mode relative polarization components, fitted with the model in Eq. 3.2.

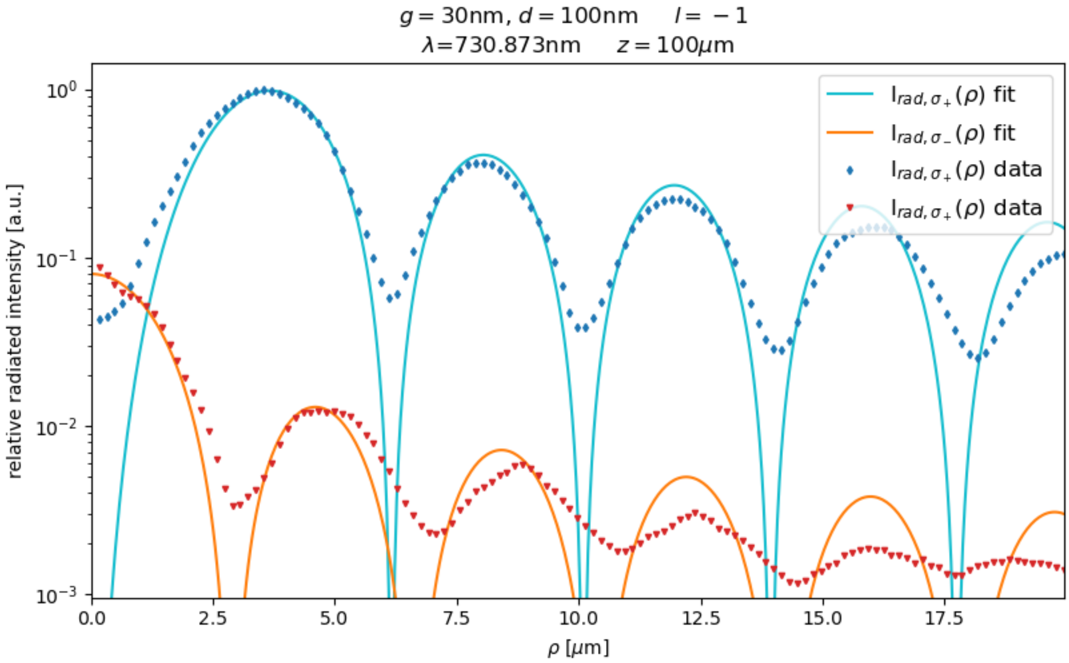

Figure 3.15: Data (markers) and fit (dashed lines) for the radial distribution of the relative radiated intensity, mode $l = -1$.

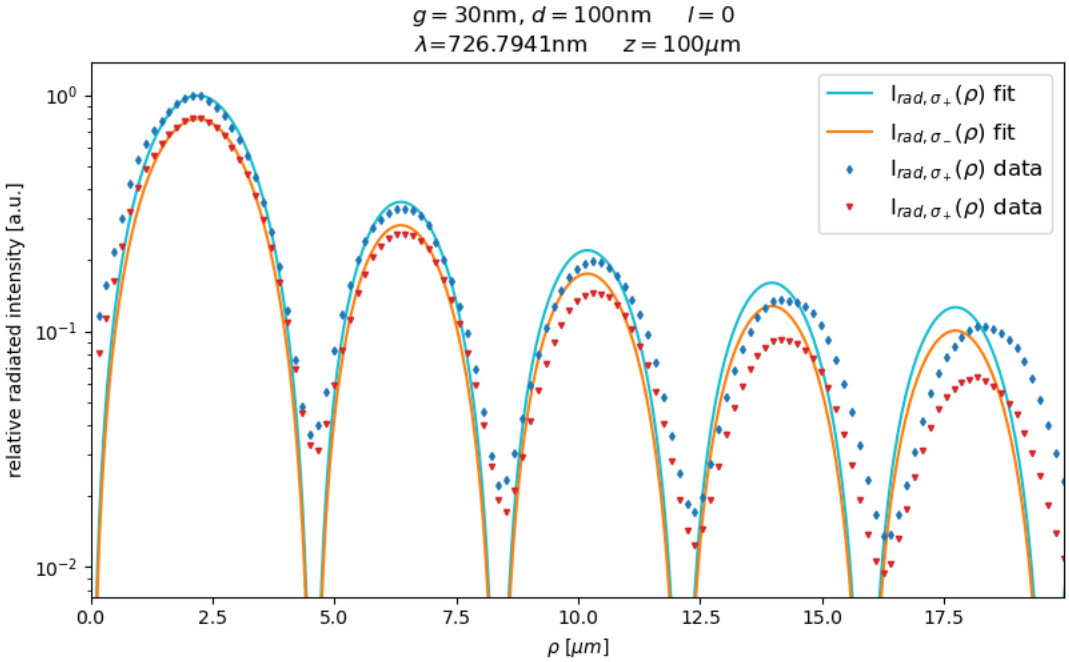

Figure 3.16: Data (markers) and fit (dashed lines) for the radial distribution of the relative radiated intensity, mode $l = 0$.

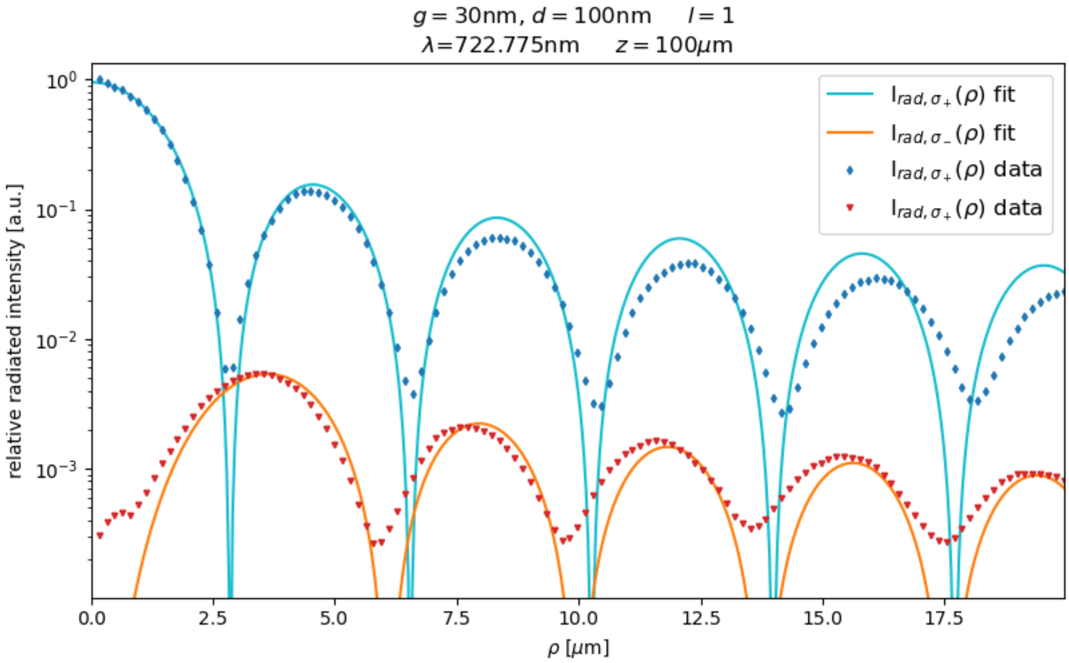

Figure 3.17: Data (markers) and fit (dashed lines) for the radial distribution of the relative radiated intensity, mode $l = 1$.

From all the three double curves fits, the fitting parameter $|E_\rho|/|E_\phi|$ is $\sim 1.34(9)$. It's also possible to notice that while the model is faithful to the data for $\rho < 12$ µm, it starts to be not quite reliable for bigger ρ, as we would expect since the diffraction theory model used here is in far field and paraxial approximations. However is pleasantly surprising to observe how the model describe fairly well for all the different modes, maintaining the same fit parameter value.

3.3.4 Polarization purity measurement

This Section is dedicated to evaluate the $\hat{\boldsymbol{\sigma}}_+$ component purity on axis ρ of the radiated intensity, with particular interest for the $l = 1$ mode. The purity is defined as

$$P_{\sigma_+} = \frac{I_{rad,\sigma_+,l=1}(\rho \sim 0)}{I_{rad,\sigma_+,l=1}(\rho \sim 0) + I_{rad,\sigma_-,l=1}(\rho \sim 0)} \tag{3.3}$$

With $\rho \sim 0$ is intended an average on a circular area with diameter $\sim 1/6$ of central spot diameter. This is achieved by closing the iris to an aperture $\varnothing \sim 0.5$ mm at $z \sim 5$ cm. Here we neglect the $I_{rad,z}$, being an $\mathcal{O}\left((\rho/z)^2\right)$ and therefore subdominant in the far field zone compared to the transverse components, as expressed in Section 2.2.1.

A straightforward method to measure the purity of a circularly-polarized beam consists in just exploiting a linear polarizer and observing the transmitted intensity. We can briefly explain why this method is effective using the Jones formalism: let's consider a light beam with polarization state $\boldsymbol{S}_{in} = \sqrt{P}\hat{\boldsymbol{\sigma}}_+ + e^{i\delta}\sqrt{1-P}\hat{\boldsymbol{\sigma}}_-$ (with $\hat{\boldsymbol{\sigma}}_+ = (1, -i)^t/\sqrt{2}$ and $\hat{\boldsymbol{\sigma}}_- = (1, i)^t/\sqrt{2}$) passing through a linear polarizer (LP) arbitrarily rotated by an angle θ in respect of the $\hat{\boldsymbol{x}} = (1, 0)$ direction. The P parameter acts as purity of the $\hat{\boldsymbol{\sigma}}_+$ (RHCP) component and δ is an arbitrary phase.

We call $M_{LP}(\theta)$ the 2×2 matrix for the LP at an angle θ.

$$M_{LP}(\theta) = R(-\theta)\, M_{LP,\hat{\boldsymbol{x}}}\, R(\theta) = \\ = \begin{bmatrix} \cos\theta & \sin\theta \\ -\sin\theta & \cos\theta \end{bmatrix} \begin{bmatrix} 1 & 0 \\ 0 & 0 \end{bmatrix} \begin{bmatrix} \cos\theta & -\sin\theta \\ \sin\theta & \cos\theta \end{bmatrix} = \begin{bmatrix} \cos^2\theta & \cos\theta\sin\theta \\ \cos\theta\sin\theta & \cos^2\theta \end{bmatrix} \tag{3.4}$$

The transmitted state will be

$$\boldsymbol{S}_{out} = M_{LP}(\theta)\, \boldsymbol{S}_{in} = \\ = \begin{bmatrix} \cos^2\theta & \cos\theta\sin\theta \\ \cos\theta\sin\theta & \cos^2\theta \end{bmatrix} \left\{ \frac{\sqrt{P}}{\sqrt{2}} \begin{pmatrix} 1 \\ -i \end{pmatrix} + e^{i\delta} \frac{\sqrt{1-P}}{\sqrt{2}} \begin{pmatrix} 1 \\ i \end{pmatrix} \right\} \tag{3.5}$$

And the transmitted intensity (adimensional) in function of θ, P and δ will be

$$I_{out}(\theta, P, \delta) = |\boldsymbol{S}_{out}|^2 = |M_{LP}(\theta)\, \boldsymbol{S}_{in}|^2 = \frac{1}{2}\left(1 + 2\sqrt{P(1-P)}\cos(\theta - 2\delta)\right) \tag{3.6}$$

We can notice that if $P = 1$ then $\boldsymbol{S}_{in} = \hat{\boldsymbol{\sigma}}_+$ is a pure circular polarization state and, as expected, the transmitted intensity is independent on the LP angle θ (in an analogue way it happens if $P = 0$, for the other circular polarization). Otherwise, if $P \neq 0$ from the transmitted intensity oscillation we can evaluate P and therefore the sought polarization purity. In Fig. 3.18 is shown the relation between the oscillation contrast of the measured transmitted intensity and the purity P. The contrast is defined as

$$C(P) = \frac{I_{out,max} - I_{out,min}}{I_{out,max}} = \frac{2\sqrt{P(1-P)}}{\frac{1}{2} + \sqrt{P(1-P)}} \tag{3.7}$$

We can notice that a low relative uncertainty on the oscillation contrast gives an even lower relative error on the purity value, due to the high derivative of $C(P)$, especially for $P \sim 1$. Measuring high levels of purity (close to 1) is easier and more reliable, exploiting this useful feature that grants a high sensitivity.

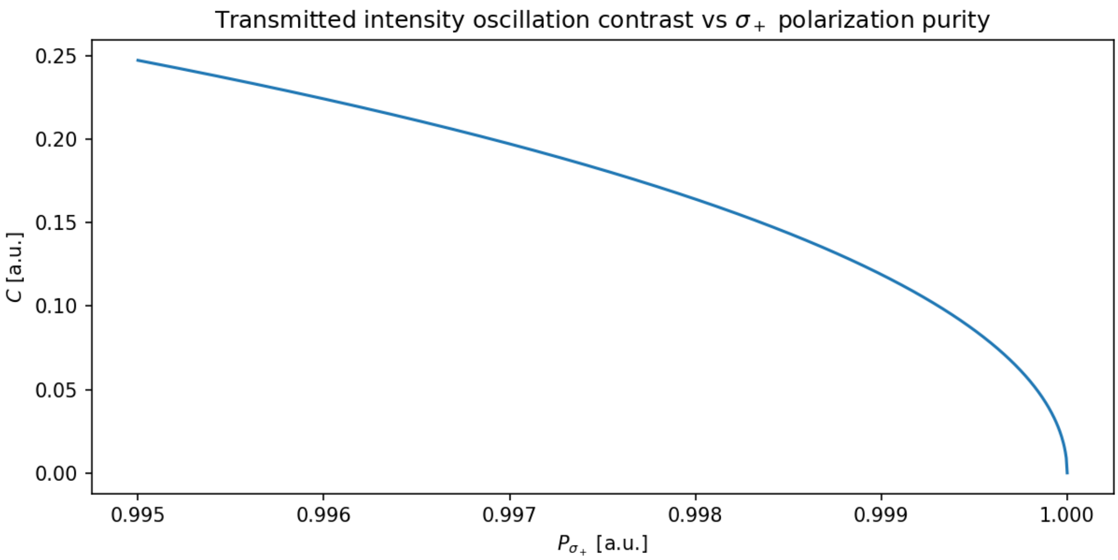

Figure 3.18: Oscillation contrast of the transmitted intensity in dependence of the polarization purity of the incoming field.

For the data acquisition, the powermeter imaging system, schematized in Fig. 3.6 has been employed. Aligning the center of ring resonator with the center of the iris and closing enough the shutter, is possible to measure the transmitted intensity through the LP in just the very center of the radiated pattern. As shown in Fig. 3.14, the radiated field diverges increasing the height. This means that it the iris is placed at $z \sim 5$ cm, the central spot is wide enough to be observed by eye. This permits a quite easy alignment of the imaging setup. Then, we measure the power read by the powermeter connected to the free space powermeter head that is screwed in a tube face down on top of the LP + iris stack. The tube is used to be sure that the power measured by the powermeter is just from the portion of light passing through the center of the almost completely closed iris ($\varnothing \sim 0.5$ mm).

In Fig. 3.19 is pictured the powermeter free space setup during the alignment procedure. The free space powermeter head is removed to observe the radiated beam projected on a white screen fixed above the structure. The iris is letting passing through the first three concentric fringes. For $l = 1$ is possible to see clearly the central spot.

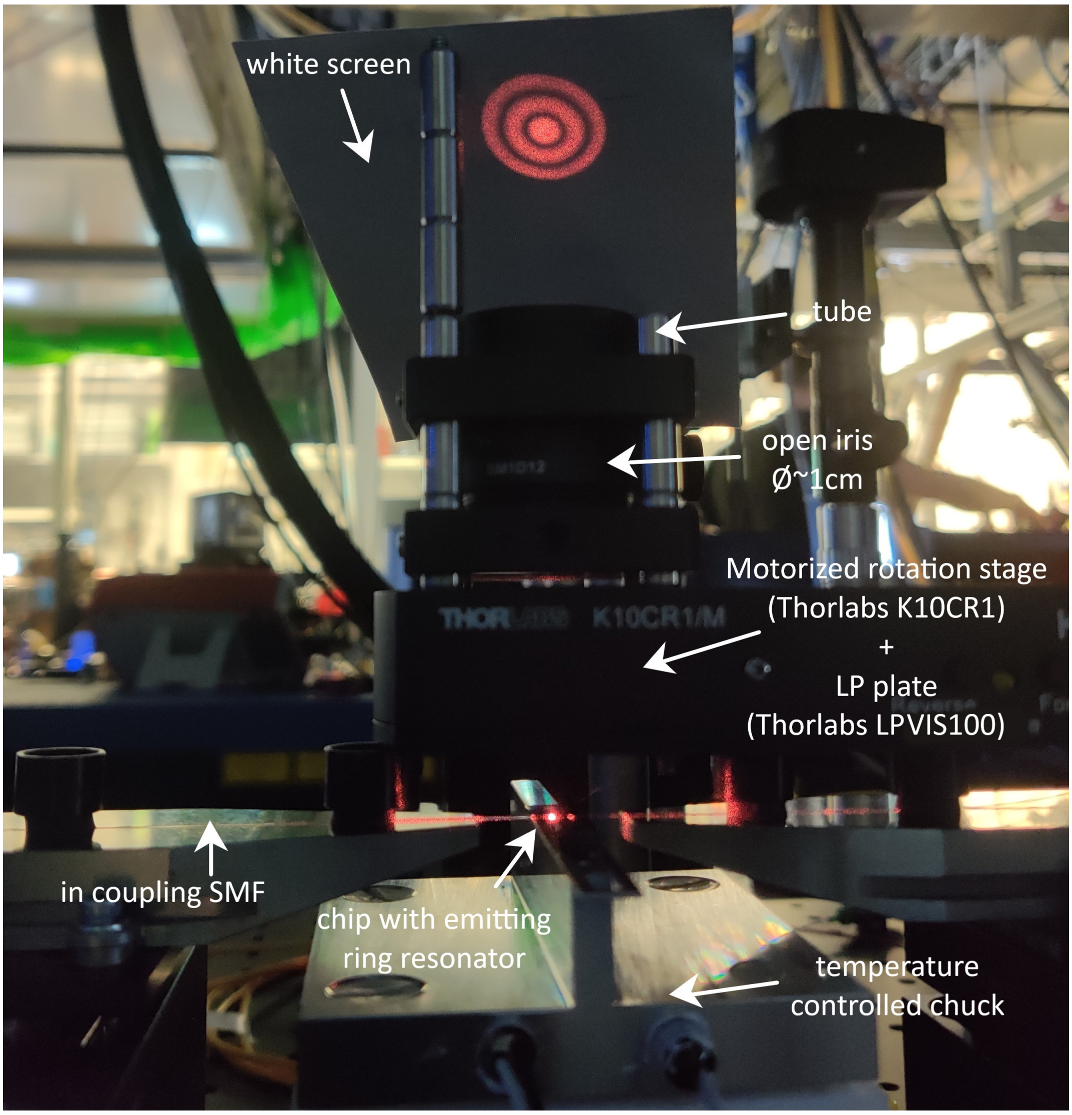

Figure 3.19: Picture of the powermeter imaging system. The free space powermeter head has been removed and a white screen has been added on top to visualize the projected beam.

Before passing to the complete polarization purity vs wavelength characterization, a single shot measurement - so fixing a frequency inside the $l = 1$ resonance and measuring the purity - on each one of the rings has been performed. This permits to better understand which device geometry, in terms of d and g, offers the highest purity values. Firstly a resonance scan like the ones shown in Fig. 3.8 for each ring has been taken; then, chosen a frequency inside the respective $l = 1$ resonance, a purity measurement, as described above, has been acquired. The results are plotted in Fig. 3.20. All the 20 rings have been tested with the same coupling conditions and the same imaging system alignment.

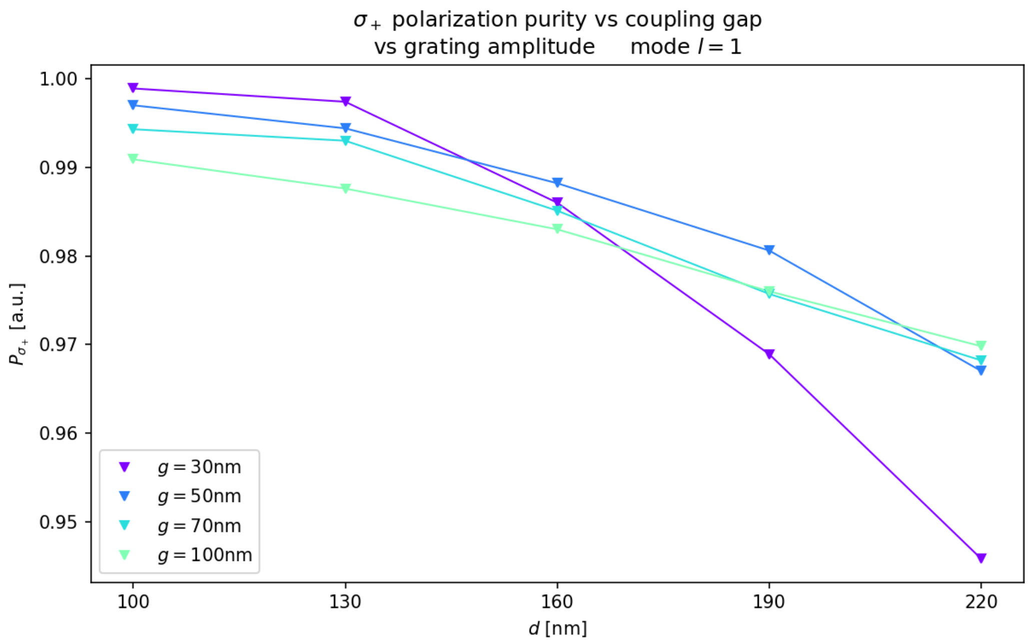

Figure 3.20: 20 single measurements of polarization purity on $l = 1$ resonance in function of grating amplitude and coupling gap.

Turns out that, for all the grating amplitude g values, the purity decreases by increasing the coupling gap width d and hence the quality factor Q, as defined in Section 3.3.1. We attribute this behavior to the fact that for a fixed intra-ring reflection coupling the forward and reverse propagating modes, the fraction contained in the reverse propagating mode increases with increasing Q [33]. Also, it seems that smaller gratings (fixed the best $d = 100$ nm) give higher purity. For this reason, overshadowing the *critical coupling condition* that would just give us a better radiated/in-coupled power ratio, we choose for the following characterization the ring with $d = 100$ nm and $g = 30$ nm.

Chosen the ring, the procedure for the polarization purity vs wavelength data acquisition is straightforward:

1. fix the wavelength to be inside the $l = 1$ resonance (previously scanned),
2. measure the transmitted intensity (through the LP and the sufficiently closed iris) with the powermeter,
3. rotate the LP plate by $\theta_{step} = 9°$ thanks to the motorized rotation mount,
4. repeat step 2 and 3 a total of 20 times, in order to have 20 intensity vs θ points between $[0°, 180°)$,

5. repeat step 1 - 4 for as many wavelengths as pleased, in order to study the polarization purity vs wavelength function.

From Eq. 3.6 is clear that the periodicity of $I_{out}(\theta, P, \delta)$ is 180°.

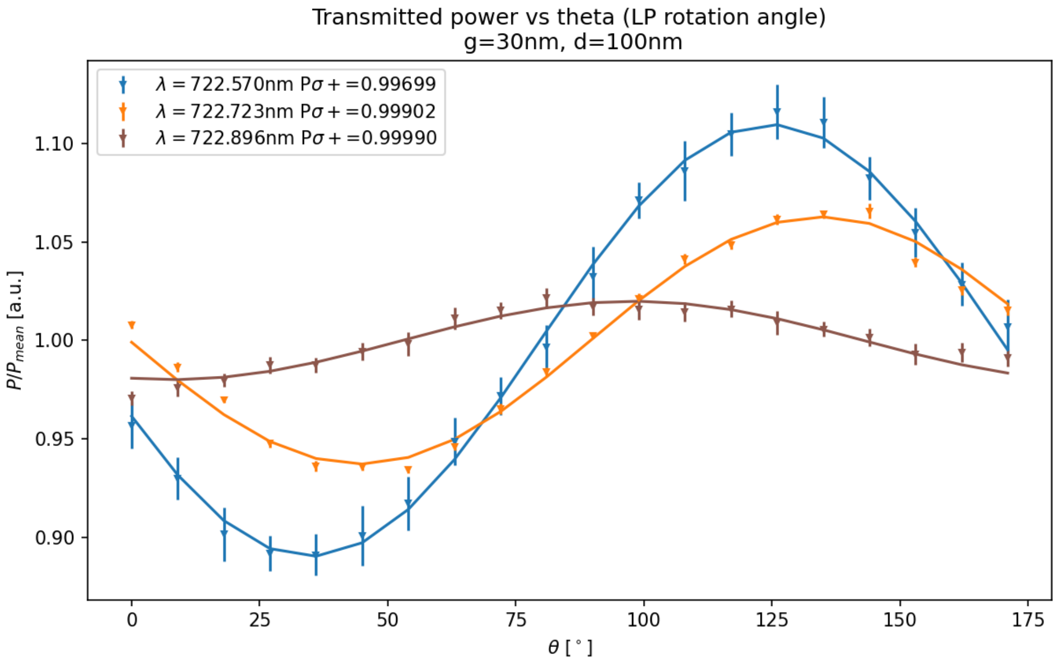

Figure 3.21: 20 data points (markers) and relative fits (solid lines) for three different wavelengths.

An example of transmitted power vs θ is presented in Fig. 3.21, for 3 wavelengths. As we can see, there is a θ dependency; this implies that the radiated field is a slightly impure circular polarization state. From the fit we can obtain the polarization purity values for the studied wavelengths. Iterating the process across the whole $l = 1$ resonance, Fig. 3.22 is obtained.

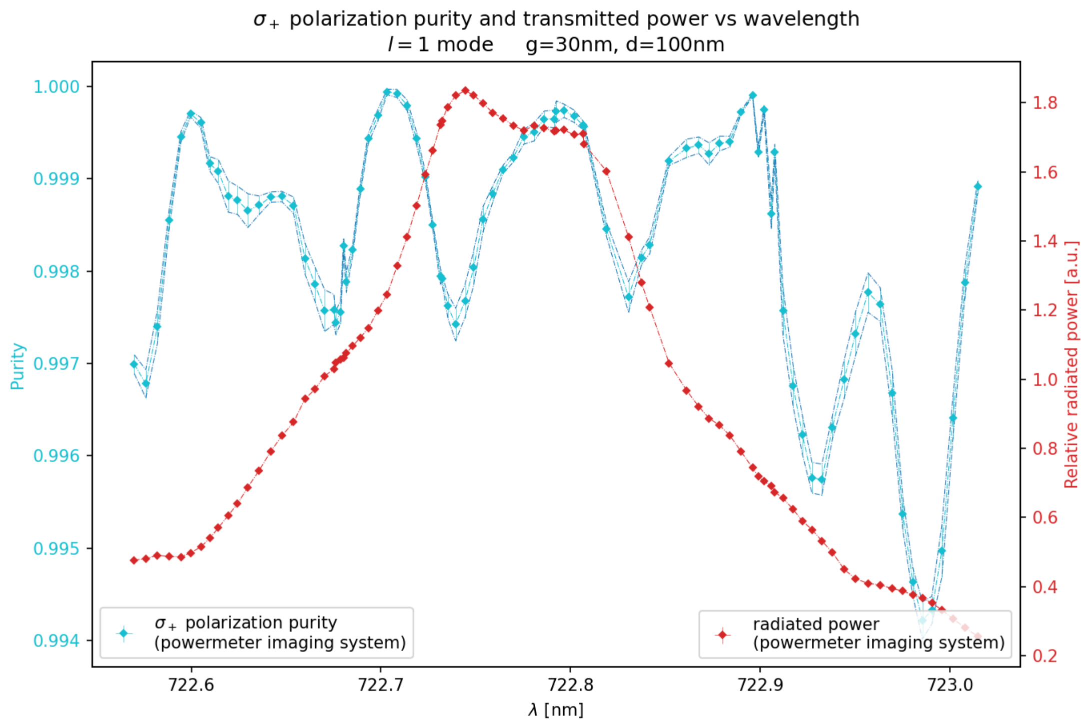

Figure 3.22: 20 data points (markers) and relative fits (solid lines) for three different wavelengths.

The average $\hat{\boldsymbol{\sigma}}_+$ polarization purity across the FWHM is 99.9%, and it reaches values above 99.99%.

We can also notice that there is clearly a non monochromatic oscillation in dependence of the wavelength. We observed this phenomenon being even more accentuated depending on how the fibers-chip alignment are arranged. We firstly noticed that coupling both the input and output optical fibers while measuring P_{σ_+} with the powermeter imaging system at various frequencies inside the $l = 1$ resonance, resulted in a strong purity-wavelength dependence. Then, placing the output fiber farther away from the exiting chip facet, this dependence decreased significantly. This decreased even more once a index matching gel has been applied both at the input fiber-chip facet touching point and at the exiting chip facet. The data in Fig. 3.22 are indeed acquired in this configuration.

A possible reason for this phenomenon can be addressed to a sum of *Fabry-Perot* cavity effects given by multiple unintentional built-in cavities that can cause a non trivial dependence on the used wavelength. For instance, the facets of the two input and output fibers, touching the chip, increase the reflectance of the two Si_3N_4-Air interfaces. This creates, for certain frequencies a constructive interference inside the bus waveguide resulting in a stranding wave. The standing wave can be seen as a sum of two waves, forward and back-propagating. Both of them are coupled (in different ratios) inside the ring, and promote the emission of a field with the same pattern, but with specular circular polarizations. This inevitably creates a modulation in the resulting polarization purity vs wavelength relation, that otherwise it's supposed to be (inside the resonance) constant. The modulation appears to not be monochromatic probably due to a superposition of multiple of these unwanted effects. At such high level of purity, even a subtle portion of reflected and therefore back-propagating mode can influence significantly the purity value, coupling into the ring in the unwanted direction. This however demonstrate the strength and sensitivity of our measuring method, able to measure oscillations in purity of $\sim 0.3\%$.

A possible next generation device based on the studied ring resonator, will be optimize to not present this effect, taking into account the structure of the chip, or even to exploit this phenomenon to its advantage.

Chapter 4

Hafnium Dioxide study

As introduced in Chapter 1, another crucial aspect to face when pursuing the integration of optics inside multilayered chips that will constitute next ion traps, is all about material study and optimization. Multiple wavelengths must indeed be transported along the chip to be eventually delivered to the ions using various sorts of outcouplers - in future possibly even with one based on the ring resonator studied in Chapters 2 and 3, or that exploits similar working principle. For this reason, there is an urgent need of suitable waveguide materials for all the frequencies of interest. A befitting material ought to have both quite higher refractive index than the cladding meant-to-be material and, also very important for scalability, low optical losses. Higher refractive index contrast $\Delta n = n_{core} - n_{clad}$ means:

- a higher confinement factor Γ of the guided modes - ratio between the power confined in the core and the total power [34],
- higher coupling factor between the guided mode and the emitted field if the waveguide is designed to have a diffraction gratings (as mentioned in Eq. 2.9). The coupling factor approximately scales with Δn^2 [34],
- smaller minimum device feature size (scaling roughly as λ/n) [35],
- a higher numerical aperture NA and a lower $\theta_c = \arcsin(n_{clad}/n_{core})$ permit the waveguide to accept more modes, obviously depending on the waveguide sizes too.

However it also means:

- stronger sidewall scattering for equivalent roughness [36].

Concerning losses instead: waveguide lengths might have to substantially increase in a hypothetical charge-coupled device (QCCD) [3] architecture. In state of the art trapped-ions quantum processors the employ integrated photonics, waveguides have a total length of ~ 5 mm [11]. Possibly in future, this path length will be extended to several centimeters, having the necessity to guide the wavelengths to different operation zones of the processor This means that having materials with sub 1 dB/cm losses is becoming more and more crucial, considering the $\sim 2-6$ dB usually lost for fibers-waveguides attachment and at the diffraction gratings.

4.0.1 Materials choice

From previous studies, we know that thermal ALD-deposited aluminum oxide is one of the best materials in terms of optical losses, both for scattering and absorption, in the blue and near UV

(NUV) range of wavelengths presenting a refractive index $n_{Al_2O_3} = 1.65 - 1.72$. A waveguide made with thermal ALD alumina can reach < 2 dB/cm losses at 405 nm and 3 dB/cm losses at 371 nm [12].

On the other hand, an interesting alternative seems to be hafnium dioxide. It is known to have a higher refractive index in the same frequency range $n_{HfO_2} \sim 2.1$ compared to alumina [37]. Optical and structural properties of thermal ALD-deposited hafnia seem to be strictly dependent on the thickness of the deposited layer. Indeed, increasing the thickness above ~50 nm results in a denser film, with higher refractive index but also with a more rough surface (passing from r_{RMS} =0.25 nm at $d \sim 10$ nm to r_{RMS} =2.03 nm at d~ 100 nm). This is due to a progressively more present crystallization of the compound [38]. Hafnium dioxide is also an already established material for UV optical coatings, it can be patterned with CMOS techniques and it's used as gate dielectric. We decide to use PEALD over thermal ALD for the depositions due to the advantage in speed. Going through an optimization process, we must perform and consecutively study multiple depositions and thermal ALD is a much slower technique. Which one of the two deposition processes offers better results in terms of reproducibility and optical properties of the resulting material is still unclear [39].

Here is our starting point. Making use of the PEALD over the thermal ALD, we will study hafnia and how its crystallization and surface roughness influence its optical properties. Then the pursued idea for material optimization is based on interrupting the hafnia crystallization process by interposing layers of alumina. In this way, we aim at creating a periodic hafnia-alumina multilayer structure, in order to maintain a relatively high refractive index (hafnia trait), a low surface roughness while exploiting a low-loss and well established matrerial for blue-UV waveguides, alumina.

Therefore in the following Sections, we will go through a study on an engineered *nano-laminate* composed by hafnium dioxide and aluminum oxide. Such multi-layer material is promising for realization of blue-UV waveguides, but maintains sufficiently high refractive index values and low losses in all the visible frequency range, comparably with the materials currently used for the same purpose. For instance at $\lambda \sim 400$ nm in a 100 nm thick slab, a $\Delta n_{Al_2O_3,SiO_2} \sim 0.21$ gives a TE_0 confinement factor $\Gamma = 0.339$. Having instead $\Delta n_{\text{multi-layer},SiO_2} \sim 0.47$ provides a TE_0 confinement factor $\Gamma = 0.696$ (and $\Gamma = 0.402$ for TM_0). The workflow for the studies of the HfO_2-Al_2O_3 films is divided in two consecutive parts, conducted in two different cleanrooms:

1. the fabrication process, consisting in material deposition using a Plasma-Enhanced Atomic Layer Deposition (PEALD) tool (by Oxford Instruments) in Binnig and Rohrer Nanotechnology Center at IBM Zürich,
2. the characterization process, which include refractive index and thickness study, together with optical losses for slab modes, has been realized with several tools in First-Lab at ETH Zürich.

We already introduced the reader to the specific technique/tools used for the fabrication and characterization of each one of studied thin films in Section 1.3. Here some details about the procedures will be described to give a better sense of a complete deposition-characterization workflow (respectively in the two distinct Sections) in order to achieve a optimized material in terms of sought performances.

4.1 Fabrication

As mentioned, just one tool has been employed for the fabrication process of all the studied films, the PEALD, indroduced in Section 1.3.1. This Section is instead meant to give to the reader a deeper understanding of which parameters influence the deposition process.

4.1.1 Deposition procedure

Each realized film has been deposited on two different substrates (during the same process session): a $< 100 >$ silicon (Si) 6 inches wafer with on top a 2.7 µm layer of thermal SiO_2, and on a 1.5 cm $\times$ 1.5 cm $< 100 >$ bare Si sample, cleaved from a bigger wafer. Depositing the same material on two distinct substrates allows for different kind of analysis, as explained in Section 4.2.

Choosing the PEALD as deposition technique, gives us the possibility to control different process settings parameters. The deposition temperature $T = 290°\text{C}$ has been kept constant for all the realized samples. The reason is fairly simple: if in future these promising materials will be integrated as waveguides or gratings inside a more complex chip together with other materials such as Pt (as shield between the integrated optics stack and the electrodes above), Au (for the trap electrodes), and so on, is required that the temperature of the depositions would monotonically decrease during the whole process, from substrate to the electrodes. This because low-temperature depositions can be affected by higher-temperature processes. Furthermore, $T = 290°\text{C}$ is a commonly used temperature for ALD and we have no interest in decreasing the temperature, since this could comport less dense material - so lower refractive index - and less pure films due to a lower efficiency of impurities annealing. Another two parameters that can be set in case of a multi-material periodic stacking (as explored in this study), are the periodicity P and the duty cycle DC of one material in respect of the other. Lastly, with a due calibration, is possible to decide the thickness d [nm] with a consistent reproducibility. These three structural parameters d, P and DC can be controlled by the number of cycles N_c of the PEALD process. Roughly 1 cycle, so the 4 complete steps in Section 1.3.1, corresponds to ~ 1 Å; this can vary depending on the precursor and the deposition temperature. The PEALD process can take several hours (i.e. 5. 5h for 700 cycles of Hafnia), so the goal thickness of all the depositions was meant to be just more than the minimum film height in order to guide at least one slab mode. This minimum thickness was established a priori simulating with COMSOL Multiphysics a slab mode for each material. For completeness in Section 4.2, both N_c and the measured d will be reported.

The material study starts with just the deposition and consecutive characterization of the two pure materials: alumina (aluminum oxide, Al_2O_3) and hafnia (hafnium dioxide, HfO_2). After this, 3 hafnia depositions of different thicknesses $\sim [10, 30, 70]$ nm have been realized in order to better understand the root mean square (RMS) surface roughness vs thickness relation. A slab material with higher RMS surface roughness is more affected by surface scattering loss, as explained in Section 1.2.3. The results, exposed in Section 4.2, led us in the direction of a multi-layered structure.

Then a series of multi-layer depositions with different P and DC has been performed, varying the number of cycles of the two precursors and number of loops in order to always arrive at a prefixed thickness of $d \sim 80$ nm. The depositions have been conducted fixing one of the two parameters P or DC and varying the other, in order to distinguish how changing the two would optimize the final product in terms of refractive index and optical losses. In this way, after a deposition the film was characterized to determine what and how to change for the next deposition and so on. The characterization and the consecutive analysis is presented in Section 4.2.

4.2 Characterization

We introduced in Sections 1.3.2 and 1.3.3 the two tools that helped us in the material characterization, spectroscopic ellipsometer and a prism coupler. Also an atomic force microscope (AFM) has been employed for surface analysis of the samples. Then we are going to present the results, along with the optimization process that led us to the final and best performing material.

4.2.1 Measurement expedients

As previously mentioned, the deposition of each film has been realized on two different substrates: on bare Si for the ellipsometry and on a 2.7 μm layer of silicon dioxide for the slab mode measurements with the prism coupler. The analysis with the spectroscopic ellipsometer works better with an iterative approach: firstly measuring the substrate optical properties on its own and then (with the substrate fixed parameters) proceeding with the characterization of the wafer substrate plus deposition. This increases the reliability and accuracy on the measurements of the deposited film on top. For the prism coupler measurements, so in particular the optical loss measurements, an oxide layer between the silicon substrate and the deposited film is strictly needed. Elsewhere all the coupled light from the prism would be absorbed by the silicon wafer without the possibility to observe a propagating mode in the alumina-hafnia slab.

As explained in the respective tool Sections, the refractive index and the thickness have been measured with the ellipsometer and the slab mode optical loss with the prism coupler.

4.2.2 Characterization of the optical properties

The most significant RMS surface roughness measurements regards the r_{RMS} vs d relation.
In Fig. 4.1, 4.2 and 4.3 are shown AFM scans over a 0.5 μm ×0.5 μm area of three different hafnium depositions respectively of $N_c = [100, 300, 700]$ and a measured $d = [11.78, 34.84, 77.10]$ nm, having RMS surface roughness $r_{RMS} = [0.161, 0.633, 2.636]$ nm.

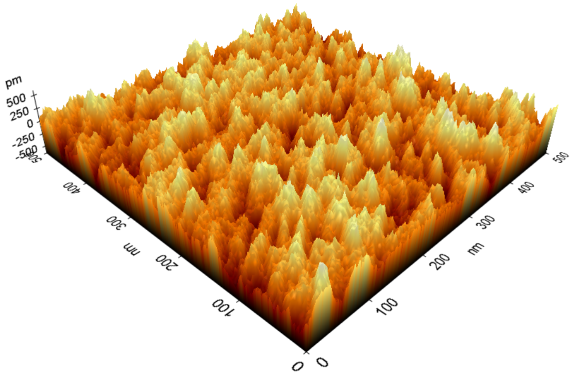

Figure 4.1: $N_c = 100$, $r_{RMS} = 0.161$ nm, $d = 11.78$ nm - AFM scan

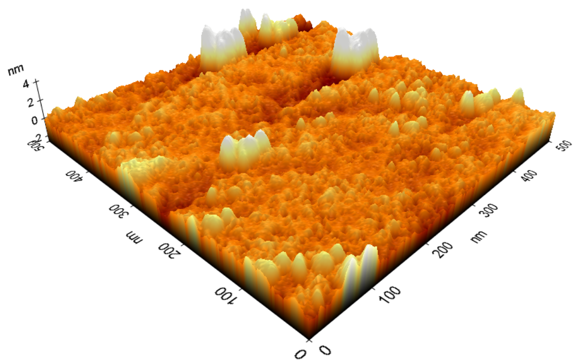

Figure 4.2: $N_c = 300$, $r_{RMS} = 0.633$ nm, $d = 34.84$ nm - AFM scan

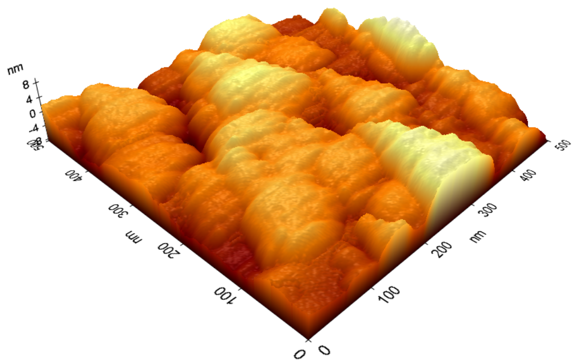

Figure 4.3: $N_c = 700$, $r_{RMS} = 2.636$ nm, $d = 77.10$ nm - AFM scan

In Fig. 4.4, a picture of the three 4 inches wafers with the depositions, plus, on the very right the bare Si wafer used as substrate.

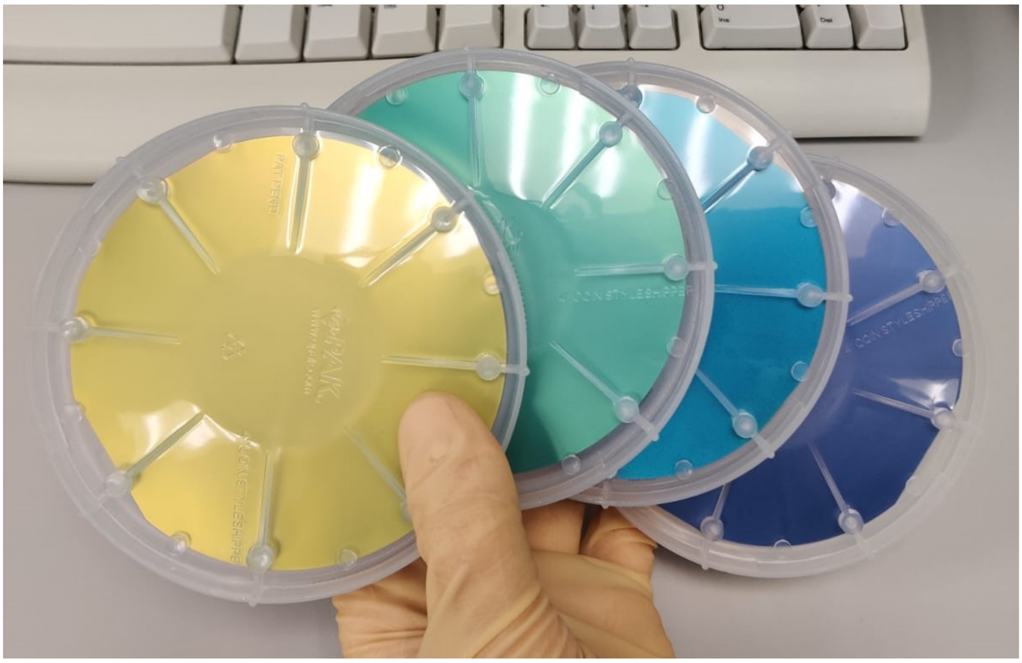

Figure 4.4: From left to right: 700, 300, 100, 0 cycles of PEALD hafnia on bare silicon wafers.

From these samples, interesting results can be highlighted: Firstly, the deposition rate (or growth per cycle) is stable and independent on the final thickness for a fixed temperature ($T = 290°$C), here $GPC = 1.15(4)$ Å/cy. Secondly, as expected from [38], the r_{RMS} increases more than linearly with d. This can be caused by a crystallization, that at high temperature, starts even at smaller thicknesses and increases rapidly. This phenomenon leads our study towards a multi-layering approach in order to stop the hafnia crystallization. We can vary DC and P, fixing the goal thickness to $\sim$ 80 nm, in order to maintain a relatively high refractive index and decreasing the optical losses. In Fig. 4.5 are shown the results from the spectroscopic ellipsometry measurements over a large array of depositions, from pure hafnia to pure alumina. DC is properly defined as $N$of Alumina cycles in 1 period/$N$of total cycles in 1 period (i.e. $DC = 0.33$ means 1 cycle of alumina and 2 of hafnia in one period of $P = 3$ cycles).

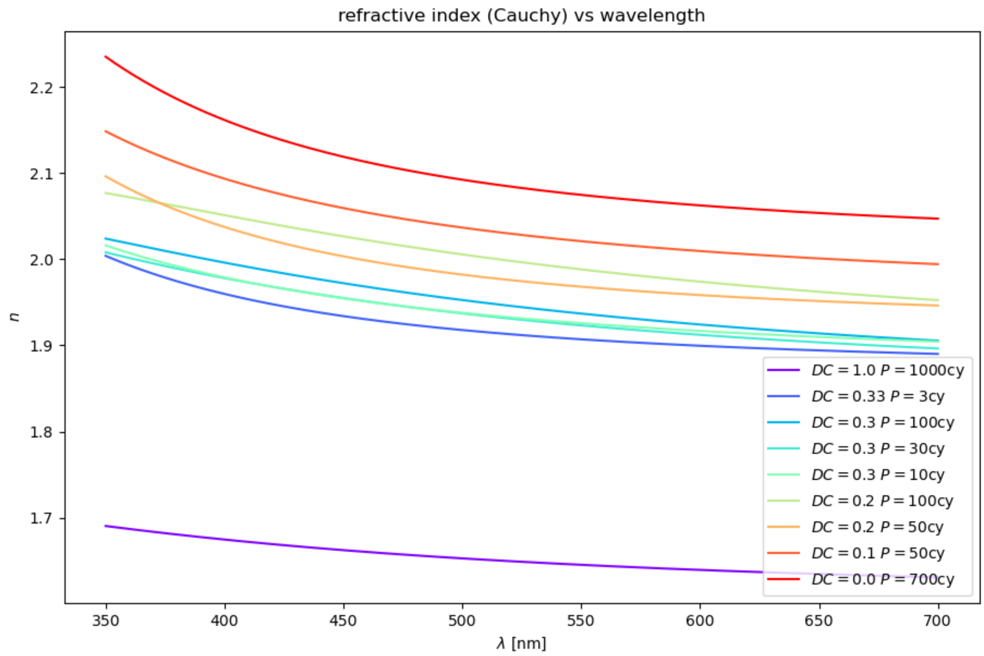

Figure 4.5: Cauchy fits to refractive index data from ellipsometry measurements of all the deposited samples.

As noticeable, decreasing the duty cycle, so increasing the percentage of hafnia in the film, gives a higher refractive index. Indeed, selecting one wavelength $\lambda = 406$ nm, and plotting $n(406\ \text{nm})$ vs DC, visualized in Fig. 4.6, the relation is linear. This indicates that the refractive index is strictly proportional to the ratio of the two oxides in the structure. The effective refractive index can be seen as a weighted average of the hafnia and alumina refractive indices.

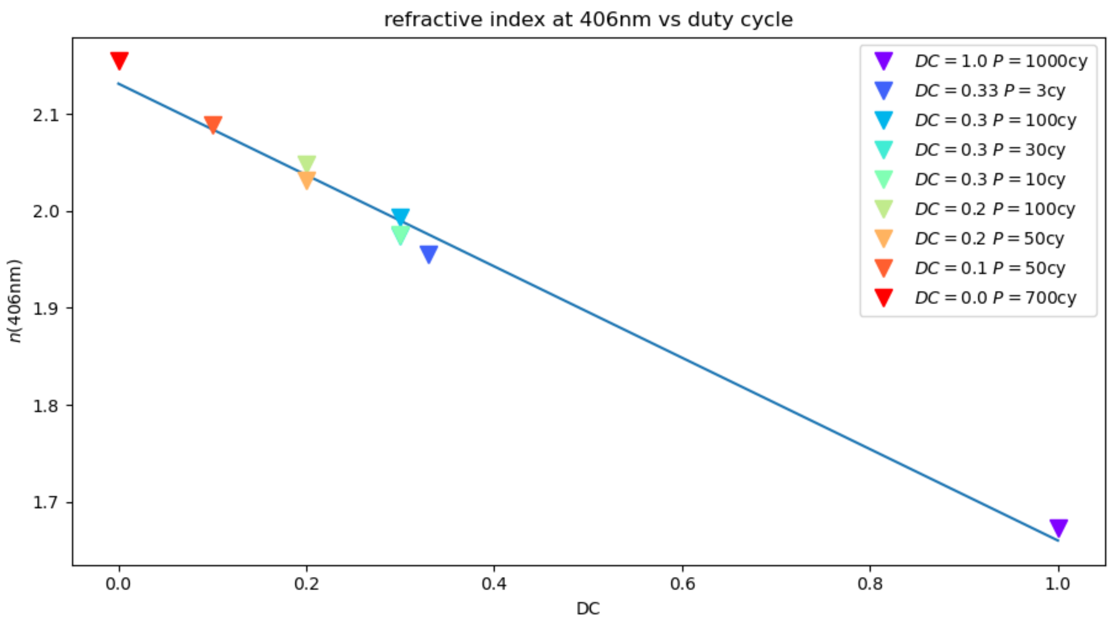

Figure 4.6: Refractive index at 406 nm in function of the duty cycle.

The optical loss for slab modes has been measured with the appropriate module of the prism coupler instrument at three different wavelengths $\lambda = [405.6, 526.5, 636.5]$ nm. The $I(x)$ function is directly fitted by the Metricon tool software and a loss value [dB/cm] can be found. However even if the slab mode is present for all the three tested wavelengths, it doesn't mean that is possible to measure a loss value. Indeed at the initial stage of the study, for some of the first deposited samples, like pure hafnia, it was not possible to measure the loss for the blue wavelength $\lambda = 405.6$ nm. At the very beginning of the optimization process, the losses of pure hafnia ($N_c = 1000$, $d \sim 120.0$ nm) were substantially high, with $l(636.5 \text{ nm}) = 13.78$ dB/cm and $l(526.5 \text{ nm}) = 33.26$ dB/cm and a not even measurable value at 405.6 nm. The optical loss at blue wavelength for the slab mode in an alumina film ($N_c = 1000$, $d = 119.2$ nm) was instead $l(405.6 \text{ nm}) = 1.71$ dB/cm. This value is higher than the one in [12] but, given our different fabrication technique, it ideally would be the goal value. However, as already explained, we aim at obtaining a material both with optical loss values comparable to alumina ones and with refractive index comparable with hafnia. It's reasonable to expect that, increasing the duty cycle of our multi-layer structure would decrease the losses as well as the refractive index. The results for the measured optical loss at 406nm are presented in Fig. 4.7 (the values for pure hafnia $DC = 0$ are not shown because impossible to measure with the used instrument).

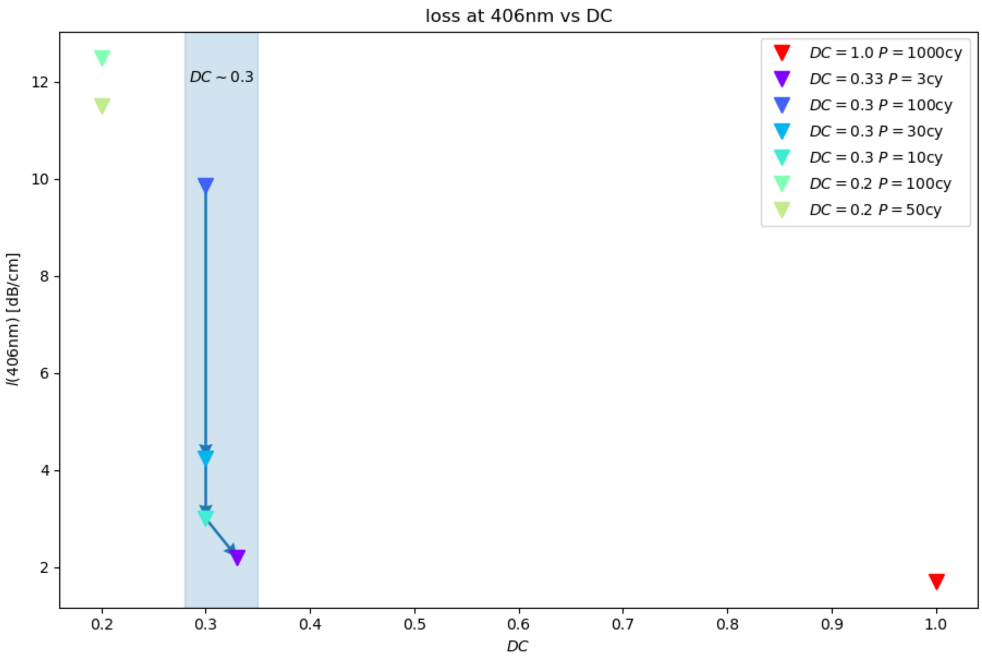

Figure 4.7: Optical loss for slab mode at 406nm in function of the duty cycle.

As expected, increasing DC brings down the losses, because we are depositing a compound that is more and more similar to the pure alumina (red marker).

Interestingly, we can notice another important feature that can be exploited for material optimization: fixing the duty cycle to i.e. $DC = 0.3$, as highlighted in Fig. 4.7 in the light blue region, the periodicity plays an important role. Following the arrow line in the $DC \sim 0.3$ region we are roughly not changing the ratio between the two materials but just the structure period. However it's clear that the optical loss is decreasing significantly with the periodicity. This phenomenon might be connected with the above mentioned crystallization of the hafnia. The consequence of the periodicity on the optical loss is compelling at all the tested wavelengths, as visible in Fig. 4.8. The data from four samples with $DC \sim 0.3$ and different periods have been fitted with a simple $l(\lambda) \propto 1/\lambda^4$ as expected for Rayleigh scattering losses. At $\lambda = [405.6, 526.5, 636.5]$ nm, changing the period P from 100 to 3 cycles, we obtain a change in the optical loss from $l = [9.85, 2.04, 1.11]$

dB/cm to $l = [2.2, 0.32, 0.18]$ dB/cm.

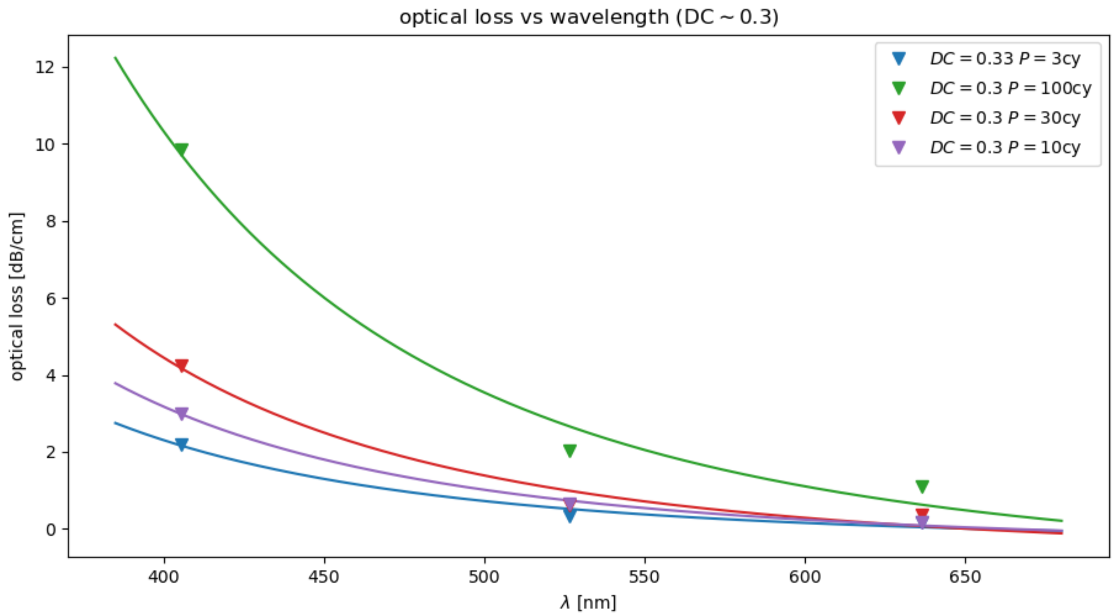

Figure 4.8: Optical loss for slab mode at different wavelengths for $DC \sim 0.3$. The data have been fitted with a simple $l(\lambda) \propto 1/\lambda^4$ as expected for Rayleigh scattering losses.

We consider the final best optimized material to be a multi-layer deposition of alumina-hafnia with period $P = 3$ cycles, duty cycle $DC = 0.33$. With this recipe, the compound maintains an effective refractive index $n(405.6 \text{ nm}) = 1.956$ and optical loss for a slab mode $l(405.6 \text{ nm}) = 2.2(1)$ dB/cm. The multi-layer approach manifests its efficacy: just by interposing layers of alumina (for one third of the total thickness) we sacrificed 9% of refractive index (from the $n_{HfO_2}(405.6 \text{ nm}) = 2.155$) to gain likely a 30 factor in loss (not even measurable for pure hafnia).

Using a simple 1 dimension computational model (analytically solvable) we can calculate the confinement factor of the slab mode in the optimized film, so the ratio between the power confined inside the core and the total propagating power, as in Eq. 1.20. For the calculation we use a SiO_2 substrate with $n_{SiO_2}(405.6 \text{ nm}) = 1.4825$, room temperature air as layer above with $n_{air} = 1.0003$ and a fixed core thickness of $d = 73.81$ nm. If $n_{core}(405.6 \text{ nm}) = 1.956$ the confinement factor for the TE_0 mode is $\Gamma = 0.527$, hence a material loss of (2.2 dB/cm)/0.527$\sim$ 4.2 dB/cm (and $\Gamma = 0.100$ for TM_0). For comparison, a core of alumina with the same thickness would not even support a TE_0 mode.

Fig. 4.9 shows a picture of the scattered light from the slab mode at $\lambda = 406$ nm coupled in the ($P = 3$ cycles ,$DC = 0.33$) wafer using the prism coupler.

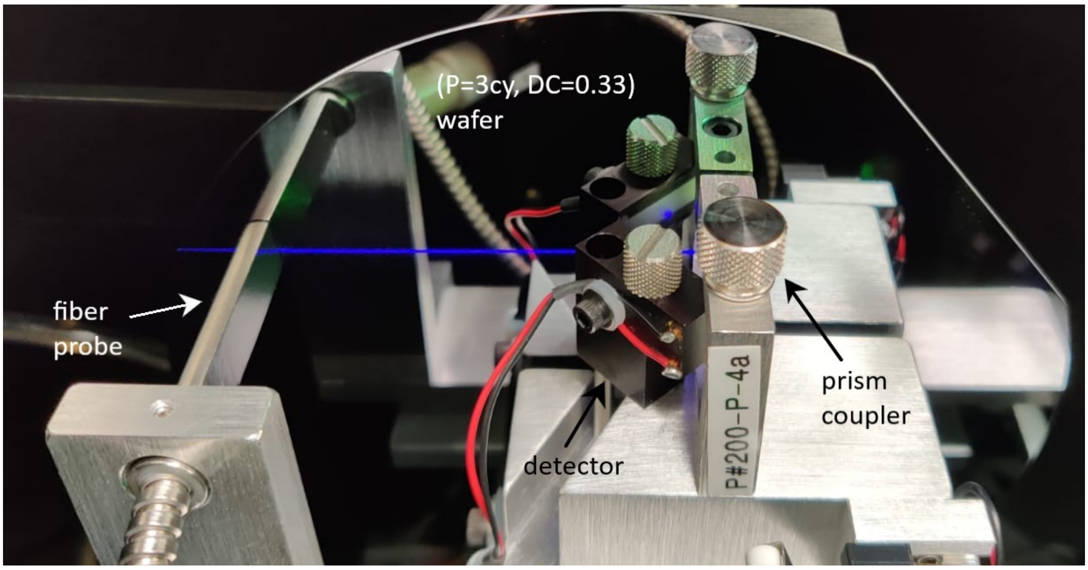

Figure 4.9: Photo of guided mode in the optimized sample during the prism coupler measurement.

To conclude, thanks to the study conducted in the present Chapter, we gave a promising alternative to the established alumina for blue-NUV waveguides. The alumina-hafnia multi-layer structure is characterized by high refractive index $n(405.6\text{ nm}) = 1.956$ and material losses $l_m(405.6\text{ nm}) \sim 4.2$ dB/cm in the blue range. With a further study on the best deposition process, the material can be further optimized to achieve even better optical properties, especially in terms of losses.

Chapter 5

Conclusions and Outlook

5.1 Conclusions

In this thesis we pursued the promising path of integrated photonics for Trapped-ion Quantum Systems.

The first goal was to provide a suitable outcoupler design able to radiate in free-space a highly pure circularly-polarized beam from a guided EM mode at the desired wavelength. In this regard, we presented a micro-metric ring resonator waveguide endowed of a square-profiled diffraction grating. In Chapter 2, using an analytical model based on diffraction theory, we were able to describe the far field radiated intensity from the resonator as a superposition of multiple dipoles emitting in phase. This simple model based on point dipoles allows valuable insight on the theory of the device as compared to full numerical simulations of the structure. The model shows how the resonator, taking advantage of the phase relation between the electric field components of the guided whispering gallery modes (WGMs) and also the structure of the LG modes, can radiate a Laguerre-Gaussian-alike beam that, depending on its azimuthal mode l reaches high circular polarization purity on axis. In particular, the device experimentally tested in Chapter 3, emits beams with average σ_+ polarization purity $\bar{P}_{\sigma_+} = 99.9\%$ across the $l = 1$ mode resonance ($\lambda_0 = 722.77$ nm, $\gamma_{HWHM} = 0.12$ nm), reaching values above 99.99% inside the FWHM interval. The measured intensity shows a spatial distribution of the two polarization component in agreement with the expected profile, calculated from the analytical model.

The second purpose of the thesis was to research on high refractive index low-optical loss materials suitable for high-contrast waveguides in the blue and NUV frequency range. After investigating how the deposition process of hafnium dioxide and aluminum oxide influences their optical properties, we pursued a multi-layer approach to reach the best material. The optimization process led us to a periodic *nano-laminate* constituted by consecutive layers of alumina and hafnia, respectively 33% and 67% of the 1-period thickness $P = 3.3$ Å. The compound presents an effective refractive index $n = 1.96$ and a material loss $l \sim 4.2$ dB/cm at $\lambda = 406$ nm. It represents an interesting alternative to the established pure alumina as it provides a much higher confinement factor (more than twice in a 0.1 μm thin slab with SiO_2 as cladding) and higher refractive index, allowing more compact gratings to emit at a given efficiency.

5.2 Outlook

Both projects constitute auspicious starting points towards a further optimization and a possible employment in future ion traps for quantum systems or in photonics devices in general.

The ring resonator presents multiple strengths: it can be easily integrated given its micrometric size; the design can be adapted, by changing the numbers of grating elements, the radius and the core material to work at the desired wavelength; the same ring can be used, changing the propagation direction of the fed light, to address both highly pure circular polarizations. Another peculiarity that distinguishes this design from the other options [24, 25], is the fact that the high polarization purity region is circumscribed and well localized in a central area, feature that can be useful for ion or atom addressing but that can be also limiting in other implementations. On top of these, the analytical model represents for us a fundamental optimization instrument: the design can be improved by changing the cross section size of the core - and hence the ratio of the electric field components of the guided WGMs - to improve the purity level. On the other hand, future devices should be designed having the observed *Fabry-Perot* effect in mind, to minimize any unwanted reflections that can be source of impurity, at this very level of polarization purity. Potentially this effect could also be positively exploit to enhance it. Another possible study could aim at tilting the emission angle of the beam, for instance changing the phase relation between the field scattered at each grating element. This could allow to place the ring resonator not directly below the ions location but instead on a side, such as the linear-polarization outcouplers [8]. Furthermore, being a resonator is a double-edged blade: the high purity level is indeed reached without any active tuning, however the inaccuracies of the fabrication process could lead to a resonance frequency shifted in respect of the desired one. A possible solution could be engineering the structure in order to have a low Q factor so a broader resonance (we showed the benefits in Section 3.3.4) and additionally implementing an active tuning mechanism, by exploiting the core material optical non-linearities to alter its refractive index and therefore the resonance wavelength. In this regard, using the thermo-optic effect is also possible but not ideal, being the device located in a cryostat and being a much slower and inefficient tuning method. Another promising path to consider is to exploit the 'purity vs phase of WGM field components' dependency - highlighted by the model - in a non-resonant device. A potential prototype could be constituted by an array of emitters arranged upon a line in order to radiate a much wider beam with high purity in the whole beam spot.

The study on alumina-hafnia multi-layer material also represents encouraging foundations for future researches. The measurements on loss on the PEALD alumina let us conclude that PEALD might be less adequate that thermal ALD, by a benchmarking with the results obtained in [12]. This might be due to a possible damage caused by the oxygen plasma directed on the sample during the reactant pulse [40]. The higher loss measured in PEALD and thermal ALD hafnia could also be a symptom of a crystallization that alumina seems to not present. Once established which deposition technique results in a better multi-layer structure, the material could be patterned and tested as fully-confined waveguide. From this study is indeed not trivial to distinguish whether the slab optical loss is majorly given by surface scattering loss or by material loss mechanisms, such as absorption or volume scatterings given by nano-crystals still present in spite of the multi-layering approach.

Chapter 6

Appendix 1

6.1 Diffraction theory model appendix

Thanks to the module of the distance between the the dipole s placed in the point $G_s(1, \phi_s, 0)$ and the arbitrary point $Q(\rho, \phi, z)$ that can be easily calculated as

$$r_s = \sqrt{z^2 + (1^2 + \rho^2 - 2\rho \cos \Delta\phi_s)},$$

is possible to define the versor $\hat{\boldsymbol{r}}_s$ directed from P to Q as $\hat{\boldsymbol{r}}_s = \mathbf{r}_s / r_s$.
Using the following relations, expressed in the Cartesian basis $B = \{\hat{\boldsymbol{x}}, \hat{\boldsymbol{y}}, \hat{\boldsymbol{z}}\}$:

$$\begin{aligned}
\hat{\boldsymbol{r}}_s &= \frac{1}{r_s} \{(\rho \cos \phi - \cos \phi_s)\hat{\boldsymbol{x}} + (\rho \sin \phi - \sin \phi_s)\hat{\boldsymbol{y}} + z\hat{\boldsymbol{z}}\} \\
\hat{\boldsymbol{\phi}}_s &= -\sin \phi_s \hat{\boldsymbol{x}} + \cos \phi_s \hat{\boldsymbol{y}} \\
\hat{\boldsymbol{r}}_s \wedge \hat{\boldsymbol{\phi}}_s &= \frac{1}{r_s} \left\{-z \cos \phi_s \hat{\boldsymbol{x}} - z \sin \phi_s \hat{\boldsymbol{y}} + (\rho \sin \phi_s \sin \phi + \rho \cos \phi_s \cos \phi - \cos^2 \phi_s - \sin^2 \phi_s)\hat{\boldsymbol{z}}\right\} \\
&= \frac{1}{r_s} \{-z \cos \phi_s \hat{\boldsymbol{x}} - z \sin \phi_s \hat{\boldsymbol{y}} + (\rho \cos \Delta\phi_s - 1)\hat{\boldsymbol{z}}\}
\end{aligned}$$

Now it's possible to express the first vectorial term of Eq. 2.14 as:

$$\begin{aligned}
|r_s|^2 (\hat{\boldsymbol{r}}_s \wedge \hat{\boldsymbol{\phi}}_s) \wedge \hat{\boldsymbol{r}}_s = \hat{\boldsymbol{x}} &\left\{-(z^2 + 1) \sin \phi_s + \rho \sin \phi - \rho \cos \Delta\phi_s \left[\rho \sin \phi - \sin \phi_s\right]\right\} + \\
+ \hat{\boldsymbol{y}} &\left\{+(z^2 + 1) \cos \phi_s - \rho \cos \phi + \rho \cos \Delta\phi_s \left[\rho \cos \phi - \cos \phi_s\right]\right\} + \\
+ \hat{\boldsymbol{z}} &\{\rho z \sin \Delta\phi_s\}
\end{aligned}$$

Then, projecting into the cylindrical basis $B' = \{\hat{\boldsymbol{\rho}}, \hat{\boldsymbol{\phi}}, \hat{\boldsymbol{z}}\}$, it's easy to find the terms whom E^{ϕ}_{ρ},E^{ϕ}_{ϕ} and E^{ϕ}_{z} are proportional to:

$$\begin{aligned}
\Big(|r_s|^2(\hat{\boldsymbol{r}}_s \wedge \hat{\boldsymbol{\phi}}_s) \wedge \hat{\boldsymbol{r}}_s\Big)_{\rho} &= -(z^2+1)\sin\phi_s\cos\phi - \rho\cos\Delta\phi_s\cos\phi\,[\rho\sin\phi - \sin\phi_s] + \\
&\quad + (z^2+1)\cos\phi_s\sin\phi + \rho\cos\Delta\phi_s\sin\phi\,[\rho\cos\phi - \cos\phi_s] \\
&= -\sin\Delta\phi_s\left(z^2+1-\rho\cos\Delta\phi_s\right) \\
\Big(|r_s|^2(\hat{\boldsymbol{r}}_s \wedge \hat{\boldsymbol{\phi}}_s) \wedge \hat{\boldsymbol{r}}_s\Big)_{\phi} &= (z^2+1)\sin\phi_s\sin\phi + \rho\cos\Delta\phi_s\sin\phi\,[\rho\sin\phi - \sin\phi_s] - \rho\sin^2\phi + \\
&\quad + (z^2+1)\cos\phi_s\cos\phi + \rho\cos\Delta\phi_s\cos\phi\,[\rho\cos\phi - \cos\phi_s] - \rho\cos^2\phi \\
&= \cos\Delta\phi_s\left(z^2+\rho^2+1-\rho\cos\Delta\phi_s\right) - \rho \\
\Big(|r_s|^2(\hat{\boldsymbol{r}}_s \wedge \hat{\boldsymbol{\phi}}_s) \wedge \hat{\boldsymbol{r}}_s\Big)_{z} &= \rho z\sin\Delta\phi_s
\end{aligned}$$

According to the far field approximation ($z/\rho \gg 1$) the terms can be simplified as:

$$\begin{aligned}
\Big((\hat{\boldsymbol{r}}_s \wedge \hat{\boldsymbol{\phi}}_s) \wedge \hat{\boldsymbol{r}}_s\Big)_{\rho} &\simeq -\sin\Delta\phi_s \\
\Big((\hat{\boldsymbol{r}}_s \wedge \hat{\boldsymbol{\phi}}_s) \wedge \hat{\boldsymbol{r}}_s\Big)_{\phi} &\simeq \cos\Delta\phi_s \\
\Big((\hat{\boldsymbol{r}}_s \wedge \hat{\boldsymbol{\phi}}_s) \wedge \hat{\boldsymbol{r}}_s\Big)_{z} &\simeq \frac{\rho}{z}\sin\Delta\phi_s
\end{aligned}$$

Similarly, it's possible to express in the B basis the third vectorial term of Eq. 2.14 as:

$$\begin{aligned}
|r_s|^2(\hat{\boldsymbol{r}}_s \wedge \hat{\boldsymbol{\rho}}_s) \wedge \hat{\boldsymbol{r}}_s = \hat{\boldsymbol{x}}&\left\{z^2\cos\phi_s - \rho\sin\Delta\phi_s(\rho\sin\phi - \sin\phi_s)\right\} + \\
+\,\hat{\boldsymbol{y}}&\left\{z^2\sin\phi_s - \rho\sin\Delta\phi_s(\rho\cos\phi - \cos\phi_s)\right\} + \\
+\,\hat{\boldsymbol{z}}&\left\{z - \cos\Delta\phi_s\right\}
\end{aligned}$$

Then, projecting into the cylindrical basis $B' = \{\hat{\boldsymbol{\rho}}, \hat{\boldsymbol{\phi}}, \hat{\boldsymbol{z}}\}$, it's easy to find the terms whom E^{ρ}_{ρ},E^{ρ}_{ϕ} and E^{ρ}_{z} are proportional to and then, using the far field approximation, we arrive to:

$$\begin{aligned}
((\hat{\boldsymbol{r}}_s \wedge \hat{\boldsymbol{\rho}}_s) \wedge \hat{\boldsymbol{r}}_s)_{\rho} &\simeq \cos\Delta\phi_s \\
((\hat{\boldsymbol{r}}_s \wedge \hat{\boldsymbol{\rho}}_s) \wedge \hat{\boldsymbol{r}}_s)_{\phi} &\simeq \sin\Delta\phi_s \\
((\hat{\boldsymbol{r}}_s \wedge \hat{\boldsymbol{\rho}}_s) \wedge \hat{\boldsymbol{r}}_s)_{z} &\simeq \frac{1}{z}(1-\rho\cos\Delta\phi_s)
\end{aligned}$$

N.B.: There's no need to calculate the second and fourth vectorial terms of Eq. 2.14 because they can be neglected, however it would be trivial.

Bibliography

[1] C. F. Roos et al. “Experimental Demonstration of Ground State Laser Cooling with Electromagnetically Induced Transparency”. In: *Phys. Rev. Lett.* 85.26 (Dec. 2000), pp. 5547–5550. ISSN: 1079-7114. DOI: 10.1103/PhysRevLett.85.5547.

[2] Colin D. Bruzewicz et al. “Trapped-ion quantum computing: Progress and challenges”. In: *Applied Physics Reviews* 6.2 (June 2019), p. 021314. ISSN: 1931-9401. DOI: 10.1063/1.5088164. URL: http://dx.doi.org/10.1063/1.5088164.

[3] D. Kielpinski, C. Monroe, and D. J. Wineland. “Architecture for a large-scale ion-trap quantum computer”. In: *Nature* 417 (June 2002), pp. 709–711. ISSN: 1476-4687. DOI: 10.1038/nature00784.

[4] Reinhold Blümel et al. “Efficient Stabilized Two-Qubit Gates on a Trapped-Ion Quantum Computer”. In: *Phys. Rev. Lett.* 126.22 (June 2021), p. 220503. ISSN: 1079-7114. DOI: 10.1103/PhysRevLett.126.220503.

[5] J. M. Pino et al. “Demonstration of the trapped-ion quantum CCD computer architecture”. In: *Nature* 592 (Apr. 2021), pp. 209–213. ISSN: 1476-4687. DOI: 10.1038/s41586-021-03318-4.

[6] I. Pogorelov et al. “Compact Ion-Trap Quantum Computing Demonstrator”. In: *PRX Quantum* 2.2 (June 2021), p. 020343. ISSN: 2691-3399. DOI: 10.1103/PRXQuantum.2.020343.

[7] Yunseong Nam et al. “Ground-state energy estimation of the water molecule on a trapped-ion quantum computer”. In: *npj Quantum Inf.* 6.33 (Apr. 2020), pp. 1–6. ISSN: 2056-6387. DOI: 10.1038/s41534-020-0259-3.

[8] Karan K. Mehta et al. “Integrated optical addressing of an ion qubit - Nature Nanotechnology”. In: *Nat. Nanotechnol.* 11 (Dec. 2016), pp. 1066–1070. ISSN: 1748-3395. DOI: 10.1038/nnano.2016.139.

[9] Karan K. Mehta and Rajeev J. Ram. “Precise and diffraction-limited waveguide-to-free-space focusing gratings - Scientific Reports”. In: *Sci. Rep.* 7.2019 (May 2017), pp. 1–8. ISSN: 2045-2322. DOI: 10.1038/s41598-017-02169-2.

[10] R. J. Niffenegger et al. “Integrated multi-wavelength control of an ion qubit”. In: *Nature* 586 (Oct. 2020), pp. 538–542. ISSN: 1476-4687. DOI: 10.1038/s41586-020-2811-x.

[11] Karan K. Mehta et al. “Integrated optical multi-ion quantum logic”. In: *Nature* 586.7830 (Oct. 2020), pp. 533–537. ISSN: 1476-4687. DOI: 10.1038/s41586-020-2823-6. URL: http://dx.doi.org/10.1038/s41586-020-2823-6.

[12] Gavin N. West et al. “Low-loss integrated photonics for the blue and ultraviolet regime”. In: *APL Photonics* 4.2 (2019), p. 026101. DOI: 10.1063/1.5052502. eprint: https://doi.org/10.1063/1.5052502. URL: https://doi.org/10.1063/1.5052502.

[13] Jiangbo Zhu et al. "Theoretical model for angular grating-based integrated optical vortex beam emitters". In: *Opt. Lett.* 38.8 (Apr. 2013), pp. 1343–1345. DOI: 10.1364/OL.38.001343. URL: http://ol.osa.org/abstract.cfm?URI=ol-38-8-1343.

[14] Christopher E. Langer. "High Fidelity Quantum Information Processing with Trapped Ions". In: *PhD Thesis* (Jen 2006). URL: https://www.nist.gov/system/files/documents/2017/05/09/langer_phdthesis.pdf.

[15] Hermann A. Haus. *Waves and Fields in Optoelectronics*. Upper Saddle River, NJ, USA: Prentice-Hall, 1984. ISBN: 978-0-13946053-1. URL: https://books.google.it/books/about/Waves_and_Fields_in_Optoelectronics.html?id=AQUpAQAAMAAJ&redir_esc=y.

[16] J. P. R. Lacey and F. P. Payne. "Radiation loss from planar waveguides with random wall imperfections". In: *IEE Proceedings J (Optoelectronics)* 137.4 (Aug. 1990), pp. 282–289. ISSN: 2053-9088. DOI: 10.1049/ip-j.1990.0047.

[17] F. P. Payne and J. P. R. Lacey. "A theoretical analysis of scattering loss from planar optical waveguides". In: *Opt. Quantum Electron.* 26.10 (Oct. 1994), pp. 977–986. ISSN: 1572-817X. DOI: 10.1007/BF00708339.

[18] David R. Boris et al. "The role of plasma in plasma-enhanced atomic layer deposition of crystalline films". In: *Journal of Vacuum Science & Technology A* 38.4 (2020), p. 040801. DOI: 10.1116/6.0000145.

[19] Becker and Sierka. "Atomistic Simulations of Plasma-Enhanced Atomic Layer Deposition". In: *Materials* 12.16 (Aug. 2019), p. 2605. ISSN: 1996-1944. DOI: 10.3390/ma12162605.

[20] Peter Ozaveshe Oviroh et al. "New Development of Atomic Layer Deposition: Processes, Methods, and Applications". In: *Sci. Technol. Adv. Mater.* (Apr. 2019). ISSN: 1468-6996. DOI: 10.1080/14686996.2019.1599694.

[21] Débora Gonçalves and A. Irene Eugene. "Fundamentals and applications of spectroscopic ellipsometry". In: *Quım. Nova* 25.6a (Nov. 2002). ISSN: 0100-4042. DOI: 10.1590/S0100-40422002000500015.

[22] Julien Cardin and Dominique Leduc. "Determination of refractive index, thickness, and the optical losses of thin films from prism-film coupling measurements". In: *Appl. Opt.* 47.7 (Mar. 2008), pp. 894–900. ISSN: 2155-3165. DOI: 10.1364/AO.47.000894.

[23] V. Negnevitsky et al. "Repeated multi-qubit readout and feedback with a mixed-species trapped-ion register". In: *Nature* 563 (Nov. 2018), pp. 527–531. ISSN: 1476-4687. DOI: 10.1038/s41586-018-0668-z.

[24] Christopher R. Doerr and Lawrence L. Buhl. "Circular grating coupler for creating focused azimuthally and radially polarized beams". In: *Opt. Lett.* 36.7 (Apr. 2011), pp. 1209–1211. ISSN: 1539-4794. DOI: 10.1364/OL.36.001209.

[25] Kévin G. Cognée et al. "Generation of Pure OAM Beams with a Single State of Polarization by Antenna-Decorated Microdisk Resonators". In: *ACS Photonics* 7.11 (Nov. 2020), pp. 3049–3060. DOI: 10.1021/acsphotonics.0c01081.

[26] Li He and Mo Li. "On-chip synthesis of circularly polarized emission of light with integrated photonic circuits". In: *Opt. Lett.* 39.9 (May 2014), pp. 2553–2556. ISSN: 1539-4794. DOI: 10.1364/OL.39.002553.

[27] Tom Schatteburg. "Simulation of high-purity circularly polarized light from a waveguide ring resonator with azimuthal grating". In: *Semester thesis in TIQI Group, ETHZ* (2018). URL: https://tiqi.ethz.ch/publications-and-awards/semester-theses.html.

[28] A. Yariv. "Universal relations for coupling of optical power between microresonators and dielectric waveguides". In: *Electronics Letters* 36 (4) (Feb. 2000), pp. 321–322. ISSN: 0013-5194. URL: `https://authors.library.caltech.edu/656`.

[29] Jeffrey B. Driscoll et al. "Large longitudinal electric fields (Ez) in silicon nanowire waveguides". In: *Opt. Express* 17.4 (Feb. 2009), pp. 2797–2804. DOI: `10.1364/OE.17.002797`. URL: `http://www.opticsexpress.org/abstract.cfm?URI=oe-17-4-2797`.

[30] Karan K. Mehta et al. "Towards fast and scalable trapped-ion quantum logic with integrated photonics". In: *Advances in Photonics of Quantum Computing, Memory, and Communication XII*. Vol. 10933. International Society for Optics and Photonics, Mar. 2019, 109330B. DOI: `10.1117/12.2507647`.

[31] Daniel J. Blumenthal et al. "Silicon Nitride in Silicon Photonics". In: *Proceedings of the IEEE* 106.12 (2018), pp. 2209–2231. DOI: `10.1109/JPROC.2018.2861576`.

[32] Xinlun Cai et al. "Integrated Compact Optical Vortex Beam Emitters". In: *Science* (Oct. 2012). URL: `https://www.science.org/doi/abs/10.1126/science.1226528`.

[33] Brent E. Little, Juha-Pekka Laine, and Sai T. Chu. "Surface-roughness-induced contradirectional coupling in ring and disk resonators". In: *Opt. Lett.* 22.1 (Jan. 1997), pp. 4–6. ISSN: 1539-4794. DOI: `10.1364/OL.22.000004`.

[34] Shun Lien Chuang. *Physics of Photonic Devices, 2nd Edition*. Hoboken, NJ, USA: Wiley, Jan. 2009. ISBN: 978-0-470-29319-5. URL: `https://www.wiley.com/en-us/Physics+of+Photonic+Devices%2C+2nd+Edition-p-9780470293195`.

[35] Clifford R. Pollock and Michal Lipson. *Integrated Photonics*. Boston, MA, USA: Springer, Boston, MA, 2003. DOI: `10.1007/978-1-4757-5522-0`.

[36] T. Barwicz and H. A. Haus. "Three-dimensional analysis of scattering losses due to sidewall roughness in microphotonic waveguides". In: *J. Lightwave Technol.* 23.9 (Sept. 2005), pp. 2719–2732. ISSN: 1558-2213. DOI: `10.1109/JLT.2005.850816`.

[37] K. Kukli et al. "Atomic Layer Deposition of Hafnium Dioxide Films from Hafnium Tetrakis (ethylmethylamide) and Water". In: *Chem. Vap. Deposition* 8.5 (Sept. 2002), pp. 199–204. ISSN: 0948-1907. DOI: `10.1002/1521-3862(20020903)8:5<199::AID-CVDE199>3.0.CO;2-U`.

[38] Yaowei Wei et al. "Growth properties and optical properties for HfO2 thin films deposited by atomic layer deposition". In: *J. Alloys Compd.* 735 (Feb. 2018), pp. 1422–1426. ISSN: 0925-8388. DOI: `10.1016/j.jallcom.2017.11.222`.

[39] Kyoung-Mun Kim et al. "Structural, Optical and Electrical Properties of HfO2 Thin Films Deposited at Low-Temperature Using Plasma-Enhanced Atomic Layer Deposition". In: *Materials* 13.9 (Apr. 2020), p. 2008. ISSN: 1996-1944. DOI: `10.3390/ma13092008`.

[40] David R. Boris et al. "The role of plasma in plasma-enhanced atomic layer deposition of crystalline films". In: *J. Vac. Sci. Technol., A* 38.4 (May 2020), p. 040801. ISSN: 0734-2101. DOI: `10.1116/6.0000145`.